NASA/TM—2004-211991/PART2

# Turbomachine Sealing and Secondary Flows

## Part 2—Review of Rotordynamics Issues in Inherently Unsteady Flow Systems With Small Clearances

R.C. Hendricks
Glenn Research Center, Cleveland, Ohio

L.T. Tam
Lockheed Martin Space Systems Company, Sunnyvale, California

A. Muszynska
A.M. Consulting, Minden, Nevada

July 2004

The NASA STI Program Office . . . in Profile

Since its founding, NASA has been dedicated to the advancement of aeronautics and space science. The NASA Scientific and Technical Information (STI) Program Office plays a key part in helping NASA maintain this important role.

The NASA STI Program Office is operated by Langley Research Center, the Lead Center for NASA's scientific and technical information. The NASA STI Program Office provides access to the NASA STI Database, the largest collection of aeronautical and space science STI in the world. The Program Office is also NASA's institutional mechanism for disseminating the results of its research and development activities. These results are published by NASA in the NASA STI Report Series, which includes the following report types:

- TECHNICAL PUBLICATION. Reports of completed research or a major significant phase of research that present the results of NASA programs and include extensive data or theoretical analysis. Includes compilations of significant scientific and technical data and information deemed to be of continuing reference value. NASA's counterpart of peer-reviewed formal professional papers but has less stringent limitations on manuscript length and extent of graphic presentations.

- TECHNICAL MEMORANDUM. Scientific and technical findings that are preliminary or of specialized interest, e.g., quick release reports, working papers, and bibliographies that contain minimal annotation. Does not contain extensive analysis.

- CONTRACTOR REPORT. Scientific and technical findings by NASA-sponsored contractors and grantees.

- CONFERENCE PUBLICATION. Collected papers from scientific and technical conferences, symposia, seminars, or other meetings sponsored or cosponsored by NASA.

- SPECIAL PUBLICATION. Scientific, technical, or historical information from NASA programs, projects, and missions, often concerned with subjects having substantial public interest.

- TECHNICAL TRANSLATION. English-language translations of foreign scientific and technical material pertinent to NASA's mission.

Specialized services that complement the STI Program Office's diverse offerings include creating custom thesauri, building customized databases, organizing and publishing research results . . . even providing videos.

For more information about the NASA STI Program Office, see the following:

- Access the NASA STI Program Home Page at ***http://www.sti.nasa.gov***

- E-mail your question via the Internet to help@sti.nasa.gov

- Fax your question to the NASA Access Help Desk at 301–621–0134

- Telephone the NASA Access Help Desk at 301–621–0390

- Write to:
  NASA Access Help Desk
  NASA Center for AeroSpace Information
  7121 Standard Drive
  Hanover, MD 21076

NASA/TM—2004-211991/PART2

# Turbomachine Sealing and Secondary Flows

## Part 2—Review of Rotordynamics Issues in Inherently Unsteady Flow Systems With Small Clearances

R.C. Hendricks
Glenn Research Center, Cleveland, Ohio

L.T. Tam
Lockheed Martin Space Systems Company, Sunnyvale, California

A. Muszynska
A.M. Consulting, Minden, Nevada

National Aeronautics and
Space Administration

Glenn Research Center

July 2004

Note that at the time of research, the NASA Lewis Research Center
was undergoing a name change to the
NASA John H. Glenn Research Center at Lewis Field.
Both names may appear in this report.

Available from

NASA Center for Aerospace Information
7121 Standard Drive
Hanover, MD 21076

National Technical Information Service
5285 Port Royal Road
Springfield, VA 22100

Available electronically at http://gltrs.grc.nasa.gov

# Turbomachine Sealing and Secondary Flows
## Part 2—Review of Rotordynamics Issues in Inherently Unsteady Flow Systems With Small Clearances

R.C. Hendricks
National Aeronautics and Space Administration
Glenn Research Center
Cleveland, Ohio 44135

L.T. Tam
Lockheed Martin Space Systems Company
Missiles & Space Operations
Sunnyvale, California 94089

A. Muszynska
A.M. Consulting
Minden, Nevada 89423

## Abstract

Today's computational methods enable the determination of forces in complex systems, but without field validation data, or feedback, there is a high risk of failure when the design envelope is challenged. The data of Childs and Bently and field data reported in NASA Conference Proceedings serve as sources of design information for the development of these computational codes. Over time all turbomachines degrade and instabilities often develop, requiring responsible, accurate, turbomachine diagnostics with proper decisions to prevent failures. Tam et al. (numerical) and Bently and Muszynska (analytical) models corroborate and implicate that destabilizing factors are related through increases in the fluid-force average circumferential velocity. The stability threshold can be controlled by external swirl and swirl brakes and increases in radial fluid film stiffness (e.g., hydrostatic and ambient pressures) to enhance rotor stability. Also cited are drum rotor self-excited oscillations, where the classic "fix" is to add a split or severed damper ring or cylindrical damper drum, and the Benkert-Wachter work that engendered swirl brake concepts. For a smooth-operating, reliable, long-lived machine, designers must pay very close attention to sealing dynamics and diagnostic methods. Correcting the seals enabled the space shuttle main engine high-pressure fuel turbopump (SSME HPFTP) to operate successfully.

**Keywords:** Turbomachine, seals, dynamics, antiswirl, CFD, models, fluid dynamic forces, rotor/stator clearances

## Introduction

Operating turbomachines by nature are unsteady systems. The fluid streamlines are interrupted, redirected, compressed, diffused, heated, and expanded by fixed and rotating discrete components with unsteady heat-release reactions. These same flows are also a source of rotor vibrations, which perturb the core and secondary flows, and in turn, propagate disturbances to other parts of the turbomachine. As an example, the NASA Energy Efficient Engine ($E^3$) aeronautical gas turbine

(Davis and Stearns, 1985) has 32 blades and 34 stators in the fan, 96 blades and 140 stators in the tenth stage (last) of the compressor, and 76 blades and 46 stators in the T1 turbine (first stage of the high-pressure turbine (HPT)). All provide very rapid, nearly periodic, high pressure and temperature variations in the flow field, and all require interface sealing and cavity load balancing with extreme care given to control of vibrations.

Gas turbines and rocket engine turbomachinery have similar interfacing, but the combination of cryogens, rapid startup, high rotor speeds, propellant-lubricated bearings, and dynamics are more severe in rocket engines. To this one must add noncentered orbitals and unsteadiness induced through eccentric thermomechanical loadings and transients associated with the vehicle flight profile (see part 3). Figure 1 illustrates the kinematics of the aeronautical gas turbine seal tip over the acceleration and full-power phases along with shutdown and soakback of a simulated flight profile, but without flight dynamics (engine on test stand).

In the past turbomachine rotordynamics have contributed to or been the direct cause of many design failures. With the maturation of the gas turbine and the demanding high-power-density rocket engine turbomachinery, most machines run stably. The exceptions arise when designers are either unaware or forced into a situation where the demands of the design outweigh the risks. In these situations the potential for failures becomes imminent whenever the design envelope is challenged or expanded. However, over time even the best of designs degrade with use, and many turbomachines in the field have encountered instabilities due to their operational time and the limited life of their components (see appendix B). As a result, it is generally accepted that no two engines operate the same or have the same time-variant signatures, even though they exhibit common fundamentals. Consequently, responsible, accurate turbomachine diagnostic techniques are required to identify root causes of impending malfunctions, with proper operator decisions leading to their prevention

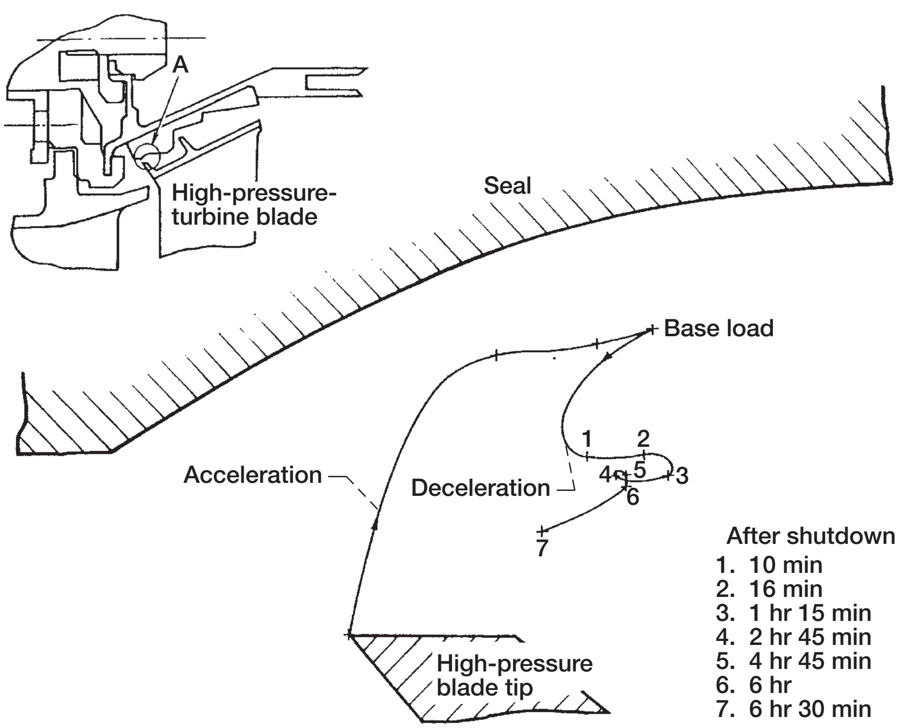


Figure 1.—Enlarged view (scale 50:1) of area A. Locus of high-pressure-turbine (HPT) blade tip seal relative to static seal during acceleration and full-power trip conditions. (Stewart and Brasnett, 1978.)

(Bently et al., 2002). However, these important issues will not be addressed herein as D.E. Bently's comprehensive book provides very adequate coverage of the subject with many examples, and we recommend the reader acquire the book.

Herein we review the inherent unsteady nature of the turbomachine with small-clearance components, specific operational problems of two turbomachine classes and their causes, fixes for instabilities, and the predictive methods of Tam et al. and Bently and Muszynska. In part 1 we review some sealing requirements and limitations from the viewpoints of the customer, designer, and researcher and the controls on the market. In part 3 we examine turbomachine internal flows, engine externals, and component life-cycle characteristics.

## Nomenclature

| | |
|---|---|
| $A$ | amplitude of rotor precession |
| $A_{ij}$ | normal velocity components induced at segment i by unit vortex strength along line segment j |
| $b$, $\alpha$ | coefficients in Prandtl mixing-length model |
| $C_p$ | specific heat |
| $C_{um}$ | average swirl speed |
| $c$ | bearing (or seal) radial clearance |
| $D$ | fluid radial damping; turbine diameter |
| $D_p$ | mean blade diameter |
| $D_R$ | rotor damping |
| $dv$ | transformed space volume element (+1) |
| $e$ | eccentricity |
| $\vec{e}(\vec{e}_1,\vec{e}_2,\vec{e}_3)$ | unit vector |
| $F_c$ | closing force |
| $F_d$ | dynamic force due to pressure |
| $F_g$ | force in seal gap |
| $F_s$ | spring force |
| $F_r$, $F_t$ | fluid dynamic radial and tangential forces, respectively |
| $F_x$, $F_y$ | equivalent radial and tangential forces in Cartesian coordinate system ($x$, $y$) |
| $F_z$ | fluid force |
| $\vec{g}$ | gravity vector |
| $H$ | blade height |
| $h_{\min}$ | minimum clearance |
| $h_{1,2,3}$ | scale factors in three coordinate directions |
| $J$ | determinant of Jacobian matrix |

| | |
|---|---|
| $j$ | $\sqrt{-1}$ |
| $K$ | fluid radial stiffness coefficient |
| $K_D$ | rotor or fluid direct dynamic stiffness |
| $K_d$ | rotor modal stiffness |
| $K_{\text{ext}}$ | external stiffness |
| $K_Q$ | rotor or fluid quadrature dynamic stiffness; lateral spring force coefficient |
| $K_{xy}$ | fluid tangential stiffness coefficient (cross-coupled stiffness), $F_t/\varepsilon$ |
| $K_0$ | fluid film stiffness |
| $K_1$, $K_2$ | shaft partial stiffnesses, left and right sides, respectively |
| $k_1$, $k_2$ | friction coefficients on rotor and eddy chamber or labyrinth chamber surfaces, respectively |
| $k$-$\varepsilon$ | turbulence energy production-dissipation |
| $L$ | blade length |
| $l$ | seal or bearing length |
| $l_m$ | mixing-length scale of seal |
| $M_d$ | rotor modal mass |
| $M$, $M_f$ | fluid inertia |
| $M_1$, $M_2$ | disk and journal masses |
| $\dot{m}$ | mass flow |
| $m_n$ | number of labyrinth chambers |
| $m_2$ | mass of unbalance |
| $N$ | number of distributed line segments |
| $n_i$ | unit normal vector |
| $P$ | rotating force |
| $P_s$ | static pressure |
| $P_{\text{in}}$, $P_{\text{out}}$ | inlet and outlet axial pressures |
| $\Delta P$ | axial pressure drop, $P_{\text{in}} - P_{\text{out}}$ |
| $p$ | fluid pressure |
| $Q$ | source flow; carrying force; lateral force |
| $[Q]$ | nondimensional force |
| $q$ | dynamic pressure |
| $R$ | seal rotor or bearing radius; Richardson flux number |
| $R_i$ | shaft radius |
| $r$ | fluid local radius in bearing or seal clearance; radius of imbalance |
| $\vec{r}$ | displacement vector |

| | |
|---|---|
| $S$ | source terms |
| $T$ | torque |
| $T_{\text{in}}$ | inlet temperature |
| $T_0$ | torque at average tip clearance |
| $T_1$ | torque at maximum tip clearance |
| $T_{\text{total}}$ | total torque of all turbine blades |
| $t$ | time |
| $\vec{U}$ | fluid relative velocity vector |
| $\vec{U}_{\text{abs}}$ | fluid absolute velocity vector |
| $\vec{\tilde{U}}$ | reference frame velocity vector |
| $u$ | local velocity |
| $\tilde{u},\tilde{v}$ | reference frame circumferential and radial velocity components, respectively |
| $V_{\text{ps}}$ | preswirl circumferential velocity at radius $r$ |
| $V_{\infty,i}$ | velocity at midpoint of segment i |
| $\text{Vol}_{\text{cell}}$ | physical volume of grid cell |
| $x$, $y$, $z$ | shaft horizontal, vertical, and radial complex displacements |
| $Y_0$ | rotor offset |
| $z$ | axial Cartesian coordinate in bearing or seal; shaft radial complex displacement, $x + jy$ |
| $z_r$ | radial displacement magnitude of $z$ |
| 0 | null matrix |
| $\alpha$ | phase; $(T_1 - T_0)/T_0$ |
| $\beta$ | destabilizing stiffness parameter, $\alpha/(2\varepsilon RF_t)$ |
| $\gamma$ | ratio of specific heats; ratio of hole surface area to seal surface area |
| $\gamma_j$ | local vortex strength |
| $\delta$ | average damping coefficient; displacement |
| $\varepsilon$ | eccentricity ratio, $e/c$ |
| $\vec{\varepsilon}$ | contravariant base vector |
| $\zeta$ | normal distance between housing and shaft (stator and rotor) surfaces |
| $\eta$ | purge flow efficiency parameter; viscosity |
| $\theta$ | angular position of tangential force |
| $\Gamma$ | vortex strength |
| $\lambda$ | fluid average circumferential velocity ratio |
| $\lambda_e$ | preswirl-related fluid average circumferential velocity ratio |

| | |
|---|---|
| $\lambda_{\text{ext}}$ | external fluid average velocity ratio |
| $\lambda_i$ | injection-related fluid average circumferential velocity ratio |
| $\lambda_n$ | nonlinear function of fluid average circumferential velocity ratio |
| $\mu_t$ | turbulent viscosity; rotor orbital velocity |
| $\nu$ | fluid kinematic viscosity |
| $d\xi^{1,2,3}$ | transformed-space arc lengths in three coordinate directions |
| $\rho$ | fluid density |
| $\tau$ | stress tensor |
| $\Phi$ | angular coordinate in bearing or seal |
| $\phi$ | rate of strain in Newtonian fluid; angle measured from position of minimum clearance |
| $\psi$ | load factor |
| $\psi_1, \psi_2$ | nonlinear stiffness and damping functions |
| $\Omega$ | rotation; onset speed |
| $\omega$ | rotor speed |
| $\omega_{\text{cr}}$ | critical speed |
| $\omega_n$ | whirl |
| $\omega_P$ | rotor precession (perturbation) frequency, or angular velocity |
| $\omega_R$ | rotational speed |
| $\omega_R^{\text{ST}}$ | rotor stability threshold |
| $\omega_1, \omega_2$ | horizontal and vertical oscillation, respectively |
| $\nabla$ | gradient |

**Superscripts:**

| | |
|---|---|
| $\rightarrow$ | denotes vector |
| $\approx$ | denotes tensor |

**Nomenclature for Thomas (fig. 4):**

| | |
|---|---|
| $A$ | flow area |
| $C_E^*$ | ratio of flow kinetic energy to shroud pressure difference, $\rho C_{1u}^2 / 2\Delta p_B$ |
| $C_{1u}$ | tangential component of absolute outlet velocity of stator blade flow |
| $\Delta h_{\text{is}}$ | stage isentropic enthalpy difference |
| $K_2$ | clearance excitation coefficient, $ql/U_{\text{is}}$ |
| $l$ | unit length of rotor blade |

| | |
|---|---|
| $m$ | stage mass flow |
| $\Delta p_B$ | pressure difference at the shrouding |
| $q$ | clearance excitation cross-force spring coefficient, $q_S + q_D$ |
| $U$ | velocity |
| $U_{is}$ | isentropic tangential force, $m\Delta h_{is}/u$ |
| $u$ | average circumferential velocity |
| $\varepsilon$ | eccentricity |
| $\varepsilon q_D$ | pressure distribution portion of $q$, $\propto \int \sin \varphi \, dA$ |
| $\varepsilon q_S$ | clearance loss portion of $q$, $\propto \int \cos \varphi \, dU$ |
| $\rho$ | density |
| $\varphi$ | circumferential angle |
| $\psi$ | load factor, $2\Delta h_{is}/u^2$ |

**Nomenclature for Benckert (figs. 8 to 10 and eq. (1)):**

| | |
|---|---|
| $C_{u0}$ | entry swirl speed |
| $e$ | eccentricity |
| $h$ | ratio of cavity to rotor height (cell depth) |
| $K_Q$ | tangential spring force coefficient |
| $l$ | seal length |
| $m$ | number of chambers |
| $P_a$ | ambient pressure |
| $P_T$ | torque or tangential force |
| $P_0$ | upstream pressure |
| $Q$ | lateral force |
| $r$ | rotor radius |
| $t$ | cell width |
| $U_w$ | rotor speed |
| $\varepsilon$ | relative eccentricity, $e/\Delta r$ |
| $\rho_0$ | upstream density |

**Glossary:**

We include a glossary because various authors use the same name for different phenomena and/or different names for the same phenomenon.

Whirl — Whirl is used in general as a synonym of rotor precession or (better) lateral orbiting. Whirl is also used to describe specific self-excited vibrations of the rotor, such as fluid whirl. Also oil whip, steam whip, aerodynamic whip, fluid-induced instability, clearance excitation, half-speed whirl, and probably even more names, describe the same phenomenon: self-excited vibration of rotors due to forces in a fluid environment.

Swirl — Swirl in seals represents circumferential flow in the direction of rotation. The flow is, of course, three dimensional and might be unsteady, but the existence of swirl means that in the rotor/seal clearance a significant circumferential flow has been established. Active antiswirl injections, as well as passive preswirl (constant tangential vanes at the entrance to the seal) techniques, clearly were developed to prevent this circumferential flow in the seal from being significant.

$\lambda$ — The product of fluid circumferential velocity ratio times rotational speed $\lambda\omega_R$ is the speed at which the fluid force rotates inside the clearance (i.e., the ratio at which the fluid force rotates relative to the rotor speed) and is especially important in the damping force because the fluid inertia force may rotate at a different rate. If the circumferential flow in the clearance is modified by an external source requiring application of some outside energy, $\lambda$ may become larger than ½, or even negative. For example, if there are injections (such as antiswirl in the direction against rotation), the circumferential flow is modified. If this external source is very strong, to the point where the circumferential flow is in the direction opposite to rotation, $\lambda$ may become negative; however, it is then probably inconvenient to relate it to the rotational speed. If the injections are in the direction of rotation, $\lambda$ becomes greater than ½, depending on the amount of injected fluid. Note that $\lambda$ higher than ½ occurs normally in pumps with high fluid recirculation. In such cases the self-excited fluid whirl has frequency higher than ½ rotor speed.

## Cases of Small Clearances Between Rotating and Stationary Parts

### Seals and Bearings

Although the primary function of a seal is to control leakage, a secondary but equally important purpose is to provide (or at least not to infringe on) rotordynamic stability. Bearings also have a dual role, to support the rotor load and to provide dynamic stability. Seal and bearing combinations can be used to enhance stability as well as to decrease bearing loads (von Pragenau, 1992; Munson et al., 2002; and Bently, 2001). Von Pragenau's work was so good that Rocketdyne patented the concepts. More recent work on fluid film bearings was done by Dimofte and Hendricks (2001), Bently (2001), and Bently et al. (2002).

Further, the flow fields in bearings and seals have similarities, although with some distinct differences. The axial pressure drop in the seal is large, and the circumferential pressure drop is nominally smaller with coupling to structure, cavity flows, and the power stream (see part 3). For the bearing the opposite nearly holds true except that coupling to the power-stream flow is indirect. Further, zones of secondary flow appear inevitable. Cavitation phenomena can occur in both bearings and seals in the form of either gaseous cavitation (pressure lower than atmospheric) or vaporous cavitation (pressure lower than saturation pressure). For these complex flows local bulk flow model physics are inadequate, but in many cases the model adequately predicts system dynamics and has been successfully used by many authors (e.g., Muszynska, 2001; and San Andres and Childs, 1997). Seal or bearing design using computational fluid dynamics and knowledge-based methodologies can enhance turbomachine stability. (See part 1 and computational methods and CFD modeling in part 3).

Simplifications that incorporate first-order physics are often used in modeling complex flows. In this respect a more complete modeling of the turbomachine operating conditions, loads, and supports is sought because rotor (component) resonances can occur far from critical and single-point sensing can fail to warn of impending failure (Queitzsch and Fleming, 2001). Although their examples are related to rolling-element bearings, these same principles are applicable to interactions between small-clearance fluid films and system dynamics throughout the turbomachine.

### Seal/Structure Interaction

When the clearance gap varies with time, lateral forces occur that act out of phase with case distortion. Depending on changes in gap in the flow direction, excitation or damping of the lateral forces occurs. The rotating drums shown in figures 2 and 3 represent very large energy storage systems that must be properly contained. For example, a 356-kN- (80-klb-) thrust engine stores 8 MJ

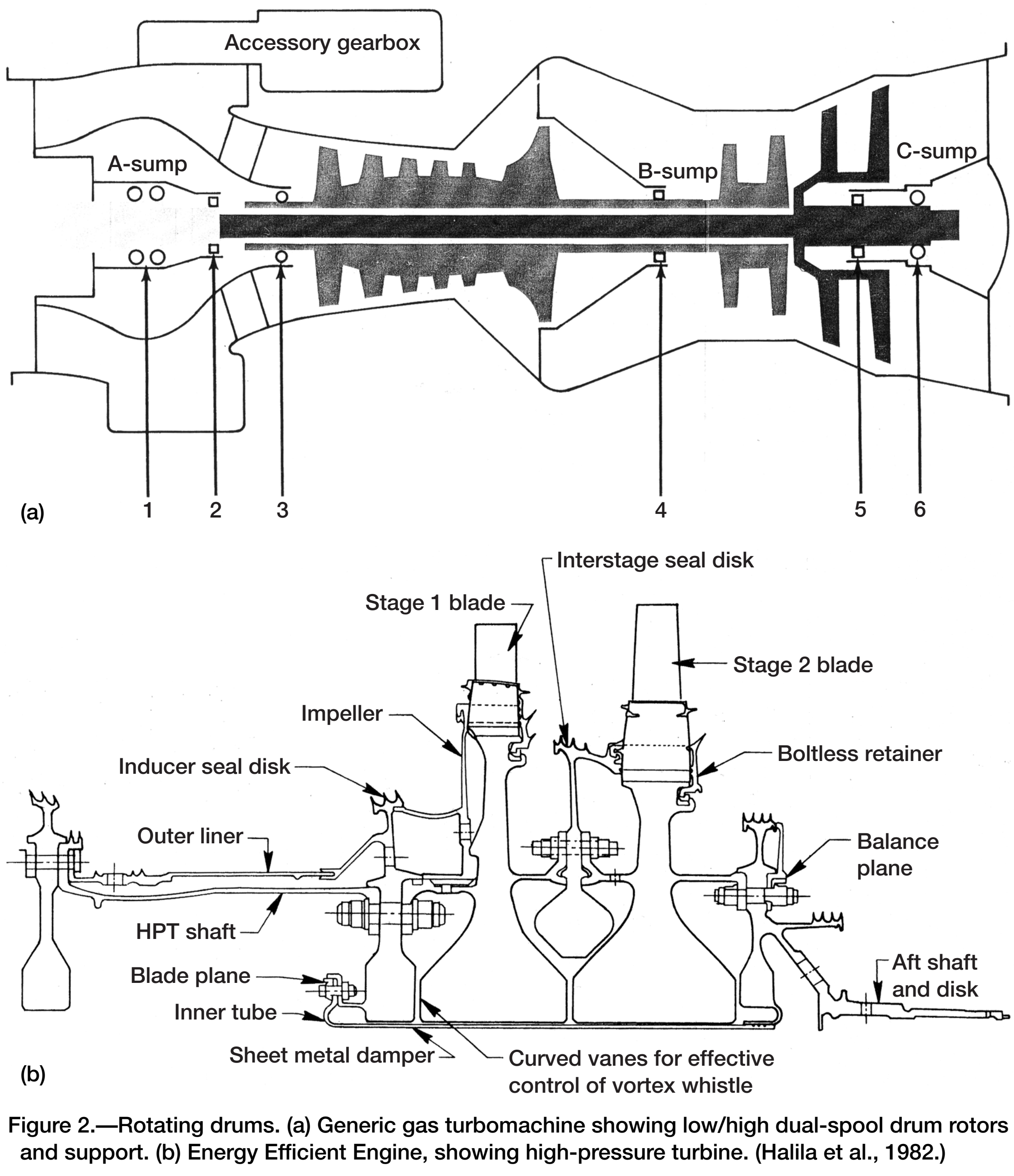


Figure 2.—Rotating drums. (a) Generic gas turbomachine showing low/high dual-spool drum rotors and support. (b) Energy Efficient Engine, showing high-pressure turbine. (Halila et al., 1982.)

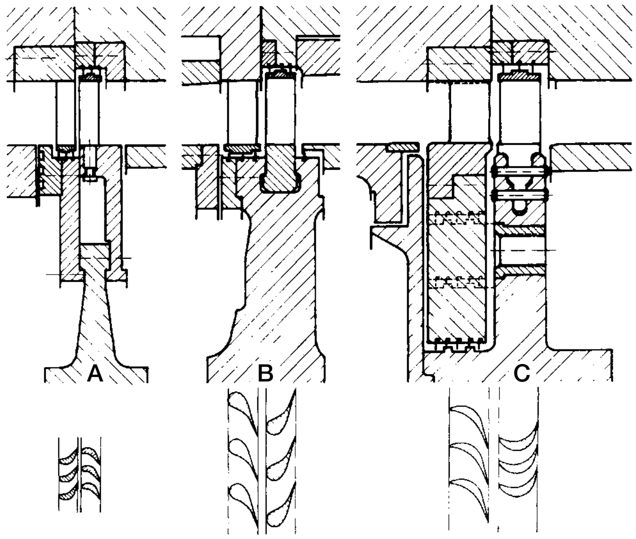


Figure 3.—Steam turbine stage types investigated. (Leie and Thomas, 1980.)

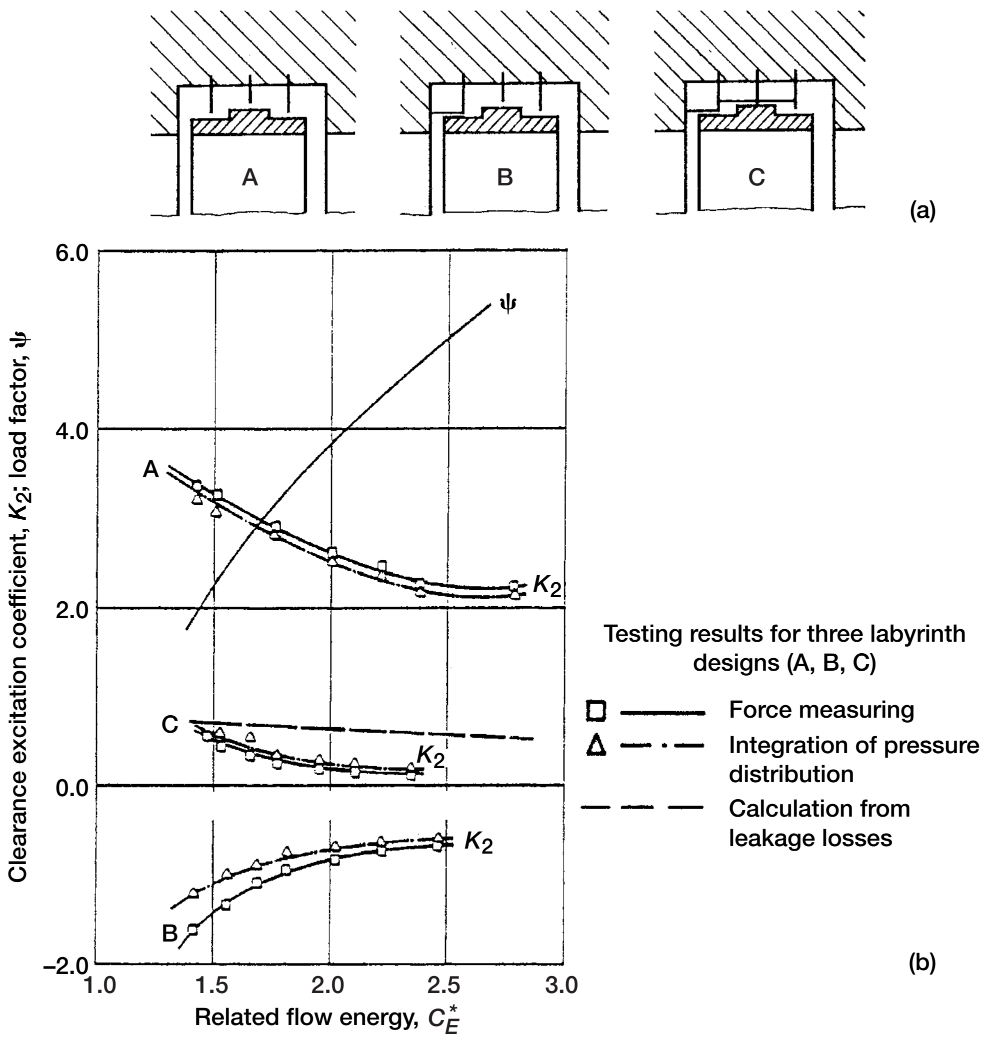


Figure 4.—Steam turbine instabilities. (a) Three labyrinth seal configurations investigated. (b) Test results. (Leie and Thomas, 1980.)

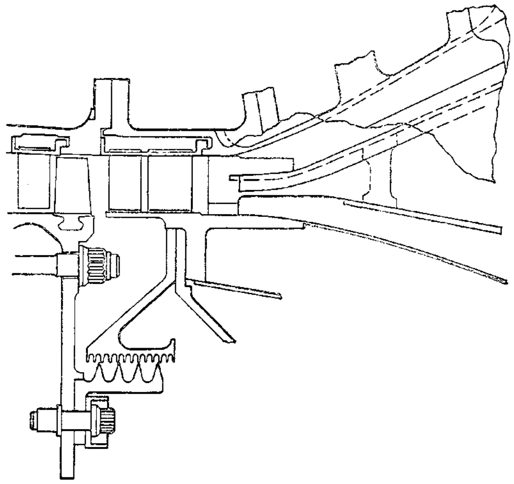

Figure 5.—Compressor discharge annular diffuser. Where compressor discharge seal is at a substantially smaller diameter than inner wall of main flow annulus, check for possible cross flow and cellular recirculating flows between wheel space chamber and diffuser inlet. (Alford, 1967.)

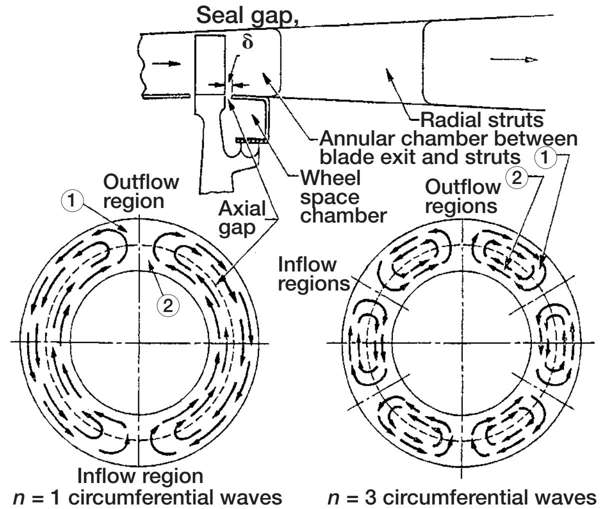


Figure 6.—Wheel space chamber coupled to diffuser inlet. Where an axial gap connects wheel space chambers and diffuser inlet, cellular recirculating flows may occur. (Alford, 1967.)

in the high-pressure turbine (HPT) rotor system and 18 MJ in the total engine; a 445-kN- (100-klb-) thrust engine stores 18 MJ in the HPT rotor system and 60 MJ in the total engine.

Early on, Smith (1933) studied the stability of rotating systems and reported that stationary damping in bearing supports always favors stability but that damping in rotating parts should be avoided when the machine has to run above a critical speed. He believed that unsymmetrical flexible bearing supports may improve running (asymmetry is to be avoided in shafts and rotors) and cautioned not to run at speeds close to critical or to half one of the normal frequencies of the system. Sometimes this anisotropy is unavoidable (as in two-pole generators).

Some 25 years later self-excited vibrations engendered by forces of the fluids being processed were investigated by Thomas (1958) (see also NASA CP–2133, 1980, p. 303, fig. 3), who looked into steam turbine whirl excitation. For a bearing, in certain respects, stiffness and damping in themselves are not so important, but their relation to one another is important. Clearance excitation forces emerge from nonuniform flows (leakages) and pressure distributions as a function of eccentricity. Thomas introduced swirl-preventing sheets of metal that reduced or eliminated the excitation forces (fig. 4), where the clearance excitation coefficient $K_2$ and load factor $\psi$ are plotted against the ratio of flow kinetic energy to shroud pressure difference $C_E^*$.

Alford (1963, 1965, 1967) followed with a series of papers establishing some methods of controlling instabilities in aeronautical turbomachines. All or nearly all unstable and oscillatory flows are self-excited by flow systems with rising pressure characteristics (one in which the internal pressure increases with an increase in flow), such as every cycle in an eccentric seal, housing, bearing, or compressor (fluid-handling machines in general). Tangential air velocity has a primary effect on resonances with circumferential waves. Phase differences between longitudinal waves in parallel diffuser passages give rise to spinning pressure waves in adjacent annular ducts (figs. 5 and 6). Resonance occurs when the space oscillations and spinning waves are the same for the wheel and disk (reminds one of Ben Franklin's glass harmonica). Alford employed principles of designing high-frequency waveguides in his analytical work.

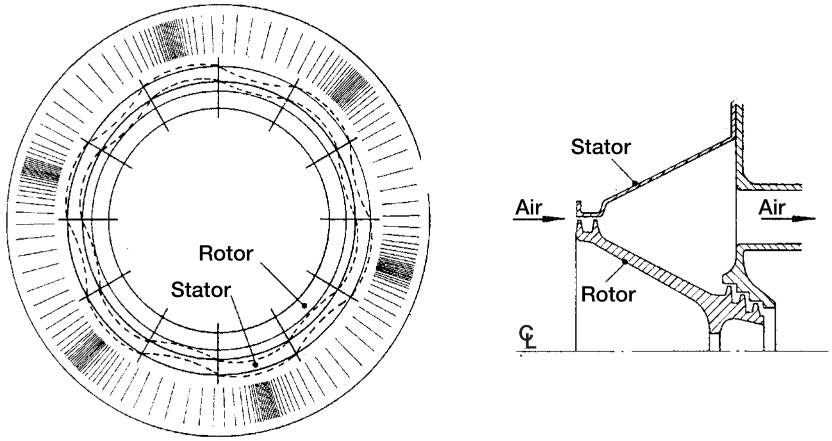


Figure 7.—Labyrinth seal vibrations. (Armstrong, E.K., discussion of Alford, 1967.)

### Self-Excited Seal Drums

***Description***.—In a discussion of Alford's paper (1967), E.K. Armstrong cited cracking in the compressor-discharge-pressure (CDP) labyrinth seal stator drum. In this case the stator vibrated to 1300 Hz (perhaps similar to a more recent engine failure problem) with 6 nodal diameters and 12 nodes with a distortion (fig. 7). At a certain temperature the frequency of mode vibration in the annular air cavity with six wavelengths becomes equal to the sixth diametrical mode of the stator ($\pi D/6$). Under these conditions variation in the air gap in the labyrinth due to the stator vibration excites vibration in the cavity. In turn the resulting pressures act upon the stator, and if the phase is correct, self-excited oscillations occur. The mechanism could be stopped by inserting 24 equally spaced radial baffles across the air cavity (phase and baffles are cited by Thomas, 1958). Alford comments that the mechanism that excites the labyrinth seal stator appears to be the same phenomenon that excites the labyrinth seal rotors.

Below are "rules of thumb" that exist in the field. These rules are listed here without specific classification and without any evaluation for applicability. Therefore, they are often misused.

***Some rules of thumb***.—Prevent parasitic leakages. Provide radial baffles near the wheel rim to prevent cellular recirculation. Provide a cylindrical surface adjacent to the baffle to ensure that a minimum area of the flow communication slot is independent of axial motion. Reduce swirl entering the diffuser. Provide a margin greater than 15 percent between resonant longitudinal waves and wheel space waves. If inlet flow is split, extend the duct splitter to the compressor inlet to prevent crossflow between inlets. Provide adequate radii on passage leading edges to prevent vortices and flow disruption, particularly flow separations. Check rotor blade excitation modes for excitation and avoid them. Dynamically monitor parameters (e.g., with proximity probes).

The work of Benckert and Wachter (1978, 1980) set the stage for further understanding the basic forces in turbomachines and the advancement of seal flow inlet swirl as a major source of high-power-density turbomachine seal instabilities.

### Swirl Brakes

Although known and reported by Thomas and Armstrong, from the work of Benckert and Wachter came the widely acclaimed swirl brake, which did solve several labyrinth seal instability

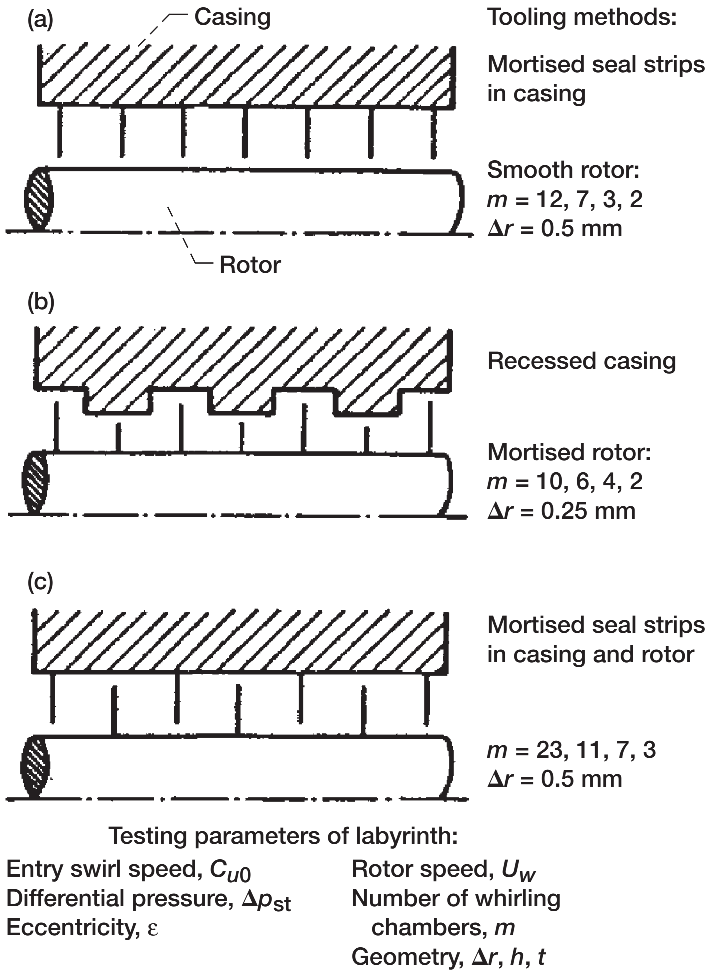


Figure 8.—Close-clearance labyrinth shaft seals, circumferential types. (Benckert and Wachter, 1978.)

problems in U.S. industrial power turbines. In their work Benckert and Wachter (1978) studied (1) teeth on stator, smooth rotor; (2) teeth on rotor, recessed stator; and (3) interlocking teeth on rotor, teeth on stator (fig. 8). They found that lateral forces related to circumferential flows are detrimental to rotor stability and that blocking the flow could control these perturbations (fig. 9). Here the lateral spring force coefficient $K_Q$ is given as a function of rotor relative eccentricity $\varepsilon$; $K_Q$ can be estimated from the swirl speed and for see-through labyrinths

$$2(K_Q h/r^2)^2 \propto \rho_0 C_{u0}^2 (P_0 - P_a) \tag{1}$$

For more established flows

$$[K_Q (h/r)^2/\pi] = m_n \rho_m [(k_1 - k_2)\, C_{um}^2 + k_2 C_{um} U_w] \tag{2}$$

where the subscript $m$ is the average value in the labyrinth chamber, $m_n$ is the number of labyrinth chambers, $k_1$ is the friction coefficient on the rotor, $k_2$ is the friction coefficient on the eddy chamber or labyrinth chamber surfaces, and $C_{um}$ the average swirl speed. (See also Muszynska's lumped-parameter model in part 2 of appendix A.)

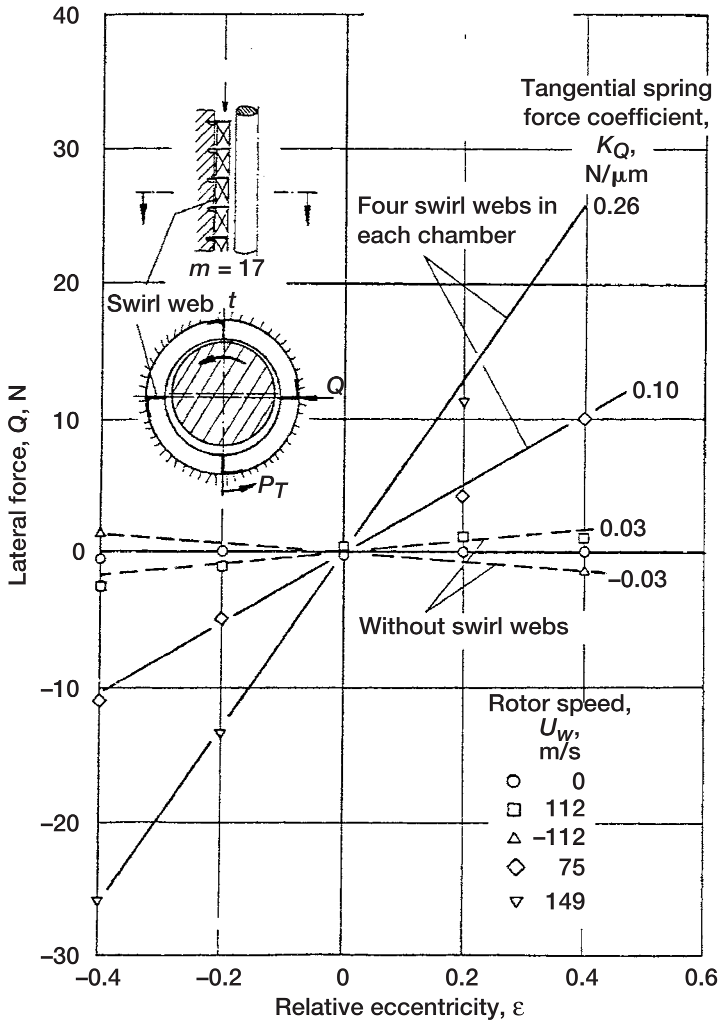


**Figure 9.—Speed-induced lateral forces by using swirl webs in each eddy chamber of labyrinth. Tangential spring force coefficient, $P_a/P_0$ = 0.49, $h$ = 2.75 mm. (Benckert and Wachter, 1980.)**

According to Benckert and Wachter (1978) the swirl brake work was an outgrowth of a description in Wohlrab (1975, translated in 1983) where a steam turbine was stabilized by placing the brake upstream of the first tooth to redistribute the entry flow in the seal and control the circumferential flow in the chambers. Benckert and Wachter also studied two sizes of honeycomb, 4.95-mm (0.195-in.) cell by 3.75-mm (0.148-in.) depth and 3.55-mm (0.140-in.) cell by 2.75-mm (0.108-in.) depth. They showed relative lateral (destabilizing) forces an order of magnitude larger than for the interlocking labyrinth (fig. 10). Iwatsubo and Iwasaki (2002) evaluated a swirl brake and a labyrinth seal similar to those of Benckert and Wachter. Iwatsubo and Iwasaki found that adding control fins in the labyrinth grooves was effective in reducing the circumferential swirl velocity and that adding control fins at the inlet, particularly the first and second grooves, controlled seal stability. This effect was predicted by Tam et al. (1988) (see the section Computational Method of Tam et al. and part 1 of appendix A). In yet another method termed a web seal (appendix B), slots are introduced to enhance stability.

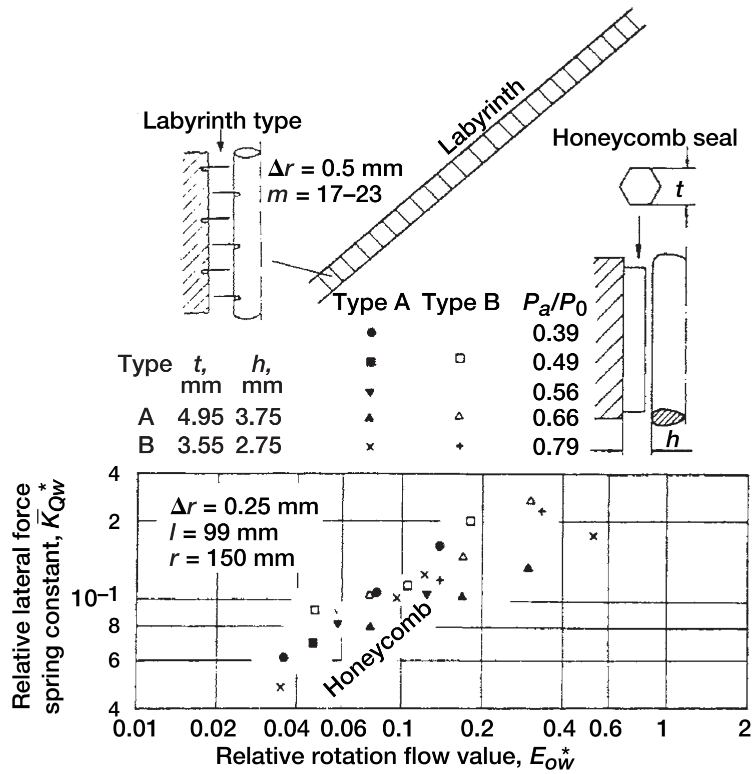


**Figure 10.—Lateral force spring coefficients as function of relative rotation flow value for two honeycomb seals. Seal clearance, *r*, 150 mm; Δ*r*, 0.25 mm; seal or bearing length, *l*, 99 mm. (Benckert and Wachter, 1980.)**

## Pumps and Impellers

Henry Black contributed heavily to the rotordynamics field. Black (1968) analyzed annular clearance spaces of impeller and balance piston seals. He found large damping associated with squeeze of the fluid to be comparable to stiffness. With dominant inertia effects, apparent negative stiffness can occur (see appendix A). Analysis gives synchronous critical speeds, whirl amplitudes, and whip boundaries. Fluid rotation in synchronous whirl reduces the damping forces. At high speeds fluid rotation may lead to whip, which can be avoided by tightening the clearances but could occur as the seal wears.

Thompson (1980) analyzed 115 individual compressor stages contained in 20 multistage bodies and concluded that the average damping coefficient δ per stage to ensure stability is

$$\delta_{\mathrm{total}} = 1.85 = \delta_{\mathrm{fluid}} + \delta_{\mathrm{mechanical}} \qquad \text{and} \qquad \delta_{\mathrm{fluid}} = -F_1/u_t \tag{3}$$

where $F_1$ is the cross-coupled force component (tangential force) due to dynamic excitation and $u_t$ is the rotor orbital velocity. Thompson also cites the opportunity to add damping to avoid the effects of compressor surge.

Colding-Jorgensen (1980) modeled the centrifugal compressor or pump stage with a vaneless volute based on a two-dimensional representation of the diffuser and impeller by an equivalent vortex of strength Γ and a source flow $Q$ at a point. The velocity at any point is the sum of the velocities induced by singularities in the field

$$\sum A_{ij} \gamma_j = V_{\infty,i}\, n_i \tag{4}$$

where $V_{\infty,i}$ is the velocity at the midpoint of segment i, $n_i$ is the unit normal vector, and $A_{ij}$ are the normal velocity components induced at segment i by unit vortex strength along line segment j. The sum is over the $N$ distributed linear segments along unit length line segments j covering the volute. The $N$ sources at the midpoints are the unknown local vortices of strength $\gamma_j$ induced at point i. The velocity $V_{\infty,i}$ is induced by the vortex ($\Gamma$, $Q$) representing the impeller at a given eccentricity and velocity of the vortex source. Once the solution for $\gamma_j$ is achieved, the velocity at any point in the plane can be found. (See also NASA CP–3344, p. 177.)

## Effect of Damping

Although it was noted by Smith (1933) sometime earlier, Crandall (1980) provides a limited explanation of how rotating damping can destabilize a rotating system. When rotation $\Omega$ is faster than the whirl $\omega_n$, rotating damping drags the rotor along; and when slower, it retards the rotor. When stationary damping is present, the stability line is balanced by backward and forward drag forces. At low rotational speeds the rotating (internal) damping force in rotating elements acts collinearly with the external damping force (damping in nonrotating elements and the rotor environment); at high rotational speeds the rotating damping force changes the polarity—thus, it opposes external damping up to its nullification. A forward whirl at rate $\omega_n$ with respect to stationary axes appears as backward whirl at a rate of $\Omega - \omega_n$ with respect to a system rotating supercritically at rate $\Omega$. Growth or decay is estimated from the energy balance. If the system is horizontal and elastically supported (e.g., compliance is greater in the $x$ direction than in the $y$ direction), the system becomes a superposition of a horizontal oscillation $\omega_1$ and a vertical oscillation $\omega_2 > \omega_1$. The more anisotropic the supports, the greater the difference between $\omega_1$ and $\omega_2$, and there is no tendency to set up a whirl of the type that can be dragged forward by rotary damping until these forces have been increased by risings in speed to be commensurate with the difference in elastic forces in the two principal directions. Thus, anisotropic bearing supports should raise the onset speed $\Omega$ for instability due to rotating damping. Nevertheless, the pendulum in the rotating coffee cup explanation for a fluid film bearing when its rotational speed exceeds 2× (twice the critical speed of the rotor) is also interesting.

As a possible illustration Crandall considered a thin fluid layer in a cup rotating at $\Omega$, a pendulum in the fluid layer rotating at $\omega_n$ (both in the counterclockwise direction (fig. 11)). When $\Omega < \omega_n$, fluid drag retards the pendulum bob and the radius of the orbit decreases. On the other hand when $\Omega > \omega_n$, fluid drag pulls the pendulum bob around in an orbit and the radius increases—a possible explanation for whip when $\Omega > 2\omega_n$. Here, Crandall assumes that $\lambda = 0.5$. The more general assumption that $\lambda$ is not constant and, in particular, differs from 0.5 opened new insights into the fluid forces acting on rotors in relatively small clearances (see part 2 of appendix A). Note that for the same rotor model the fluid whip condition used in the Bently-Muszynska fluid model is $\Omega = \omega_n / \lambda$. Because $\lambda$ can be modified (e.g., by swirl brake, fluid injection, or applied pressure), Crandall's instability threshold also can be modified. An example is given in part 2 of appendix A.

For a more complete assessment of theory, data, and analysis in the development of seals-related instability problems and their solutions and seals and secondary flow codes development, see a NASA Conference Publication as given in the references. For further work in the area of pumps and turbomachines contact

Dara Childs, Texas A&M Pump Consortium Meetings, College Station, Texas
Allen Acosta and Chris Brennen, CalTech, Pasadena, California
Yoshinobu Tsujimoto, Osaka University, Osaka, Japan/ ISROMAC–9, Hawaii, 2002

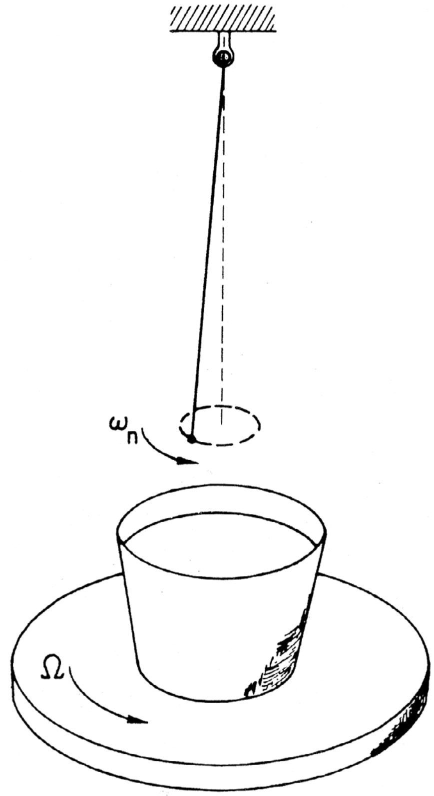


Figure 11.—Rotating coffee cup illustration. (Crandall, 1980.)

Bently Pressurized Bearings Company
NASA Conference Proceedings

It was from these and other field experiences that the space shuttle main engine turbomachinery field came to realize the importance of lateral forces that destabilize the rotor and the importance of upstream correction of the inlet swirl. In some seals the swirl brake mitigates those forces. The effort to control circumferential flow continues to this day (see appendix B).

## Turbomachines With Specific Operational Problems

### High-Power-Density Turbomachines

Let us digress for a moment as some background seems in order. For more complete work, see books by Childs (1993) and Vance (1988); and for diagnostics see Bently et al. (2002). As noted, steam turbine seal leakages were investigated by Thomas and later by Alford for aeronautical turbine rim seals. Although the destabilizing forces of bearings were somewhat recognized and resolved, the forces in seals of the space shuttle main engine high-pressure fuel turbopump (SSME HPFTP) were not. Instabilities in the SSME HPFTP caused many failures and prompted Otto Goetz (chief engineer) and his group (e.g., George von Pragenau, Henry Black, Ed Gunter, Larry Ludwig, Dara

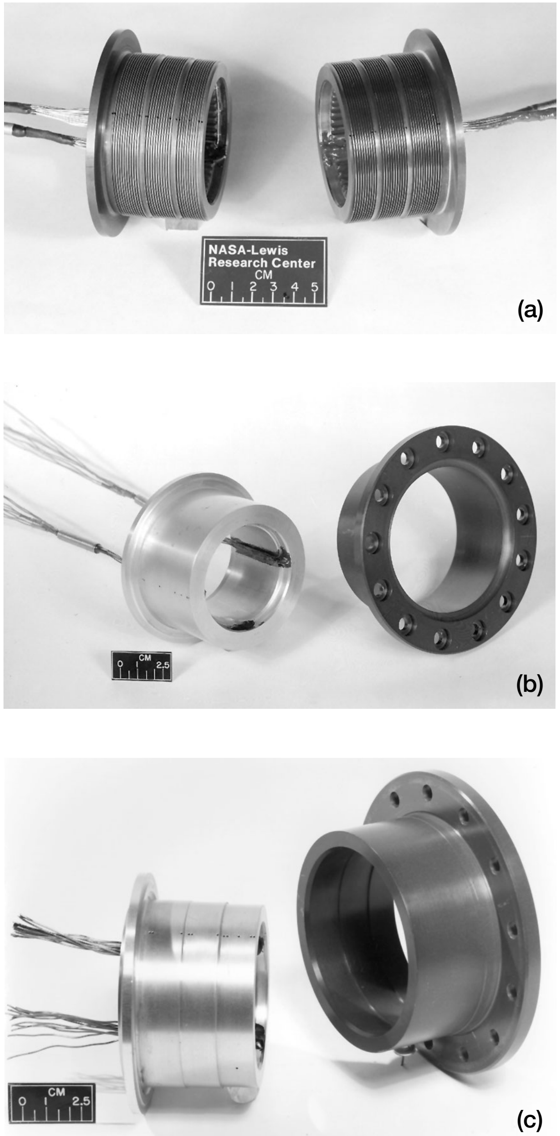


Figure 12.—High-pressure fuel turbopump (HPFTP) shuttle seal. (a) Three-step labyrinth. (b) Straight cylindrical. (c) Three-step cylindrical. (Hendricks, 1981a,b,c.)

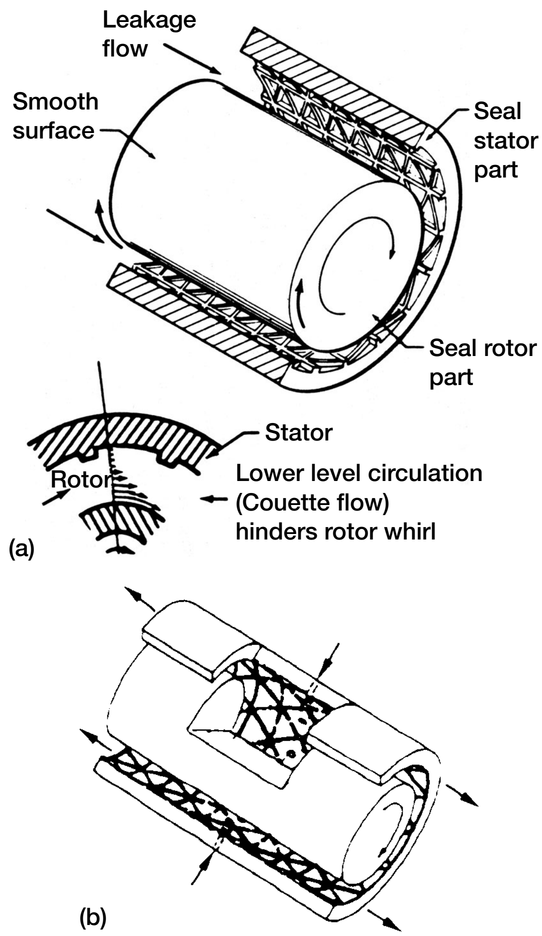


Figure 13.—Damping seals and bearings. (a) Damping seal concept with isogrid stator. (b) Damping bearing concept with stationary orifices (orifices can also be in the shaft). (Inventions of George von Pragenau, Huntsville, Alabama; Hendricks et al., 1995.) See also part 1, figure 33.

Childs, and others) to propose investigating the seals as a probable cause. Goetz suggested full-scale testing of the HPFTP seals in a simulated, nonrotating configuration. Hendricks tested and later published dynamic force data for three seal configurations (labyrinth, cylindrical, and stepped cylindrical) with cryogenic and gaseous hydrogen as the working fluid for a range of conditions. These data along with the stability and damper seal concepts of von Pragenau (1982, 1985) served as guidelines for subsequent turbopump refurbishment (Hendricks, 1981a,b,c) and kept the space shuttle "flying" until a better understanding emerged (figs. 12 and 13). *Correcting the seals enabled the SSME HPFTP to operate successfully.*

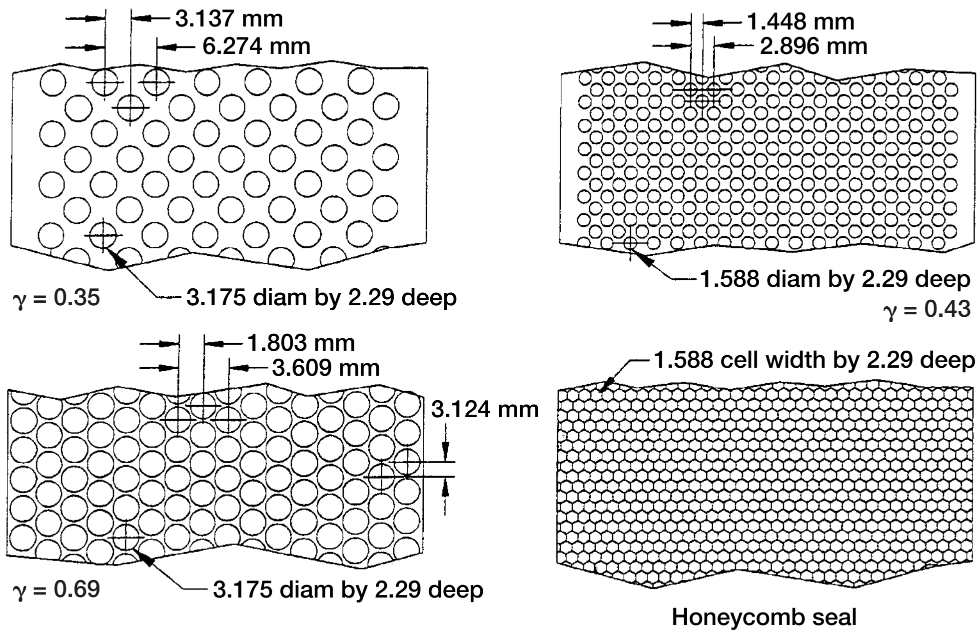


Figure 14.—Hole patterns for damper seals, where $\gamma$ is ratio of hole surface area to seal surface area. (Yu and Childs, 1997.)

These turbopump instability problems led Prof. Childs to organize the first seals and rotordynamics workshop at Texas A&M as reported in NASA CP–2133 (in retrospect, a classic document). A dearth of data and a wealth of seal instability problems coupled with little understanding of sealing forces in high-power-density turbomachines dominated the workshop. As understanding began to emerge, the results were documented in NASA Conference Publications (see references). A sampling of topics include field test data, seal dynamic coefficient measurements, analytical methods, numerical techniques, and practical applications. Computational fluid dynamics (CFD) has merged the classical dynamics approach with that of the actual flow field, with some success in describing these forces. Damping concepts of von Pragenau have been extended to a variety of hole patterns (fig. 14). Swirl brakes and antiswirl methodology have been applied with significant success (fig. 15). Design data, from foreign and domestic sources, provided dynamic coefficients; and the data of Braun et al. (1987) quantified the flow fields near the minimum clearance for both the convergent and divergent zones of a simulated bearing. Seals began to play a prominent role in stabilizing turbomachines, and some understanding of sealing forces in high-power-density machines began to emerge, although the details continue to be analyzed yet today.

The Benckert and Wachter explanations led rotordynamicists such as Crandall to also give explanations of the instability problems; Black, Fleming, Vance, Childs, Gunter, and others provided theoretical analyses. NASA initiated two programs, one with Childs dealing with seal rotordynamic instabilities and the other to design seals and secondary flow systems. The rotordynamics program with Childs provided data, analysis, and biannual workshops that over the years enabled a considerable degree of confidence to emerge within the turbomachinery community. NASA initiated the development of the computer codes SCISEAL and INDSEAL with progress of the seals community reported at workshops on an annual basis. Later San Andres developed TAMSEAL. These codes were an outgrowth of the need to capture experience, data, and analysis into code form for seal and secondary flow designers.

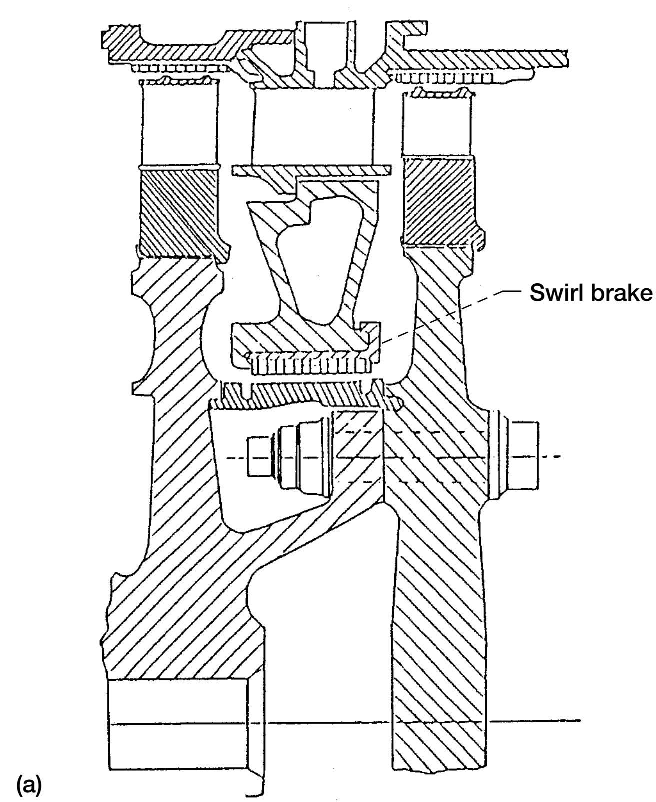


Figure 15.—High-pressure oxygen turbopump (HPOTP). (a) Interstage seal (relative dimensions not to scale). (b) Radial swirl brake. (c) Improved swirl brake. (Childs et al., 1991.)

A long series of experimental seal testing by Childs, Vance, Iwatsubo, San Andres, Bently, Muszynska, and Allaire providing dynamic coefficients, analytical methods (Fleming,[1] Gunter, Nelson, Black, Brown, Muszynska, Bently, and others), and computational techniques (Tam, Przekwas, Rhode, Nordmann, Athavale, San Andres, and others) began to replace the data and analysis dearth with credibility and served as the basis for codes developments and analysis. The CFD numerical work of Tam et al., to be discussed later, in terms of dynamic stiffness, and the works of Nordmann that centered on flow CFD and the small-perturbation method with cross-coupled terms paved the way for use of CFD modeling with full-field-coupled conjugate solutions developed by Athavale (see part 3).

Spurred by the many industrial field instability problems and the seals data, Bently et al. (1986) evolved their work on dynamic stiffness (direct and quadrature) relating the destabilizing circumferential flows by the swirl ratio $\lambda$. Through this parameter, which relates the magnitude of the circumferential flows along with the rotor forces, phase relations were determined and criteria for self-excited vibrations established. The relations of whirl (self-excitation frequency linear with rotor speed) and whip (self-excitation frequency independent of rotor speed) in seals and bearings took shape (fig. 16). Muszynska (2001) gave a succinct summary of these results in an invited lecture at

[1]According to David Fleming of NASA Glenn, he and Gunter looked into the HPFTP instability problem and found the analysis had been carried out for a cylindrical seal. Had this seal been used rather than the labyrinth seal, sufficient damping might have been available to avoid the instability.

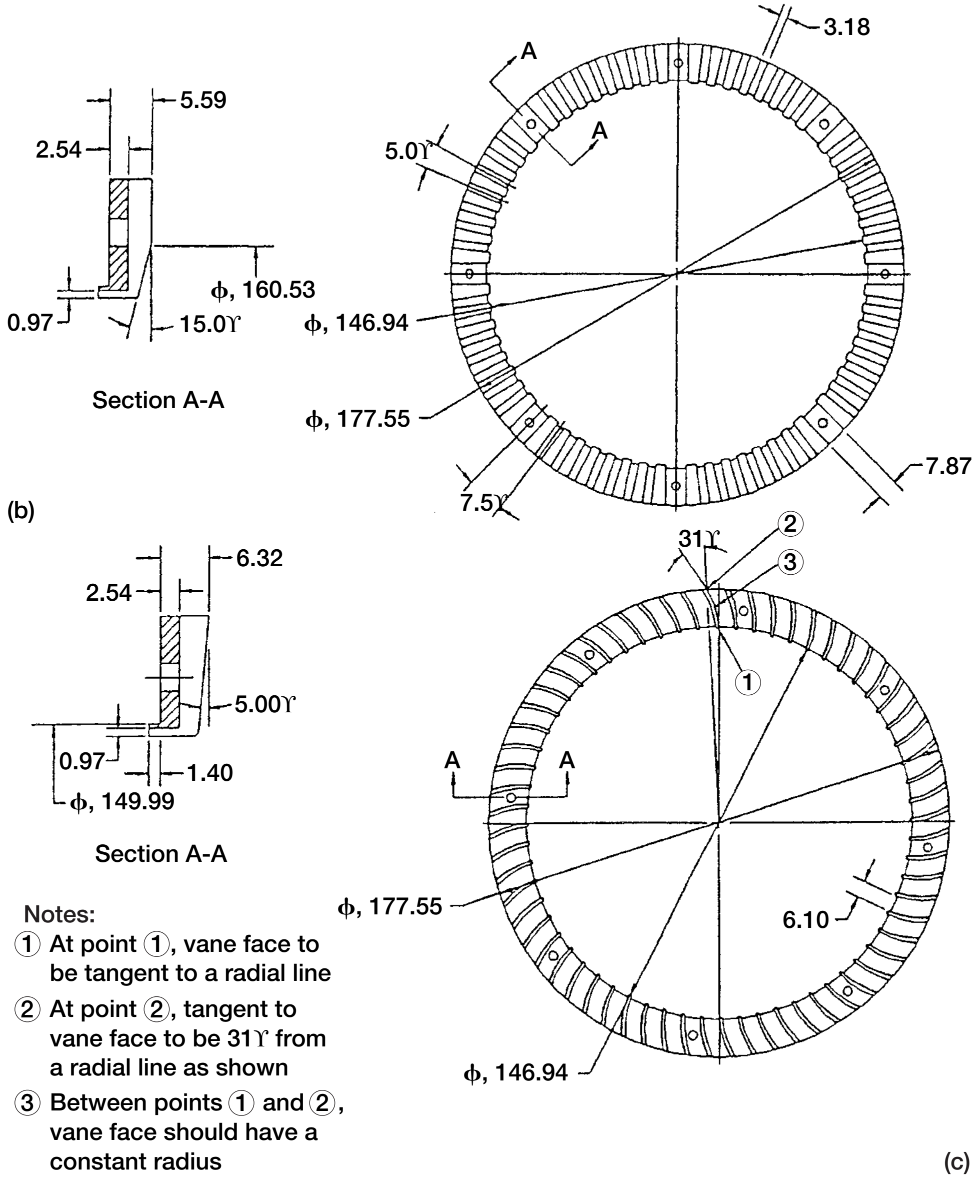


Figure 15.—Concluded. (b) Radial swirl brake. (c) Improved swirl brake. Dimensions in millimeters. (Childs et al., 1991.)

ISCORMA–1. In each case the emphasis is related to controlling the lateral or tangential forces that destabilize the rotor while maintaining those dynamic (direct) forces necessary to support turbomachine loadings (see also Bently et al., 2002).

In a recent effort Kawak et al. (2002) investigated a seal concept for an SSME-class liquid oxygen–methane pump. Held by a clamping nut and inserted between the rotor and the pump case, a floating ring seal comes into contact with the rotor at its maximum eccentricity position (fig. 17). As the pump comes up to speed, the backflow from the impeller forces the floating ring against the static ring while fluid dynamic forces position it in orbit about the shaft center. At this point, the floating ring behaves as a cylindrical seal. Their dynamic analysis shows that a floating ring could provide pump stability to 80 000 rpm whereas a rigid cylindrical seal could provide pump stability to only 40 000 rpm, the latter being unstable in the operating range of 50 000 rpm.

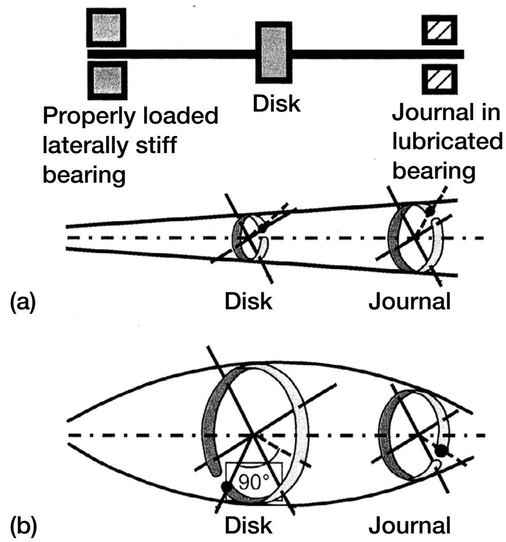


Figure 16.—Fluid whirl and fluid whip modes. (Orbits filtered to whirl or whip frequency.) (a) Whirl mode. (Disk lags journal very slightly. Shaft behaves like a rigid body.) (b) Whip mode. (Shaft deflection is similar to first balance resonance mode but is corkscrewed. Disk lags journal by up to 90°.) (Muszynska, 2001.)

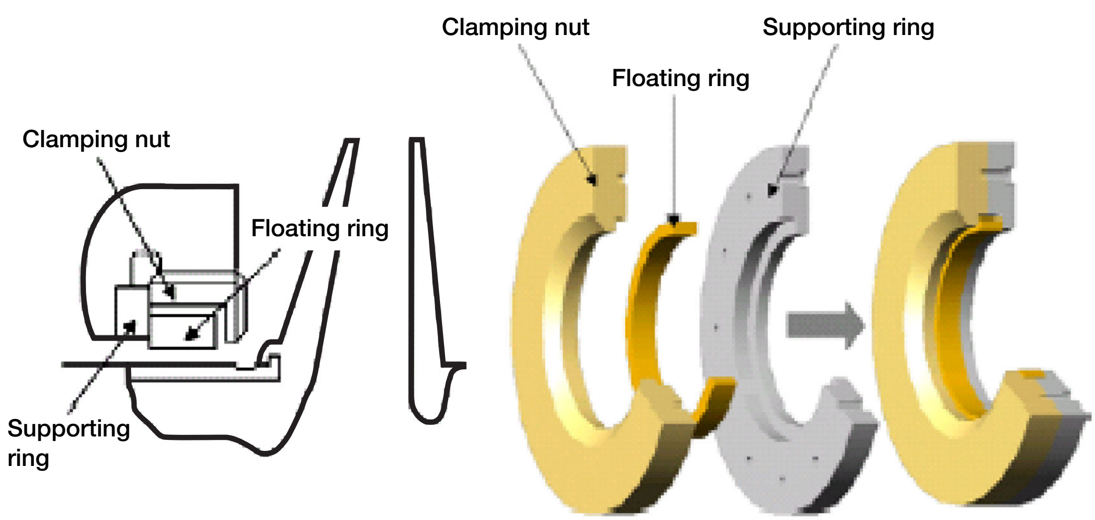


Figure 17.—SSME-class liquid oxygen–methane floating ring pump seal. (Kawak et al., 2002.)

## Aeronautical and Aeronautical-Derivative Turbomachines

Returning to the perhaps more familiar aeronautical gas turbine industry, Abbott (1981) provides a good review of aeroelastic instabilities amid sets of concerns. None of the results can be reproduced from these reviewed papers starting with Alford's work in the late 1950's and early 1960's (Alford, 1963, 1971) and all the subsequent ones. To be fair, the problems and solutions are reported but key geometric information is always missing. Each company must have its own files or know the engine parameters for those results that are held proprietarily (i.e., this is a guide; get your own test data).

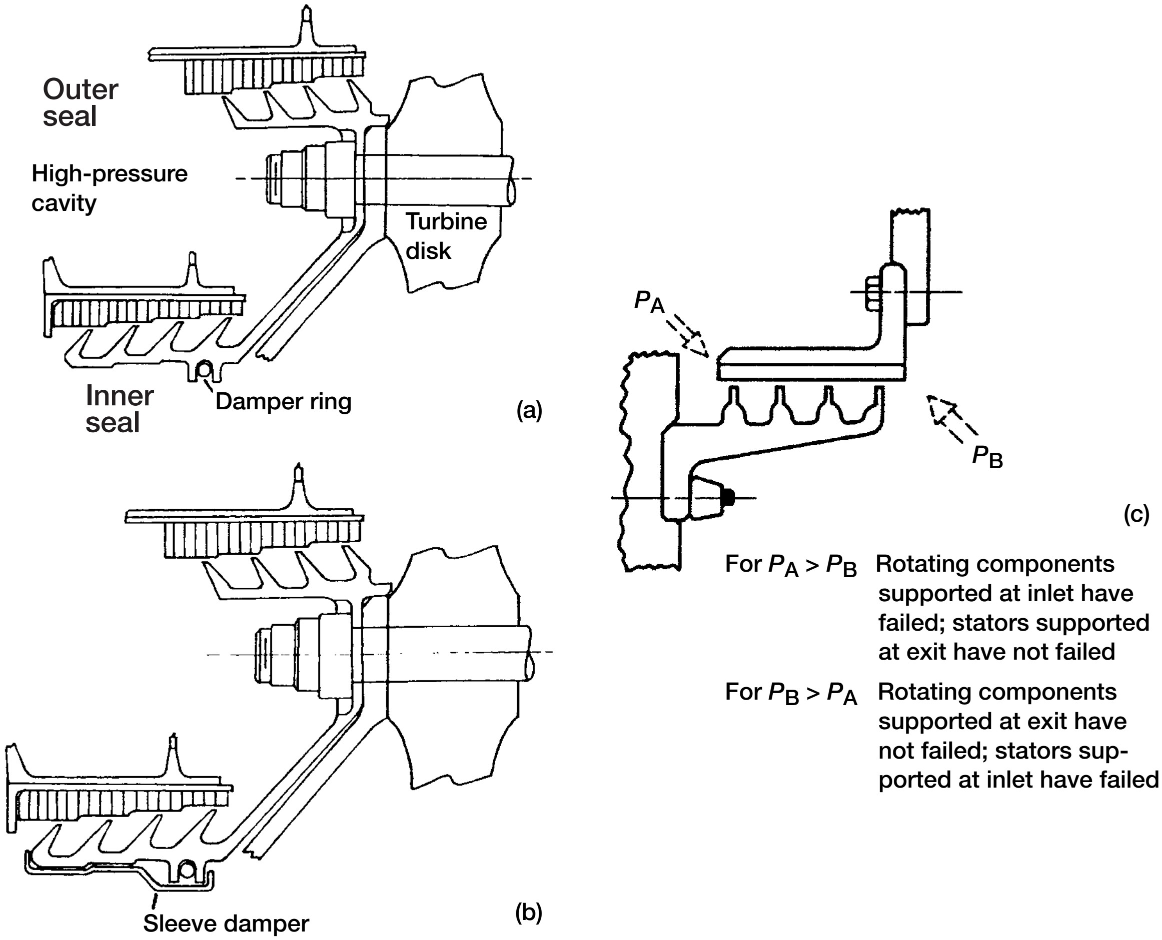


Figure 18.—Inner and outer labyrinth air seals. (a) Damper ring. (b) Damper drum (Abbott, 1981). (c) Effect of seal component support (Ludwig, 1978).

### Damper Rings and Drums

Engine companies preferring to support seals at the low-pressure side have no reported seal vibration problems with this configuration (e.g., outer seal (fig. 18)). However, supporting a seal at the high-pressure side highly stresses the “knee” or last tooth region, and instabilities have caused engine failures (e.g., inner seal (fig. 18)). Here, the classic “fix” is to add a damper ring or a cylindrical damper drum as in the case where the ring has insufficient damping. These are usually severed rings (also called split rings) or severed drums (fig. 18). Abbott’s (1981) analysis included the circumferential fluid velocity that enabled him to show that damping of a seal supported on the low-pressure side (outer seal) crosses over from apparent negative to positive damping before the mechanical system’s natural frequency reaches the fixed acoustic frequency (fig. 19(a)). On the other hand for a seal supported on the high-pressure side the damping becomes apparently negative when the mechanical system’s natural frequency exceeds the fixed acoustic frequency (fig. 19(b)). Figure 19 also gives experimental stability data for low- and high-pressure-side supports. Three different seal configurations (no details) were tested to confirm previous engine concerns, but as a safety factor they added a seal drum to the seal ring.

In his conclusions Abbott (1981) states “results are for stationary seals which are designed to have either high- or low-pressure-side support. For a rotating seal the mechanical natural frequency is the frequency which would be measured by an observer moving at the same tangential velocity as

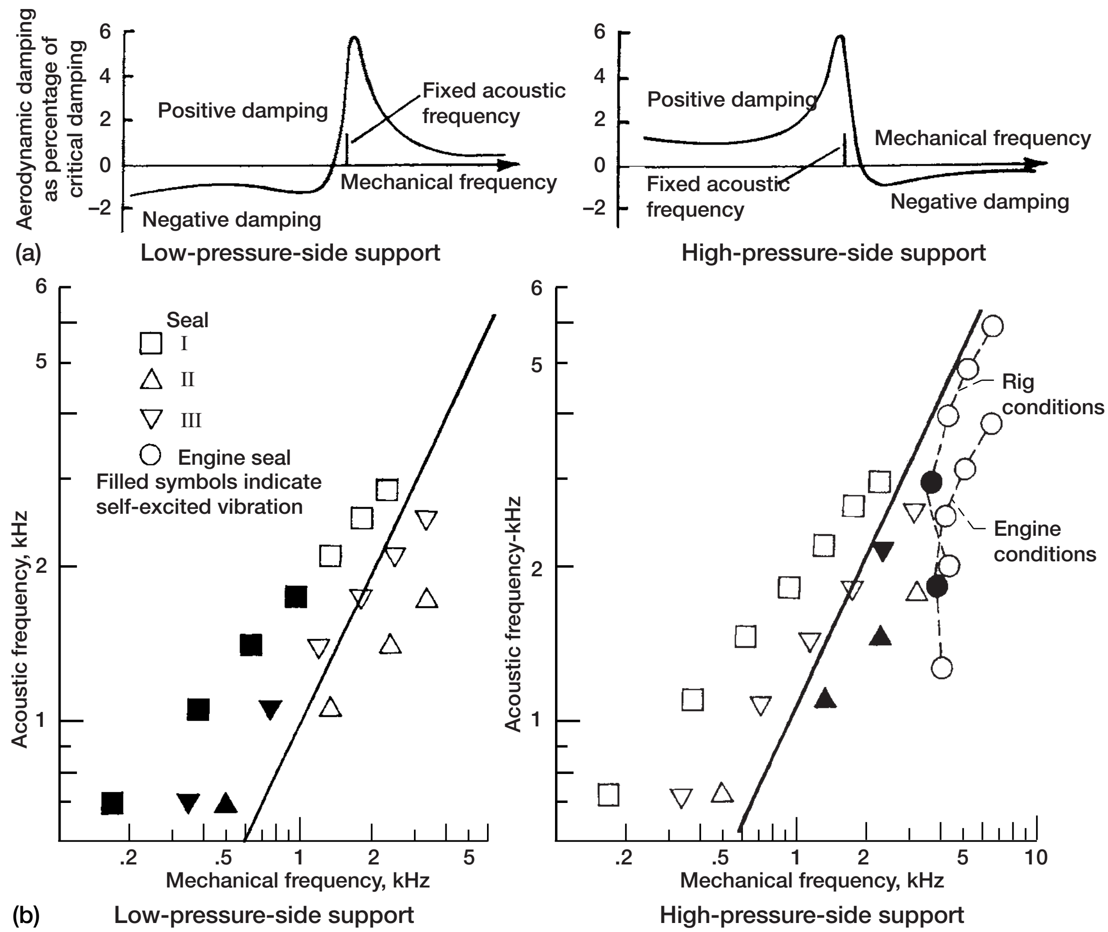


**Figure 19.—Seal support and damping characteristics. (a) Aerodynamic damping characteristics. (b) Correlation of seal support test results. (Abbott, 1981.)**

the air in the seal tooth cavities." For each mode consideration must be given to both forward and backward mechanical wave frequencies. It is clear that circumferential flows can destabilize the seal, and according to Abbott's definition of mechanical frequency it is related to the inverse of the $\lambda$-parameter of Bently et al. (1986), where $\lambda$ is the ratio of average fluid-force rotational speed to rotor speed.

***Rule of thumb***.—With reference to figure 18, if a rotating seal is supported on the high-pressure side, add dampers. If it is supported on the low-pressure side, there is generally not a problem. Make the seal stiff enough to ensure that the mechanical frequency always exceeds the acoustic frequency. For engine companies that support their seals at each end, these criteria do not hold. For example, Lewis et al. (1978) investigated high-cycle-fatigue cracking in an F–100 engine CDP seal where the rotating seal is supported at each end and the static seal is supported at the midspan (fig. 20; similar to fig. 10 in part 1). The cracking was common to seals with tight clearances. In rig testing a cavity bleed was used to perturb and excite the seal (fig. 21). Engine thrust and specific fuel consumption (SFC) were very sensitive to flow through this seal as is usually the case for the CDP seal (Hendricks et al., 1994). Stability was 13 times more sensitive to seal tooth 4 (downstream) than to seal tooth 1. Although the actual clearances are not given, the fix was to convert it into a converging seal. Opening the first tooth clearance by 0.254 mm (0.010 in.) (radial) and closing the fourth tooth clearance by 0.0381 mm (0.0015 in.) (radial) stabilized this seal configuration, but the actual clearance is not given. For a smooth cylindrical seal optimum stiffness is achieved for a clearance convergence ratio

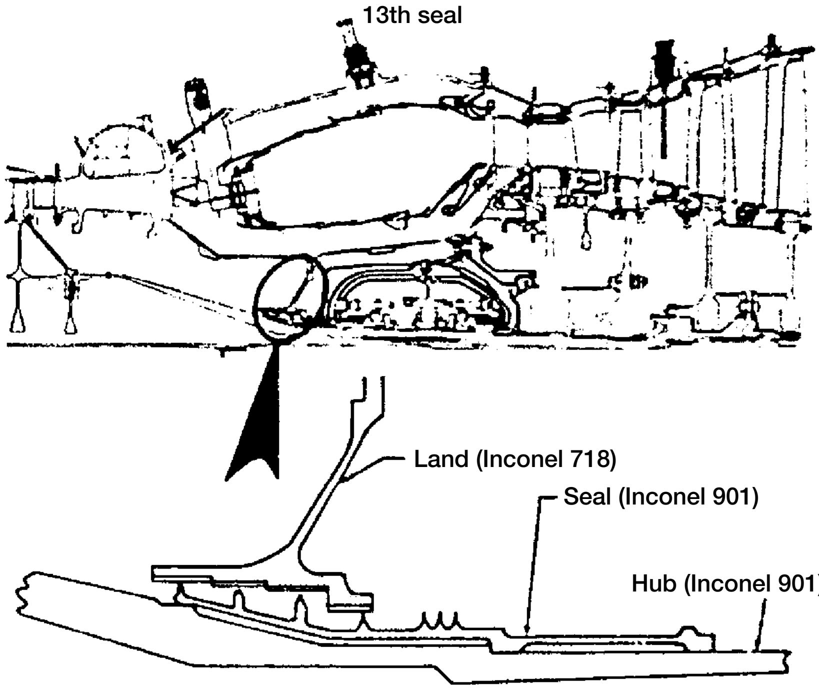


Figure 20.—Engine cross section, seal support points, and materials specifications (Lewis et al., 1978.) Seal similar to figure 10, part 1.

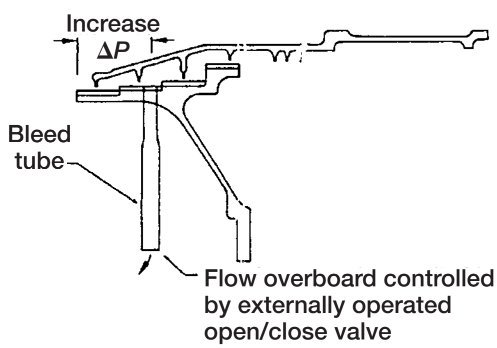


Figure 21.—Seal land bleed tube testing, amplified instability to confirm predicted pressure drop effect. (Lewis et al., 1978.)

of 1.8 (Fleming, 1977). One cannot assume labyrinth seal wear to be uniform and need to evaluate the stability of worn seals.

## Aeroelastic and Aeroacoustic Effects

Schuck and Nordmann (2002) recently investigated aeroelastic instabilities in the range 0.8 to 2.9 kHz for a nonrotating, two-teeth-on-rotor labyrinth seal. Flow through their apparatus could be in either direction, providing seal support either on the high-pressure side (HPS) or from the low-pressure side (LPS). Both the stator and the rotor cylinders were supported at the same end, a difference from the configuration of figure 16 (Abbott, 1981), making direct comparisons more difficult. For the LPS system the measured cavity pressure amplitudes diminished. For the HPS system the growth of the pressure amplitude was reproducible and higher in the cavity than in the labyrinth. In their analysis Schuck and Nordmann (2002) combined the acoustic equations with finite element methods to provide solutions for the rotor and stator frequency and mode shapes. Mode 0 happens but is not as likely. Mode 2 and mode 3 are computed with and without preswirl elements. Mode 3 (fig. 22(a)) is difficult to distinguish from mode 6 unless phase is considered. However, mode 2 is more readily distinguished (fig. 22(b)). This experimental and numerical work begins to lend further understanding to Alford's rules of thumb and brings potential resolution of the types of dampers (rings or drums) and the required geometry into the open literature.

Schuck and Nordmann (2002) investigated the stiff rotor/stiff stator combination with nominal clearance of 0.15 mm (0.006 in.). For high-pressure-side support, mode 2 vibrations appeared to be of considerable amplitudes at a pressure ratio (out/in) of 0.86, where inflow pressure was about 7 bar (102 psi). For low-pressure-side support, mode 3 was dominant with similar amplitudes, but now the pressure ratio to achieve these amplitudes dropped to 0.5 to 0.75 (toward choking conditions) and no vibration occurred at inflow pressures of 3 and 5 bar (43.5 and 72.5 psi). Mode 2 vibrations at LPS occurred only two times. The HPS and LPS mode 2 results of Schuck and Nordmann (2002, 2003) are compared in table I.

Although there are some differences in measurements, when comparing frequencies one finds that LPS is around 690 Hz and HPS is around 890 Hz. There is also a significant difference between the pressure amplitudes in the labyrinth chamber (see bold values in table), LPS being nearly half that for HPS. The difference between pressure amplitudes in the labyrinth chamber and the cavity is even larger for mode 2 than for mode 3 LPS and may be a reason why mode 3 LPS occurs much more often and why LPS vibrations need higher inflow pressure and a smaller pressure ratio than HPS vibrations.

Low-pressure-side-supported structures show less accurate coherence between the structure and the pressure field and therefore need higher pressure differences between in- and outflow to achieve comparable structural (and pressure) amplitudes. The restriction concerning the applied pressure ratio is important.

According to Schuck and Nordmann (2003) the measured data tabulated in their paper each mark an upper or lower boundary for the area of amplitude values (i.e., for a nearly constant inflow pressure, all measurements with a certain configuration show amplitude values between those two measurements).

## Compressor and Turbine Blade Tip Instabilities

Under normal operating conditions the leakage flows maximize in the leading-edge region and track across the passage to the trailing edge of the preceding blade. The stage-whirl instability is instigated (1) when a blade stalls, developing a separation region that unloads the blade and failing to produce sufficient pressure to maintain flow around it; (2) when a reduced-flow region forms ahead of the blade (blockage), diverting the flow around it and increasing the angle of attack of the oncoming blade while reducing it on the preceding blade, and (3) when the differential angles of attack cause the stall zones to propagate from the pressure side to the suction side of each blade opposite the direction of rotation in pairs or sets of stall zones that can envelop the rotor tip region (fig. 23; Johnsen and Bullock, 1965). Blade stall (airfoil flow separation) can occur for a variety of reasons, such as surface roughness on blade or casing interface, casing treatment (e.g., felt metal, honeycomb, or smooth), tip clearance, tip wear, vortex shedding, foreign object damage, nonuniform loading, and eccentric rotation).

Mailach et al. (2001) cite three types of instability originating from compressor blade tip vortices: (1) a local rotating stall region over one or a few blade passages that grows into a rotating stall cell, (2) wavelength disturbance that rotates around the annular clearance region and eventually breaks down the flow field, and (3) a group of superimposed modes or part-span stall that can

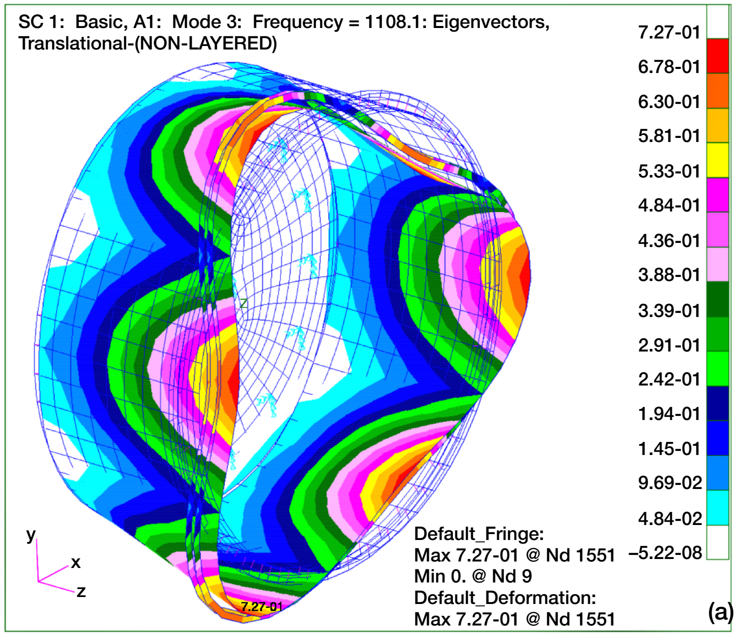


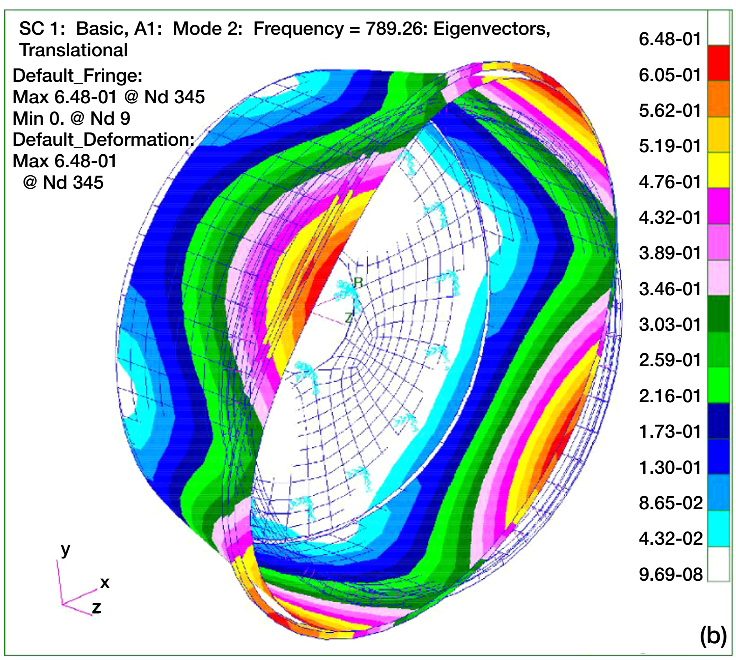


Figure 22.—Mode shape of seal housing. (a) Mode 3. (b) Mode 2. (Schuck and Nordmann, 2002.)

TABLE I.—LOW-PRESSURE- AND HIGH-PRESSURE-SIDE SUPPORT DATA WHERE MODE 2 OCCURS

| Support side | Inlet pressure, bar | Pressure ratio (out/in) | Frequency, Hz | Amplitude, μm | | Labyrinth chamber pressure, bar | Cavity pressure, bar | | |
|---|---|---|---|---|---|---|---|---|---|
| | | | | Rotor | Stator | | At labyrinth chamber | At mid-plane | Near support |
| LPS | 6.9 | 0.75 | 684 | 45 | 10 | **0.088** | 0.265 | 0.25 | 0.229 |
| LPS | 6.9 | 0.586 | 694 | 50 | 3.8 | **0.07** | 0.28 | 0.27 | 0.248 |
| HPS | 7.05 | 0.9 | 881 | 37 | 52.4 | **0.146** | 0.25 | 0.27 | 0.286 |
| HPS | 7.1 | 0.86 | 899 | 47 | 89.1 | **0.26** | 0.344 | 0.372 | 0.34 |

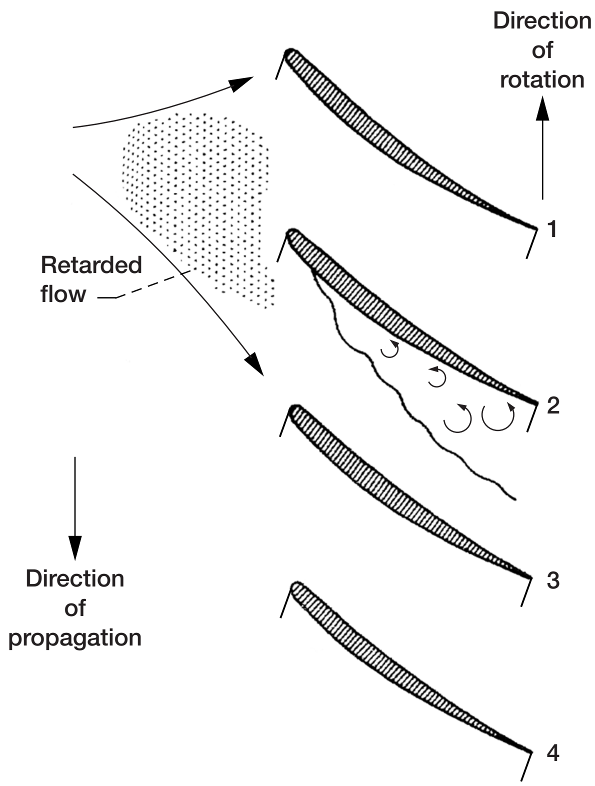


Figure 23.—Propagating stall in cascade. (Fig. 230, p. 313, Johnsen and Bullock, 1965.)

intensify tip clearance noise and blade vibrations. Although not cited, vortex flows within the blade passage are engendered by flows along the blade surfaces from the pressure to the suction side, and corner vortices may be regarded as yet another class. Under normal operating conditions the leakage flows maximize in the leading-edge region and track across the passage to the trailing edge (for more detail, see parts 1 and 3). In the experiment of Mailach et al. (2001) third-stage rotor blade data of a four-stage compressor were taken at large clearances (4.3 percent ratio of tip clearance to tip chord length). These data revealed a strong tip vortex with a reversed flow region within the gap that intensified (repeated) every other blade and subsequent blockage. Unshrouded compressor and turbine blade tip flows are illustrated in part 1 and blade passage flow computational methods in part 3. Hendricks et al. (1995) and Athavale et al. (1993) provide simulated cases.

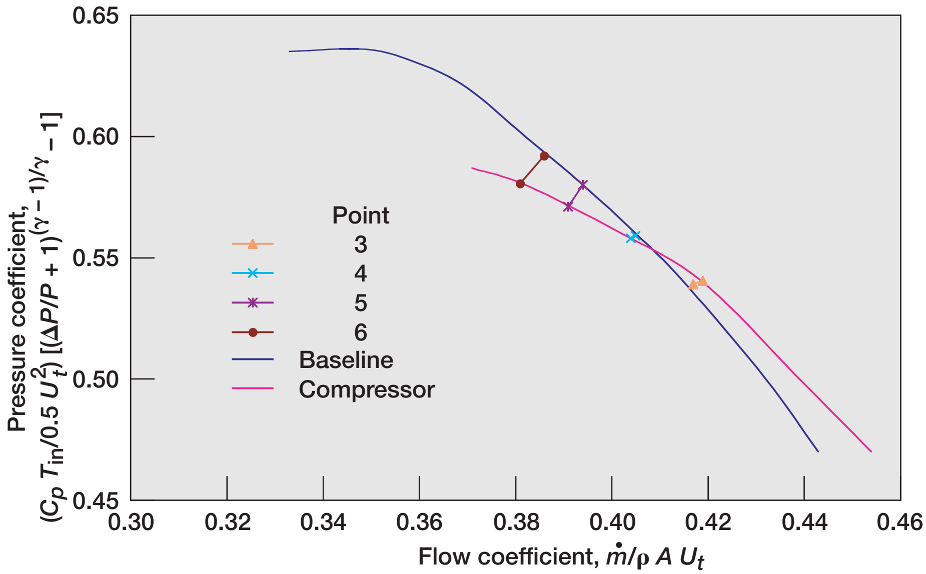


Figure 24.—Compressor map for baseline compressor and compressor A at 0.0962-cm offset and data set points 3 to 6. (Storace et al., 2001.)

TABLE II.—COMPRESSOR A FORCES AND NORMALIZED CROSS-COUPLED STIFFNESS (WHIRL ANGLE) FOR ROTOR OFFSET $Y_0$ OF 0.0965 cm (0.038 in.)

[Mean blade diameter times blade height, $D_pH$, 30.3 cm$^2$ (4.7 in.$^2$); fluid tangential stiffness coefficient, $K_{xy} = F_x/Y_0$.]

| Compressor operating condition | Test point | Radial force, $F_x$, N | Tangential force $F_y$, N | Torque, $T$, N-cm | $K_{xy}D_pH/T$ |
|---|---|---|---|---|---|
| Peak efficiency | 3 | –2.71 | 2.63 | 1010.6 | –1.64 |
| Design point | 4 | –4.13 | 4.36 | 1000.6 | –2.76 |
| High load | 5 | –7.29 | 5.69 | 989.4 | –4.63 |
| Peak pressure | 6 | –9.61 | 7.88 | 926.2 | –6.58 |

In discussing compressor whirl Storace et al. (2001) claim Alford (1965) concluded that blade loading would be lower in the minimum clearance than in the maximum clearance resulting in forward whirl, similar to turbines. Ehrich (1993) concluded the opposite. Citing the work of Thomas (1958) and Alford (1965), Storace et al. (2001) statically offset the rotor of a four-stage, low-speed, 1.524-m (60-in.), 804-rpm compressor and determined the sum of forces perpendicular to the plane of displacement. A sample map is shown as figure 24.

See table II for a representative set of data forces resulting from the integration of the pressure changes about the blade. Figure 25 illustrates these peripheral normalized pressure profiles for the high-load case ($P_{t5}$).

The resulting forces promoted backward whirl over much of the operating range with islands of zero and positive forward whirl near the design point confirming Johnsen and Bullock (1965). For the high-load case ($P_{t5}$) the magnitude of the cross-coupled force increased with offset (fig. 26). In most cases these instabilities are "fixed" by the manufacturer using split rings, drums, or enhanced dampers. However, the root cause remains unexplored and is of little consequence until the design parameters call for high stage loadings and marginal compressor designs.

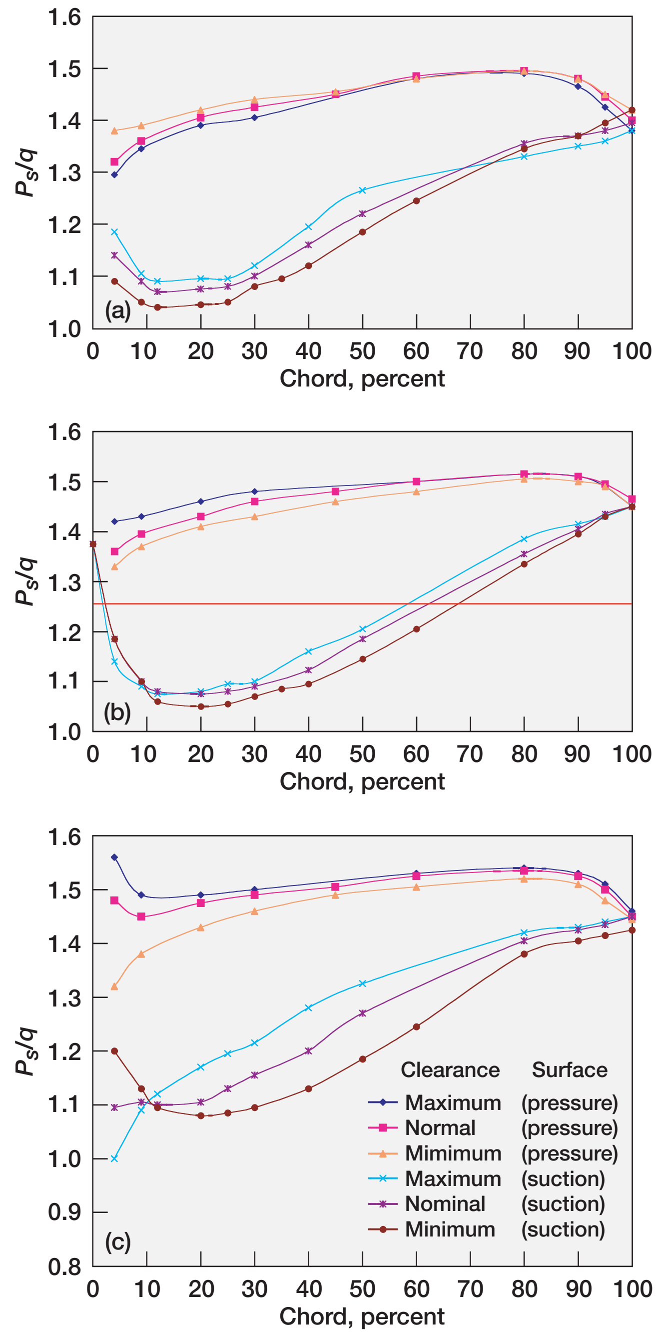


Figure 25.—Peripheral static/dynamic pressure ratio $P_S/q$ variation from leading edge to trailing edge for pressure and suction sides of stator blade. (a) At 5% span. (b) At 50% span. (c) At 90% span. (Storace et al., 2001.)

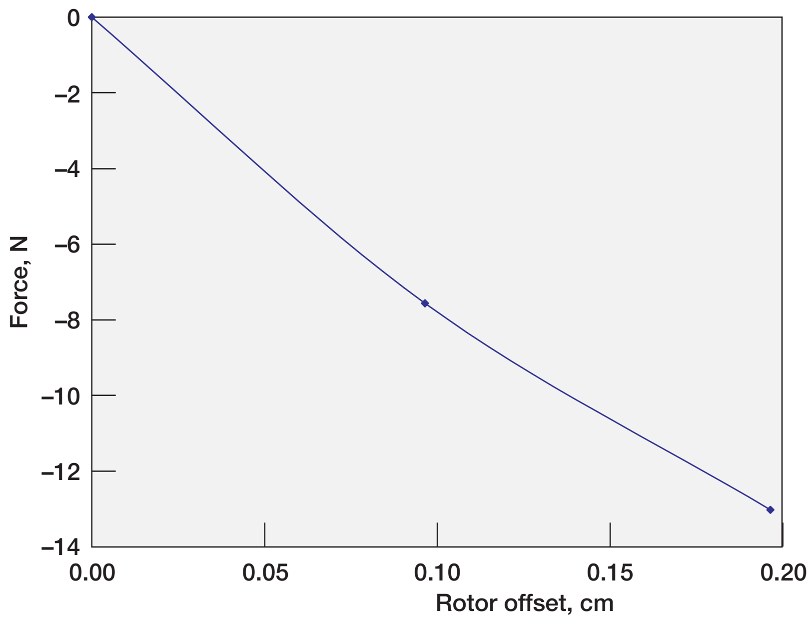


Figure 26.—Cross-coupled force at high compressor loading $P_{t_5}$. (Storace et al., 2001.)

Storace et al. (2001) also noted the peaking of the unsteady forces leading the minimum clearance by 40° for compressor A. Doubling the clearance at the rotor interface dropped torque efficiency by 1.6 points versus 0.9 point for doubling the hub stator clearance. The effects of entry cavity are explored by, for example, Millsaps in NASA CP–3239 (pp. 179–207). Storace in NASA CP–3122 (pp. 285–299) discusses predicting the performance of aerodynamically excited turbomachines, but Storace et al. (2001) does not discuss the many works appearing in the NASA Rotordynamic or Seals Workshop proceedings or in ISCORMA, which would have benefited the authors.

We will now review and expand the earlier work of Tam et al. (1988) and the lumped-parameter model of Muszynska (1986a,b) and Bently et al. (1986).

## Specifics of Tam et al. and Bently and Muszynska Models

### Computational Method of Tam et al.

Tam et al. (1988) considered a shaft rotating clockwise at rotational speed $\omega_R$, precessing with amplitude $A$, and having dynamic eccentricity at rotor precession (perturbation) frequency $\omega_P$ within a three-dimensional, static, cylindrical seal or bearing housing (fig. 27). Strong axial pressure drops, significant Coriolis and centrifugal forces, and convergent and divergent zones are the major contributors to dynamics. For these nonconventional flow fields in very narrow passages with passage geometry changing periodically with time, gyroscopic motions are predominant.

A three-dimensional, rotating coordinate frame attached to, and precessing with, the rotor at perturbation frequency $\omega_P$ can be described. In this coordinate system the given seal and bearing geometry is invariant in time (Mullen and Hendricks, 1983; Tam, 1985; and Tam et al., 1986), since the precession motion of the rotor center with respect to the housing-centered position (zero static eccentricity) is assumed to be restricted to a circular orbit. With this approach the whole computational domain is simply returning back to its quasi-steady-state condition, and the computational requirements are drastically simplified (see also fig. 28 for numerical gridding). This approach

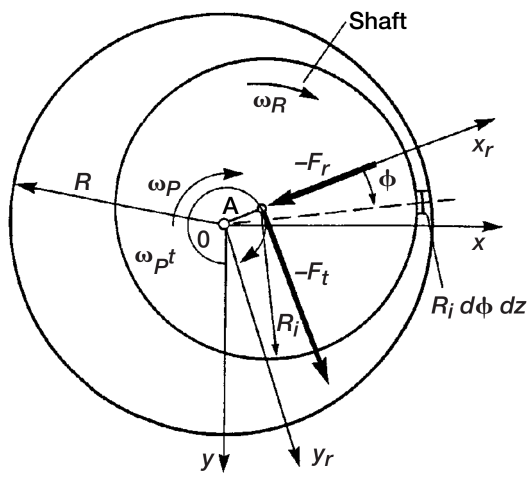


Figure 27.—Seal or bearing configuration in a constant axial plane *Z*. (Tam et al., 1988.)

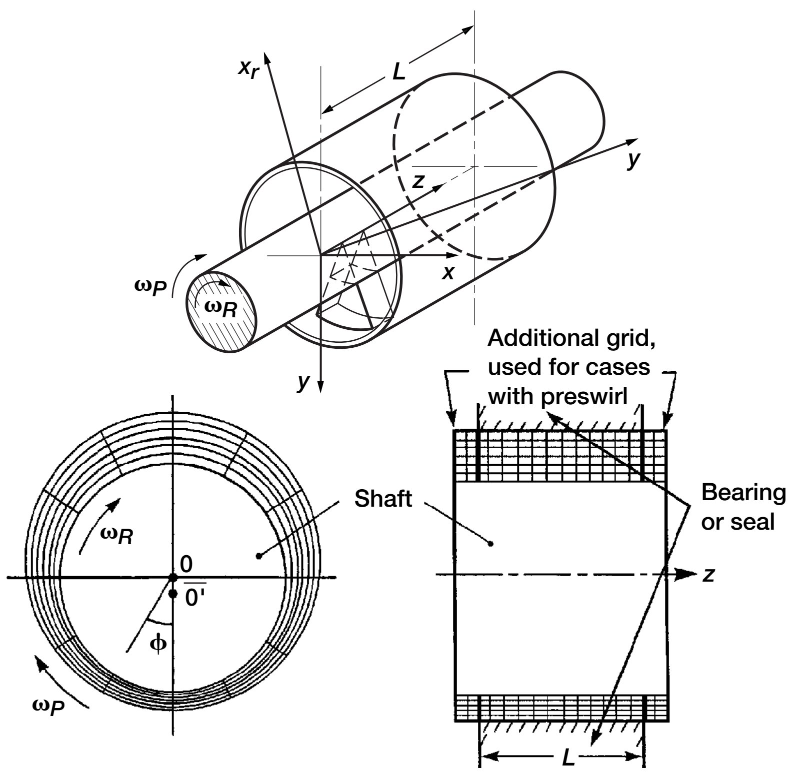


Figure 28.—Shaft housing configuration and fluid flow grid distribution. (Tam et al., 1988.)

provides a very effective and competitive advantage enabling us to perform a true two-way, solid-fluid coupling analysis with the inclusion of a solid dynamic model simultaneously interacting with the fluid flow. Part 1 of appendix A highlights the governing equations formulated, the influence of turbulence, and the numerical algorithm employed on the multidimensional modeling of whirling seals and bearings.

## Analytical Method of Bently and Muszynska (Lumped-Parameter Model)

The lumped-parameter-model fluid average circumferential velocity ratio[2] $\lambda$ (Bently et al., 1986; and Muszynska, 1986a,b) describes the fluid force more accurately than traditional analytical bearing and seal coefficient modeling. In this model the axial flow is uncoupled from the circumferential flow and affects the circumferential flow in a parametric way only. The model directly correlates to rotation-related circumferential flow parameters that are major factors in rotor stability.

The lumped-parameter analytical modeling (see part 2 of appendix A) is divided into two parts. The first part deals with the fluid film forces within the seal or bearing. The second part couples the component with the rotor to account for two complex modes. The fluid film analysis demonstrates the importance of $\lambda$ to seal and bearing stability (Muszynska, 2001). The rotor/fluid-coupled mode solution is outlined in appendix A, and to a first order the coefficients of dynamic stiffness ($K = K_D + j\,K_Q$) become

$$\begin{aligned} K_D &= \text{direct dynamic stiffness} = \text{Rotor}_{\text{DDS}} + \text{Fluid}_{\text{DDS}} \\ &= \left[K - M\omega_P\right]_{\text{rotor}} + \left[K_0 - M_f\left(\omega_P - \lambda\omega_R\right)^2\right]_{\text{fluid}} \end{aligned} \tag{5}$$

$$\begin{aligned} K_Q &= \text{quadrature dynamic stiffness} = \text{Rotor}_{\text{QDS}} + \text{Fluid}_{\text{QDS}} \\ &= \left[D_R\omega_P\right]_{\text{rotor}} + \left[D\left(\omega_P - \lambda\,\omega_R\right)\right]_{\text{fluid}} \end{aligned} \tag{6}$$

Equations (5) and (6) illustrate that system stability can be readily altered (1) by controlling swirl (von Pragenau, 1982, 1985; Muszynska et al., 1988b; and Muszynska and Bently, 1989) and (2) by increasing radial fluid film stiffness (e.g., hydrostatic and ambient pressures; Bently et al., 2002). With control of both issues, injection and pressure, rotordynamic systems can be "walked through" rotor criticals (see Bently et al., 2002) during both turbomachine runup (powered) and rundown (unpowered) (also consider throttle chops). The rundown is most dangerous because the turbomachine is unloaded.

The major effort is then to define the effects of $\lambda$, fluid film stiffness, and damping. The rotor and fluid direct (real) $K_D$ and quadrature (imaginary) $K_Q$ components follow from the nonsynchronous forward perturbation numerical results (figs. 29 and 30), which show a large fluid inertia coefficient. When the fluid film component is coupled with the system and fluid inertia is neglected, stability thresholds agree with experimental evidence.

## Modeling Results

***Computational results***.—Three-dimensional-flow numerical results show significant changes in the local values of the fluid dynamic forces along the seal (or bearing). They also show the existence of significant secondary flows and local separations even in cases of a large axial pressure drop.

[2]Fluid average circumferential velocity ratio multiplied by rotor speed $\lambda\omega_R$ is the speed at which the fluid force rotates, where $\lambda$ can be identified as the ratio of the self-excited fluid whirl frequency to the rotational speed. By using hammer impulse testing of the rotor at constant speed, $\lambda\omega_R$ can also be identified as a natural frequency of the rotor and fluid system. In many cases the value of $\lambda$ is near 1/2, but it can be greater or less than that depending on several factors (e.g., pressure gradient or viscous or injection effects).

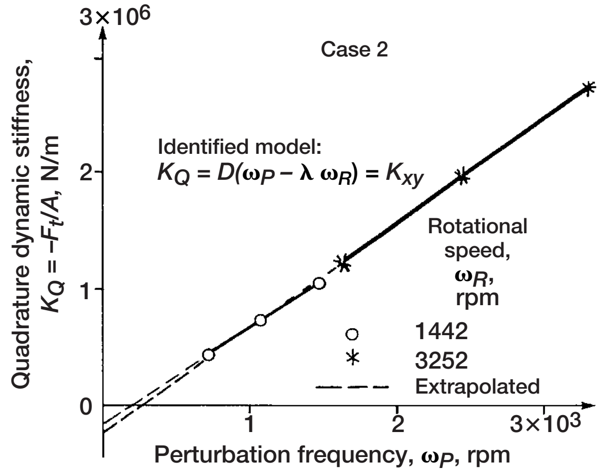


Figure 29.—Quadrature dynamic stiffness versus perturbation frequency. Identification of fluid radial damping $D$ (8860 kg/s) as slope and velocity ratio $\lambda$ (0.125) from the ordinate-intercept ($-D\lambda\ \omega_R$) of the straight line. Amplitude of rotor precession, $A = c/2$; change in fluid pressure, $\Delta_P$, 17 bars. (Tam et al., 1988.)

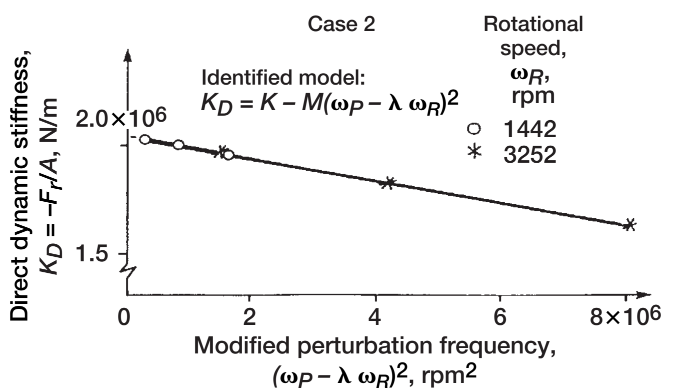


Figure 30.—Direct dynamic stiffness as function of modified perturbation frequency. In these coordinates the results represent a straight line for easy identification of fluid radial stiffness $K$ (intercept, $2.04\times10^6$ N/m) and fluid inertia $M$ (slope, 4.63 kg). Fluid average circumferential velocity ratio, $\lambda$, 0.125; amplitude of rotor precession, $A = c/2$; change in fluid pressure, $\Delta_P$, 17 bars. (Tam et al., 1988.)

The integrally averaged forms of fluid direct $K_D$ and quadrature $K_Q$ dynamic stiffnesses arise from fluid radial $F_r$ and tangential $F_t$ force components divided by precession amplitude $A$. The dynamic stiffnesses are plotted versus perturbation frequency $\omega_P$ (fig. 29) and in its modified form (fig. 30), where only forward perturbation was considered ($\omega_P$ and $\omega_R$ in the same direction). (See also part 1 of appendix A.)

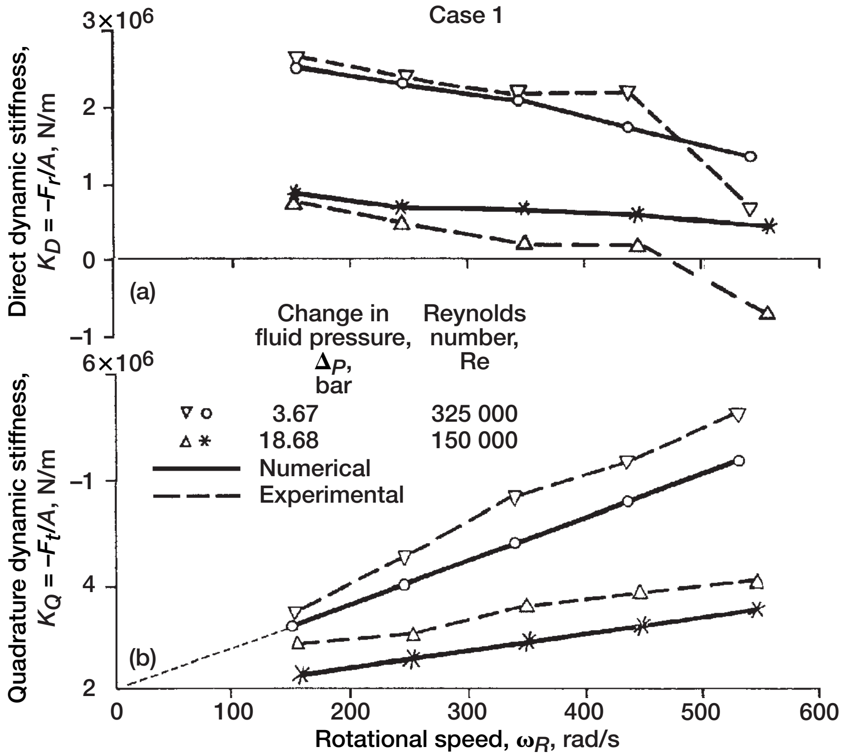


**Figure 31.—Fluid (a) direct and (b) quadrature dynamic stiffnesses as function of rotational speed for two axial Reynolds numbers. Amplitude of rotor precession, $A = 0.24c$. A comparison of calculations and measurements by Childs in NASA CP–2238 and contract NAS8–33716. (Tam et al., 1988.)**

***Comparison with experimental data***.—Figures 31(a) and (b) compare numerical results[3] with the experimental results obtained by Childs (in NASA CP–2250, 1982, and in NASA CP–2338, 1984). Although there were three steps within the length of the experimental seal, for simplicity the seal modeled was considered as a straight cylindrical seal without inlet preswirl. The experiment and the calculations qualitatively agreed. The calculated direct dynamic stiffness decreased with speed but did not exhibit the negative values of the experimental data at elevated rotor speed. The omission of the internal steps may account for this discrepancy. The quadrature dynamic stiffness increased with rotational speed and agreed reasonably well with the data of Childs.

***Nonlinear considerations***.—For amplitude $A = 0.5c$ (where $c$ is bearing or seal radial clearance), the dynamic stiffnesses are higher than for $A = 0.24c$. The fluid radial stiffness $K$ is a nonlinear increasing function of shaft eccentricity (the most pronounced effect), and pressure and fluid average circumferential velocity ratio $\lambda$ is a decreasing function of eccentricity (lesser effect). The effect of eccentricity on the fluid radial damping $D$ and the fluid inertia in the range of parameters considered is not very high.

***Seal secondary flow***.—Lower rotational speed and higher perturbation speed intensified the secondary flow zones and, by lowering the average circumferential velocity, enhanced rotor stability. The zone of secondary flow depends on the inlet boundary conditions and rotates with rotor precession frequency $\omega_p$.

[3]Modeling fluid, bromotrifluoromethane, or Halon 1301 ($CBrF_3$), used for fire suppression.

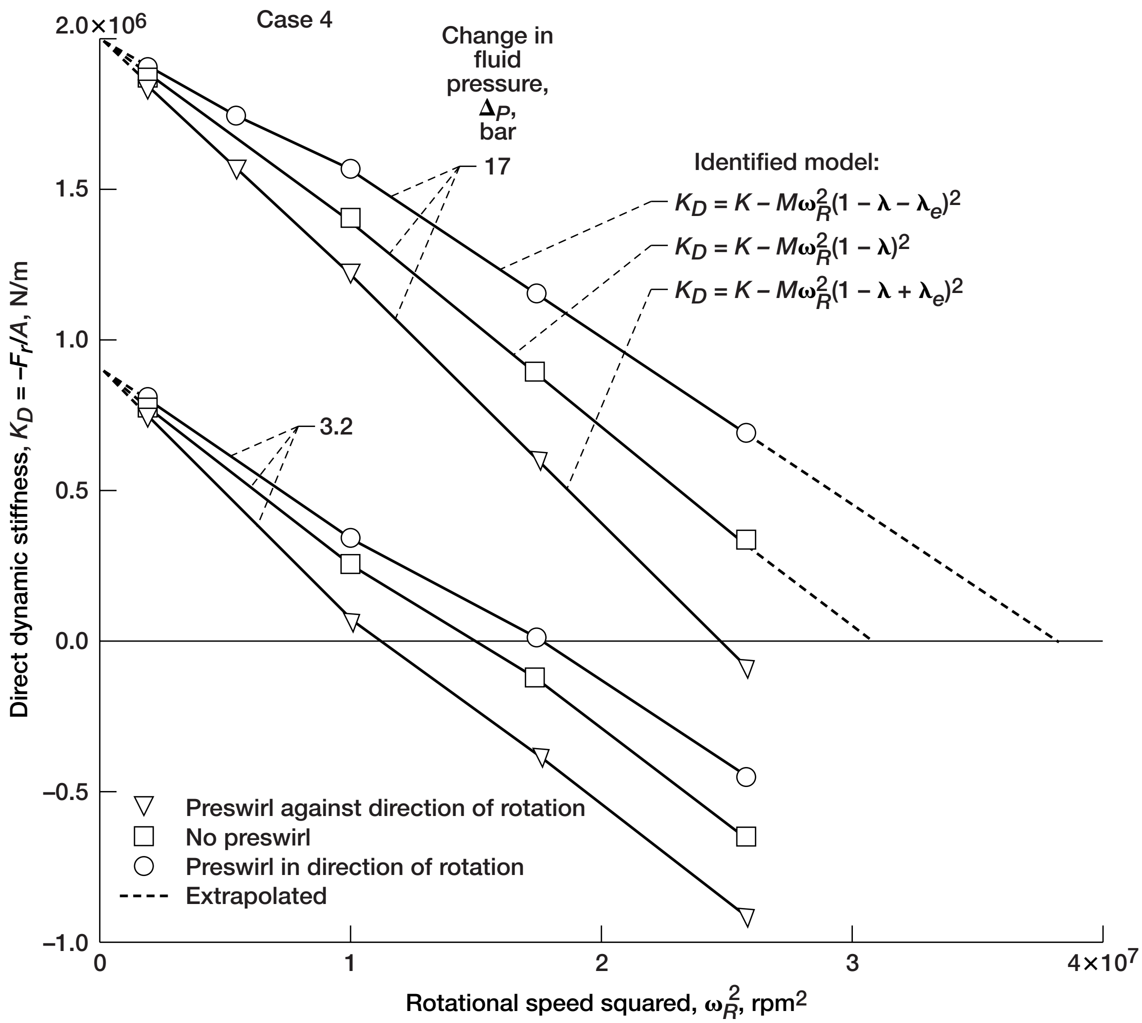


**Figure 32.—Direct dynamic stiffness as function of rotational speed squared (synchronous perturbation). $M(1-\lambda)^2$ = 0.0648 kg; fluid radial stiffness coeffecient, $K$, 1.98×10$^6$ N/m; pressure-related circumferential average velocity ratio, $\lambda_e$) = 0.111 (1 – λ); amplitude of rotor precession, $A$ = 0.24$c$. Note influence of preswirl on average circumferential velocity ratio as well as increase of fluid radial stiffness with pressure differential. (Tam et al., 1988.)**

In the numerical model the preswirl was imposed at the seal inlet in either the forward or backward circumferential direction in the following form:

$$V_{\mathrm{ps}} = R_i \omega_R \left[1 - r/R\right]^{1/3} \tag{7}$$

where $V_{\mathrm{ps}}$ is the preswirl circumferential velocity at radius $r$ and $R_i$ and $R$ are shaft and seal radii, respectively. Figures 32 and 33 show calculations for seal flow with preswirl at two values of axial pressure drop. The preswirl clearly modified λ, here shown for synchronous perturbation ($\omega_P = \omega_R$). For higher axial pressure drops the circumferential flow is reduced as shown schematically in figure 34.

Figure 35 illustrates the influence of inlet preswirl on the secondary (backward) circumferential flow field. It is evident that the preswirl intensified the recirculation zone if it was introduced in the direction opposite to rotation (lower resultant λ and higher rotor stability). Preswirl in the direction

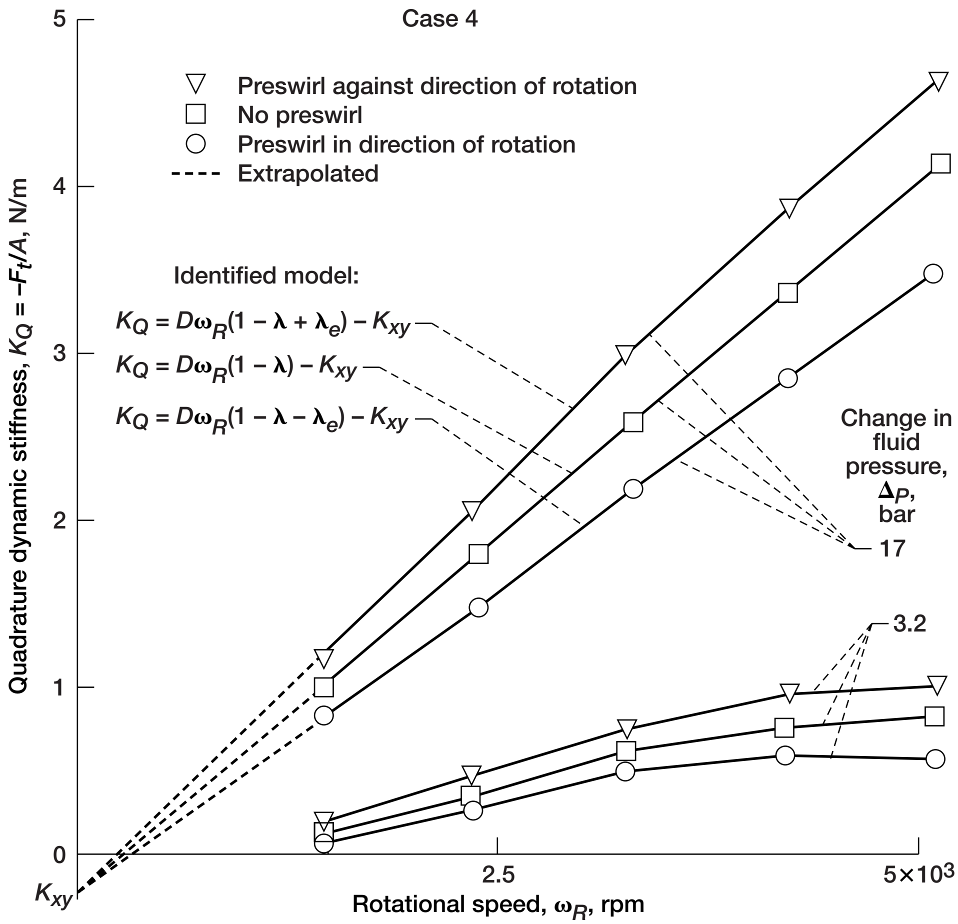


Figure 33.—Quadrature dynamic stiffness as function of rotational speed (synchronous perturbation). Fluid effective damping, $D(1-\lambda)$ = 8240 kg/s; pressure-related circumferential average velocity ratio, $\lambda_e$, 0.141 $(1-\lambda)$; fluid tangential stiffness coefficient, $K_{xy}$, $2.58\times10^5$ N/m; amplitude of rotor precession, $A = 0.24c$. Note influence of preswirl on average circumferential velocity ratio as well as increase of fluid radial stiffness with pressure differential. (Tam et al., 1988.)

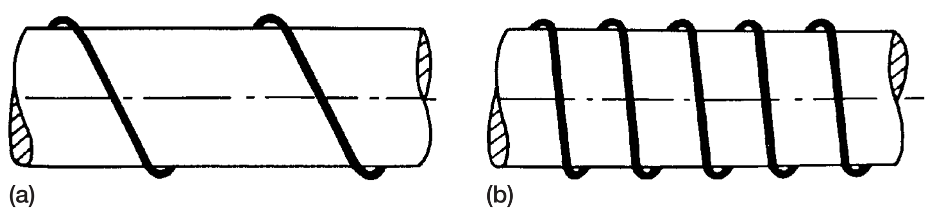


Figure 34.—Interpretation of axial and circumferential flow resulting in "spiral" flow. (a) High pressure drop. (b) Low pressure drop. (Tam et al., 1988.)

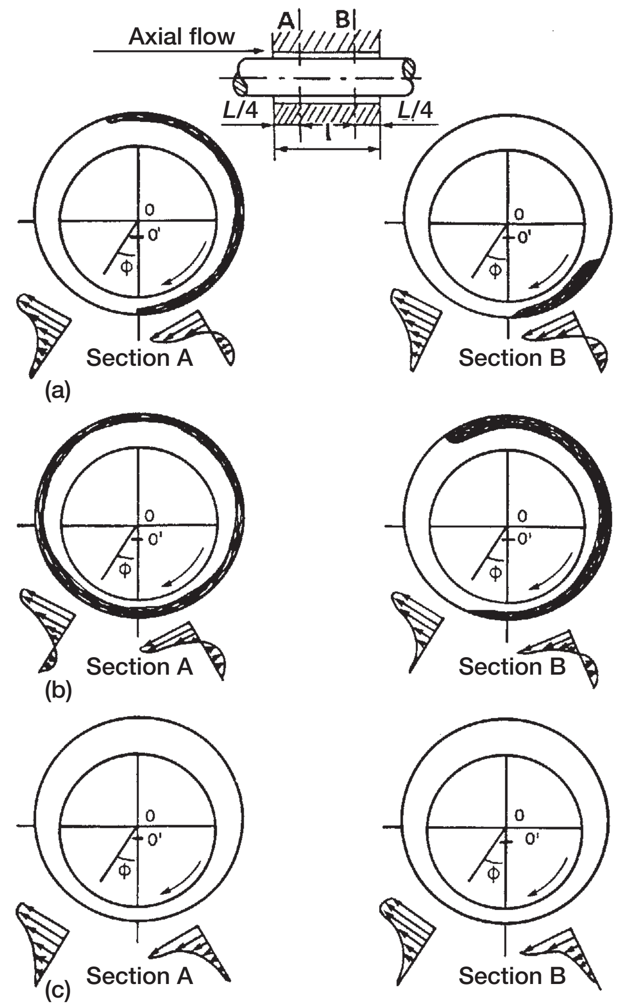

Figure 35.—Influence of preswirl on circumferential flow field. (a) No preswirl. (b) Preswirl against direction of rotation. (c) Preswirl in direction of rotation. Shadowed areas indicate secondary flows. (Tam et al., 1988.)

of rotation weakened the recirculation zone and intensified forward circumferential flow (higher resultant $\lambda$).

***Effects of surface curvature and influence of rotating flows on turbulence***.—As cited in part 1 of appendix A, in the regions of negative velocity gradients the Richardson flux is also negative and a smaller value of $\varepsilon$ decay intensifies the turbulence level. Negative Richardson flux increases from the shaft walls (from inner to outer walls) and becomes a maximum at the separation regions. Then, the gradient of Richardson flux drops sharply and changes to a positive number where the turbulence level is damped and a secondary recirculating zone appears.

In the case of forced swirl, formed by a spinning shaft, the centrifugal forces near the inner wall support the growth of vortical structures more than in curved-channel flow. The angular velocity gradients are generally negative all across the flow path, with the largest absolute values near the housing, where the largest turbulence will be generated. This situation is inherently unstable because high turbulence levels suppress the formation of secondary flow patterns. However, by introducing preswirl or multiple injection on the seal or bearing, often a counterswirling vortex can be formed near the housing wall, which is known in practice to have a stabilizing effect on rotordynamics. In this case the largest angular velocity gradient is shifted toward the shaft. Within the countervortex

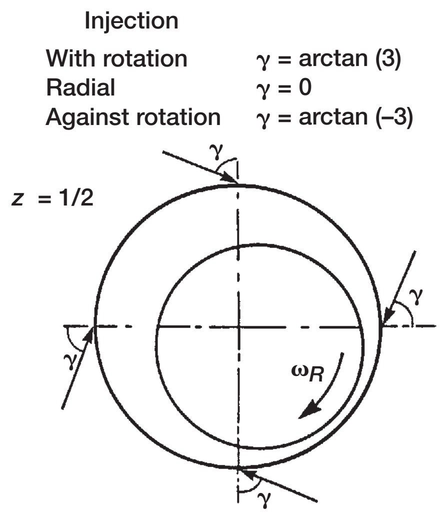


Figure 36.—Injection geometry. (Tam et al., 1988.)

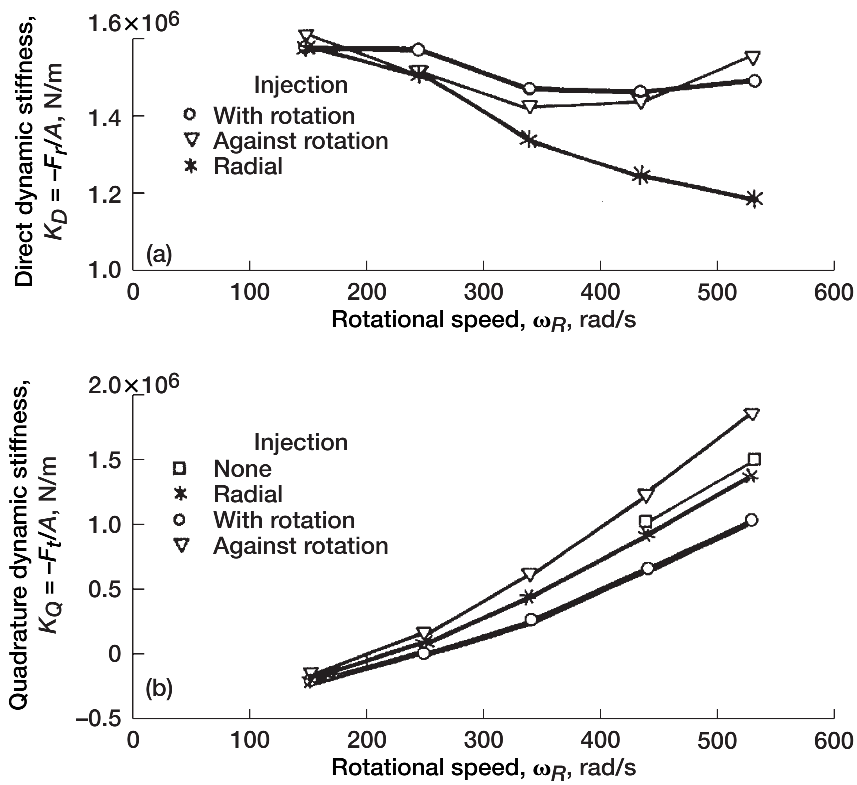


Figure 37.—Direct (a) and quadrature (b) dynamic stiffnesses as function of rotational speed for cases with fluid injection (synchronous perturbation). Change in fluid pressure, $\Delta_P$, 0.5 bar. (Tam et al., 1988.)

zone both the Richardson flux and the gradient of angular velocity change sign, in turn reducing the turbulence levels in that region and enhancing system stability.

***Fluid injection effects***.—Figures 36 and 37 illustrate the injection geometry and the influence of fluid injection on dynamic stiffness and give the corresponding angular relations. Three cases with injection were considered (radial or "vertical", in the direction of rotation, and against rotation). Injection rate was proportional to rotational speed. All parameters exhibited nonlinear character as functions of rotational speed. Fluid radial stiffness increased, fluid inertia decreased, and fluid effective damping $D(1-\lambda+\lambda_i)$ increased when injection was against rotation ($\lambda_i < 0$, where $\lambda_i$ is the injection-related average circumferential velocity ratio) and decreased when injection was in the direction of rotation ($\lambda_i > 0$). Radial injection caused a higher radial stiffness $K$ and a lower $\lambda$ than in the no-injection case, a very important observation for pressurized, fluid-lubricated bearings as well as for antiswirl seal techniques. The average axial leakage was reduced by 7 percent. (See also part 2 of appendix A.)

In developing the LE–7A liquid hydrogen–liquid oxygen engine for the H–IIA launch vehicle, subsynchronous whirl at 250 Hz (rotations/s) (15 000 rpm; 1571 rad/s) was found in the fuel turbopump. The instability could be controlled by tightening the bearing clearances, but that solution proved too costly. A CFD analysis was undertaken to assess the effect of Thomas forces (Alford forces) (fig. 38). The computational sector model included the power-stream flow path through the nozzle and one turbine stage of the high-pressure fuel turbopump (inlet pressure, 21.4 MPa at 750 K) rotating at 703 Hz (rotations/s) (42 200 rpm; 4419 rad/s) and developing 28 800 kW of power at design conditions. Figures 39 and 40 give streamlines and pressure distributions at three normalized tip clearances (0.5, 1.0, 1.5). With these results rotor torque can be evaluated. Seal swirl or fluid-force circumferential velocity $\lambda$ causes the rotor system to become unstable. Reversing inlet swirl stabilizes the system as also noted by Thomas (1958), Benckert and Wachter (1978), and Tam et al. (1988). Altering the injection of liquid hydrogen coolant flows (seal leakage) at the seal inlet from normal to the rotor to tangential to the rotor mitigated the instability (figs. 41 and 42).

In terms of Thomas forces as described by Motoi et al. (2003), the destabilizing force $F_t$ illustrated in figures 27 and 38 becomes

$$\begin{aligned} F_t &= \sum \frac{T_0}{R}\left[1+\frac{T_1-T_0}{T_0}\cos\theta\right] \qquad && 0 \le \theta \le 2\pi \\ &= \frac{\alpha T_{\text{total}}}{2R} && \alpha = \frac{T_1-T_0}{T_0} \end{aligned} \tag{8}$$

where $T_1$ is the torque at maximum tip clearance, $T_0$ the torque at average tip clearance, and $T_{\text{total}}$ the total torque of all turbine blades.

$$K_{xy} = F_t/\varepsilon \tag{9}$$

where $\varepsilon$ is the ratio of eccentricity $e$ to clearance $c$. As suggested by Thomas (1958)

$$K_{xy} = \beta T_{\text{total}}/DL \tag{10}$$

where $L$ is the blade length, $D$ the turbine diameter, and

$$\beta = \alpha/(2\varepsilon R F_t) \tag{11}$$

was evaluated though computation and agreed with experimental data. For the turbopump configuration of Motoi et al. (2003) $K_{xy} = 8.1\times10^5$ N/m and $\beta = 0.56$.

The computational effort represents a more realistic approach by including nozzle and blade flows at three eccentric geometric conditions. For these rotor and stator computations, only steady solutions were considered, and "boundary data were averaged" and then passed off to the other subdomain at this boundary. The unsteady flow field can be computed but requires very large computational times, mesh sliding, and time resolution. Although the model is simplified with respect

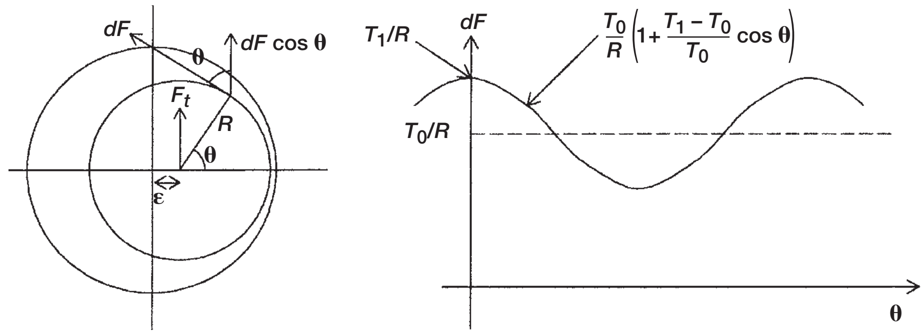


Figure 38.—Thomas force. (Motoi et al., 2003.) Courtesy ISCORMA–2.

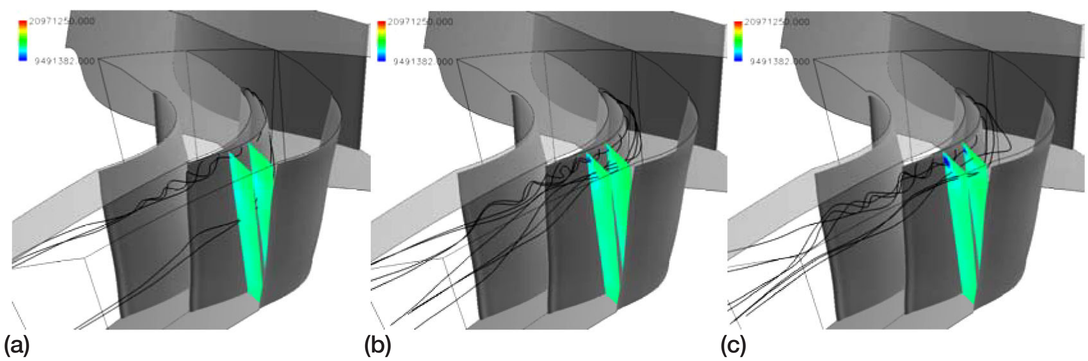


Figure 39.—Streamlines and pressure distributions. (a) Tip clearance, 0.5. (b) Tip clearance, 1.0. (c) Tip clearance, 1.5. (Motoi et al., 2003.) Courtesy ISCORMA–2.

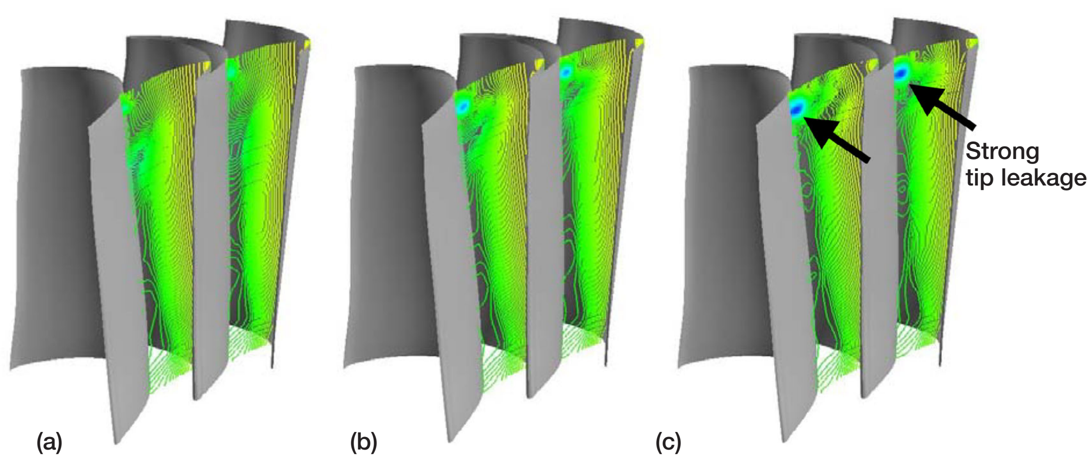


Figure 40.—Effect of tip clearance on pressure distribution. (a) Tip clearance, 0.5. (b) Tip clearance, 1.0. (c) Tip clearance, 1.5. (Motoi et al., 2003.) Courtesy ISCORMA–2.

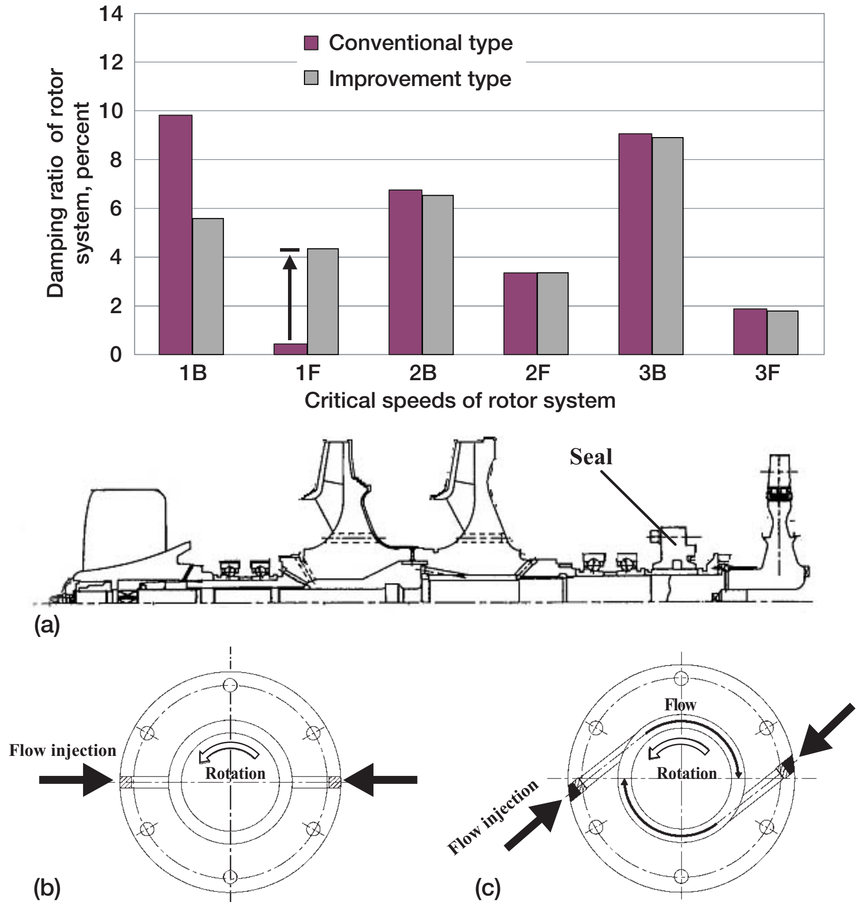


Figure 41.—Damping ratio of each mode. (a) Turbine seal (cross section of fuel turbopump). (b) Conventional type. (c) Improvement type. (Motoi et al., 2003.) Courtesy ISCORMA–2.

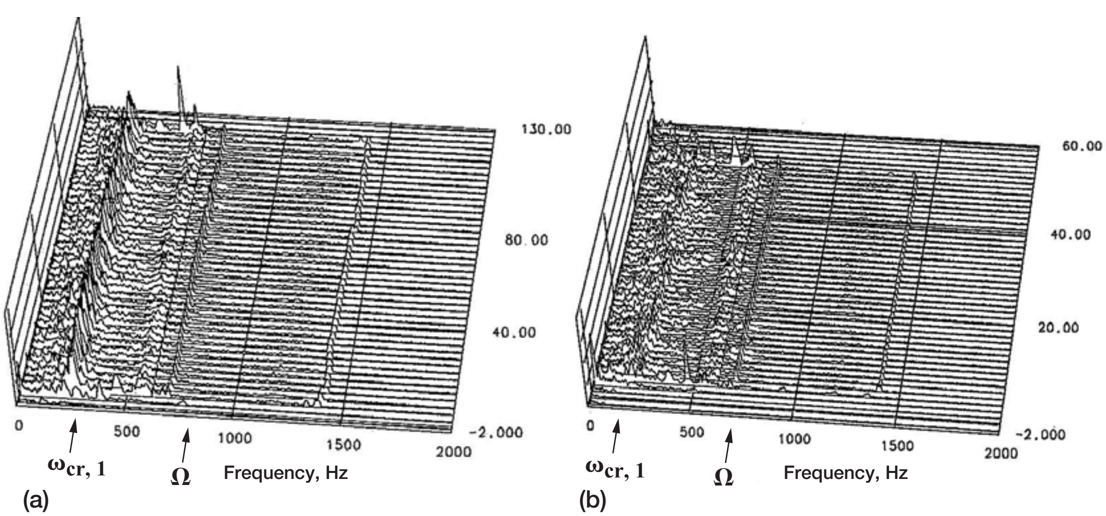


Figure 42.—Displacement in radial direction of fuel turbopump at engine firing tests. (a) Conventional seal. (b) Improved seal. (Motoi et al., 2003.) Courtesy ISCORMA–2.

to nozzle and blade time-dependent interactions and dynamic flow interactions between the casing and the rotor blade tip, Motoi et al. (2003) cite good agreement with data. Further, using these computational results as guidelines—instead of changing the turbine design to reduce the Thomas (Alford) forces and correcting the inlet swirl, which is known to stabilize seals (e.g., labyrinth seals)—provided the required turbopump stability.

As another example of the effects of preswirl and injection, Kanki et al. (2003) investigated partial-admission turbine sealing. Gas turbine and steam turbine combined-cycle operation provides higher plant efficiencies at greatly reduced carbon dioxide, $NO_x$, and other emissions than conventional systems. Partial-admission turbines are used to control load demand and therefore engender complex effects that often lead to subsynchronous vibrations. Under these conditions inlet swirl produces similar destabilizing effects in both cylindrical and labyrinth seals. Because the destabilizing force in partial-admission turbines depends strongly on swirl distribution, adding a swirl break (fig. 43) had a large effect on both full- and partial-admission turbines. Figure 44 gives natural frequency and damping ratio data for labyrinth and flat annular (smooth) seals and shows peak values for the smooth seal nearly twice those for the labyrinth seal with no swirl break inserts.

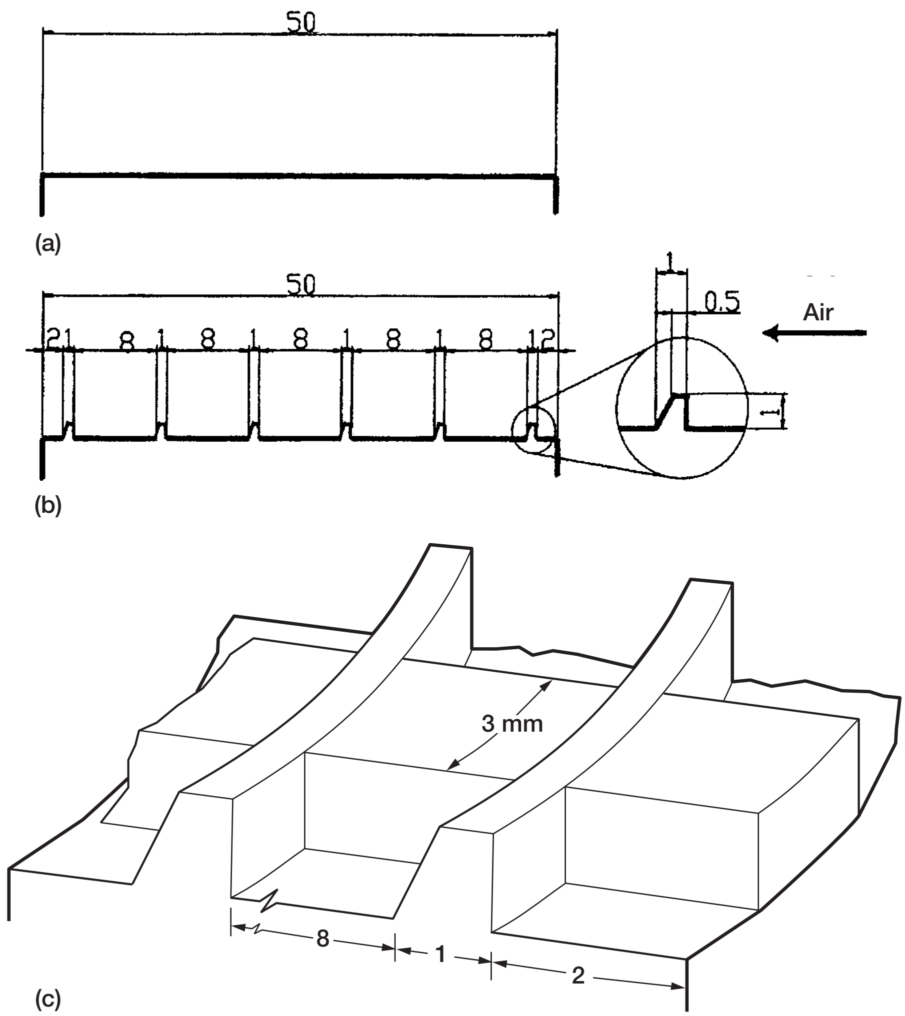


Figure 43.—Configuration of test seal. (a) Annular seal. (b) Labyrinth seal. (c) Flow blockers. Dimensions in millimeters. (Kanki et al., 2003.) Courtesy ISCORMA–2.

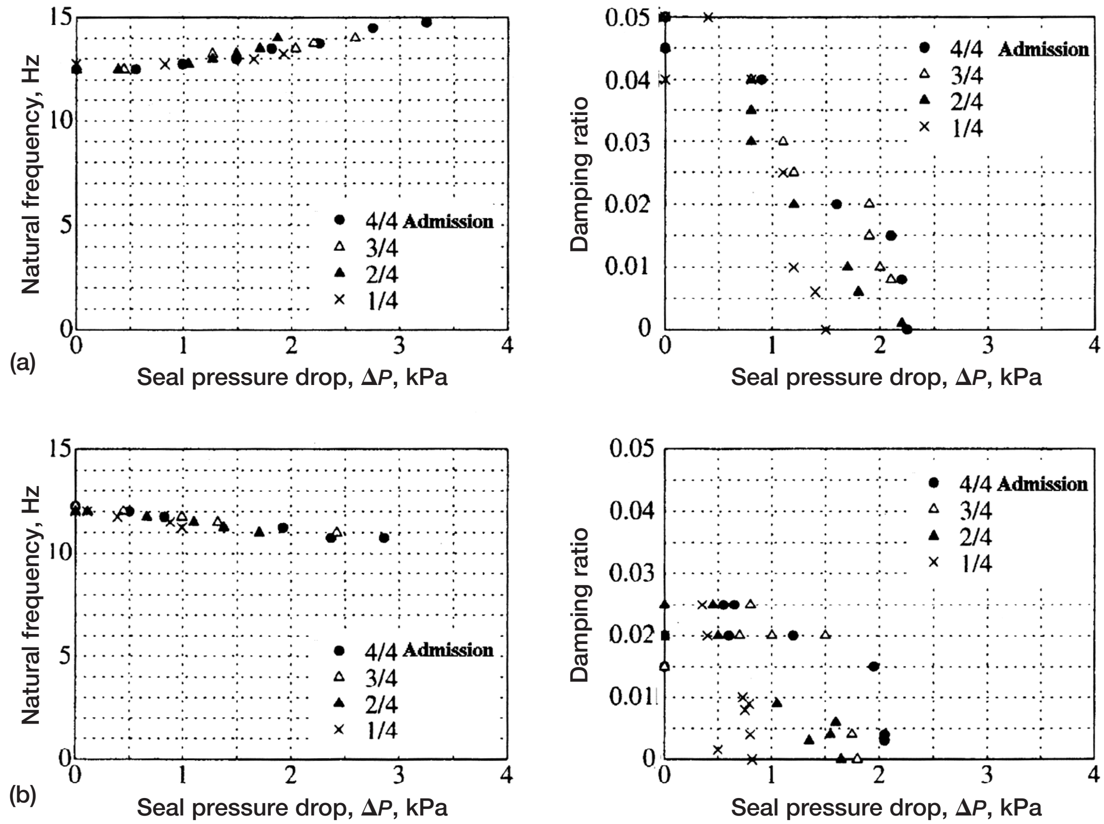


Figure 44.—Comparison of flat annular (smooth) seal and labyrinth seal. (a) Smooth seal. (b) Labyrinth seal. (Kanki et al., 2003.) Courtesy ISCORMA–2.

For comparison, figure 45 shows cases with inlet swirl breakers only and with multiple-chamber swirl breakers (three labyrinth chambers and inlet).

Figure 46(a) gives average swirl velocities and pressure drop data for four 90° flow blockage sector configurations (e.g., four of four sectors open (two transducers per sector; i.e., a full-admission condition)), and figure 46(b) gives data for three of four sectors blocked (i.e., a one-quarter-admission turbine). Data are also given for three of four and two of four sectors blocked.

***Conditions and parameters of Kanki et al. (2003).***—Kanki et al. (2003) studied six-tooth labyrinth and smooth seals under the following conditions: experimental seal length (50 mm), diameter (129.5 mm), radial clearance (0.25 mm), casing surface (smooth), support shaft diameter (5 mm), support span length (300 mm), casing thickness (10 mm), inlet air pressure (0.4 MPa), outlet pressure (atmospheric), maximum flow rate (2.5 N-m$^3$/min or standard m$^3$/min), and rotational speed (zero). The preswirler was a set of 45° helical gears with a standard 2-mm involute profile. The labyrinth tooth was 1 mm at the casing wall by 1 mm high and had a 0.5-mm forward facing (surface) at the rotor interface. The cavity length was 8 mm with 2-mm inlet and exit lengths. The flow blocks were rubber inserts 1 by 3 by 8 mm for the labyrinth chamber or 1 by 3 by 2 mm for the inlet. Blocks were inserted around the circumference to block circumferential flow in either one, three, or five

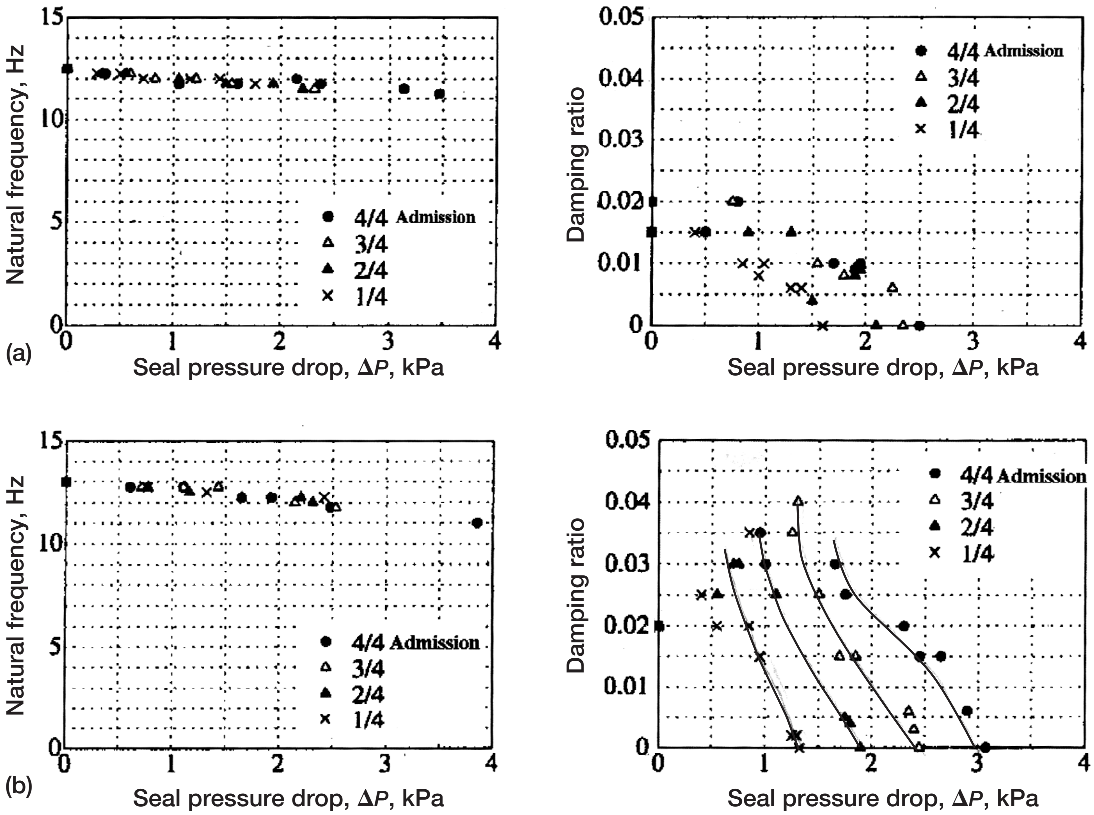


Figure 45.—Effect of swirl breakers. (a) Inlet swirl breaker only. (b) Multiple-chamber swirl breakers (three chambers and inlet). (Kanki et al., 2003.) Courtesy ISCORMA–2.

labyrinth chambers, with four blocks per chamber almost coinciding with the admission flow blocks. The damping ratio was derived from the free decay vibration caused by an impulse hammer striking the rotor. The rotor speed did not alter the results for this model and low-speed conditions. The computations were carried out using the theory of Kostyuk (1972) on a 130-mm-diameter, 0.25-mm-radial-clearance labyrinth seal with 6- and 9-mm cavity chamber height and width, respectively, and zero rotational speed.

These examples illustrate the conflicting demands of negative preswirl for rotor stability and positive preswirl to mitigate turbine cavity heating and flow blockage losses of turbine blade cooling fluid. These conflicts must be properly balanced and resolved early in the design stage (see also part 3).

***Effects of axial flows***.—Figure 47 illustrates a rotor housing study with large clearances to determine fluid effects in the convergent and divergent zones. At the smallest clearance the axial flow velocity was consistently zero, but the oil was axially pumped into and out of the divergent and convergent zones, respectively, with secondary flow zones in the high-clearance zone. In flow visualization experiments these zones were clearly observed (Braun et al., 1987). However, for this case these patterns were significantly changed by small axial pressure gradients (e.g., 0.1 bar; 1.45 psi), and secondary flow zones tended to be small or vanished altogether.

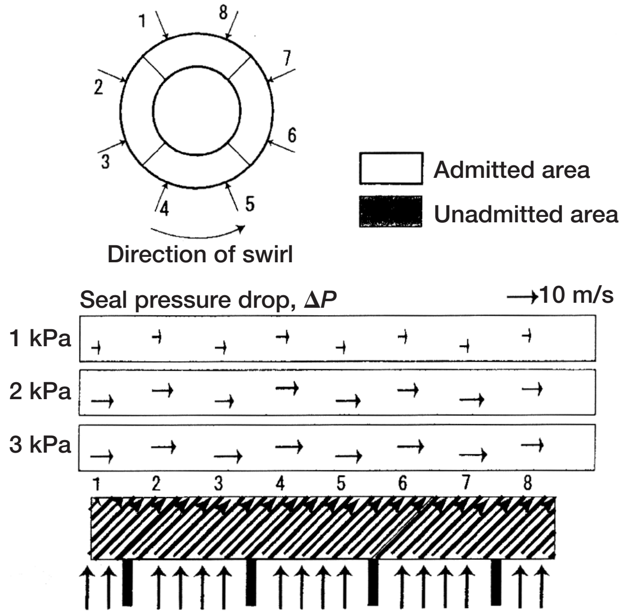


| $\Delta P$ | 1 | 2 | 3 | 4 | 5 | 6 | 7 | 8 | $V_{avg}$ |
|---|---|---|---|---|---|---|---|---|---|
| 1 kPa | 0.88 | 0.88 | 1.08 | 1.26 | 0.88 | 0.88 | 0.88 | 1.26 | 3.4125 |
| 2 kPa | 1.03 | 0.95 | 0.85 | 1.03 | 1.12 | 0.95 | 1.12 | 0.95 | 7.1625 |
| 3 kPa | 0.88 | 0.95 | 1.08 | 1.08 | 1.02 | 1.04 | 1.08 | 0.88 | 8.4375 |
| Average | 0.93 | 0.93 | 1.00 | 1.12 | 1.01 | 0.96 | 1.03 | 1.03 | |

(a)

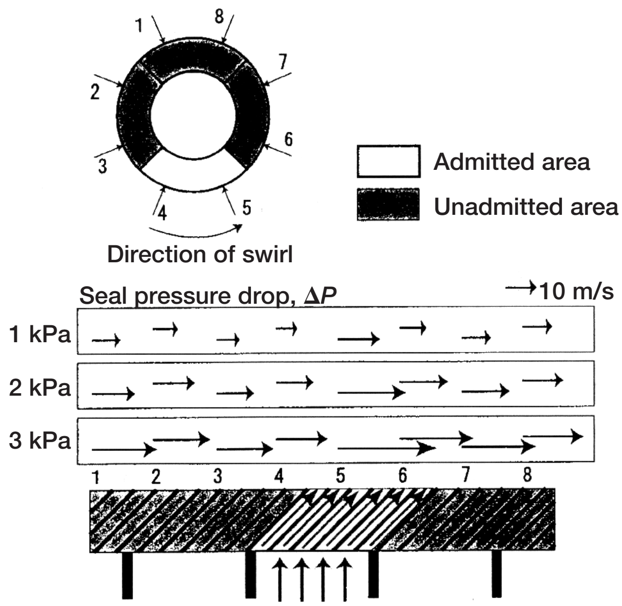


| $\Delta P$ | 1 | 2 | 3 | 4 | 5 | 6 | 7 | 8 | $V_{avg}$ |
|---|---|---|---|---|---|---|---|---|---|
| 1 kPa | 0.95 | 0.90 | 0.79 | 0.73 | 0.67 | 1.33 | 0.85 | 0.95 | 10.15 |
| 2 kPa | 0.78 | 0.82 | 0.79 | 0.71 | 0.71 | 1.29 | 0.92 | 0.92 | 17.05 |
| 3 kPa | 0.81 | 0.86 | 0.76 | 0.76 | 0.69 | 1.31 | 0.98 | 1.0 | 24.2 |
| Average | 0.85 | 0.86 | 0.78 | 0.73 | 0.69 | 1.31 | 0.92 | 0.96 | |

(b)

Figure 46.—Measured swirl velocity. (a) 4/4 admission. (b) 1/4 admission. (Kanki et al., 2003.) Courtesy ISCORMA–2.

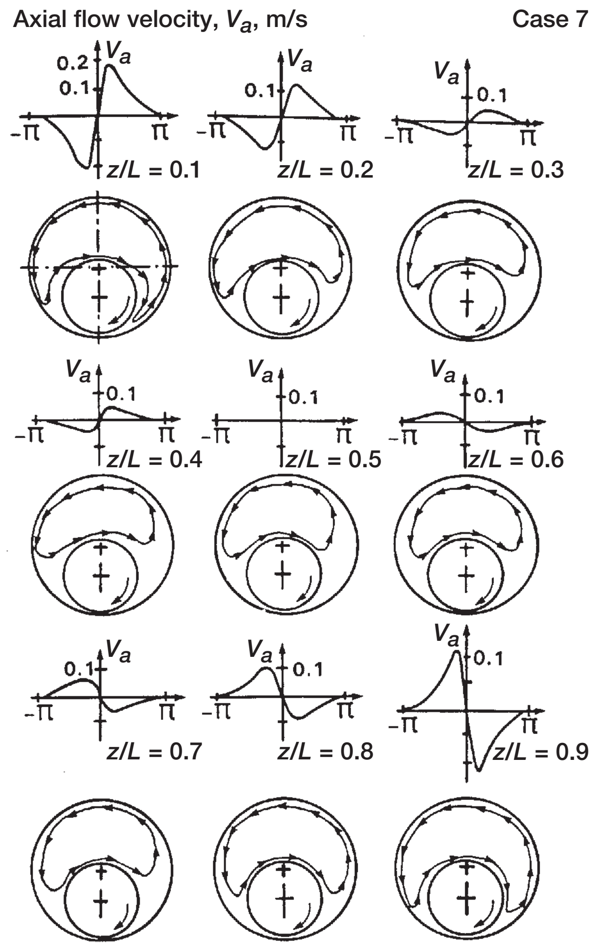


Figure 47.—Mean axial flow distribution along unwrapped circumferential direction and secondary flow patterns of a bearing at various axial planes. Pressure drop, 0; rotor precession frequency, $\omega_p$, 0.

## Summary

Although advances in computational methods have increased our capability to determine forces in complex systems, feedback and validation of field data remain primarily in the proprietary realm, complicating information exchange. In one such exchange Thompson provided an average damping parameter for 115 individual compressor stages contained in 20 multistage bodies, but details are not likely to surface.

Some physical descriptions of the instabilities given by, for example, Armstrong seem classic. Armstrong, in commenting on Alford's paper, writes that at a certain temperature the frequency of mode vibration in an annular air cavity with six wavelengths is equal to the sixth diametrical mode of the stator. Under these conditions air gap variations in the labyrinth due to the stator vibration excite vibrations in the cavity. In turn, the resulting cavity pressure oscillations act on the stator and, if the phase is correct, self-excited stator oscillations occur. The mechanism could be stopped by inserting 24 equally spaced radial baffles across the air cavity.

The stability work and rules of thumb of Alford and Thomas on turbomachine drum and shroud seals continue to be designed into aeronautical and aeronautical-derivative gas turbines and many industrial steam turbines. Computational fluid dynamics (CFD) coupled with aeroacoustics and aeroelasticity are potential methods for validating these rules of thumb and have been developed. However, the field validation data and computational time associated with such a systematic program are unlikely to be supported unless a costly failure occurs. For example, the classic "fix" is still to add a split (severed) damper ring or cylindrical damper drum as a cure for aeronautical engine seal failures.

Compressor blade tip vortices can engender a local stall region that grows into a rotating stall cell. Stage whirl instability is instigated when a blade stalls, developing a separation region, unloading the blade, and failing to produce sufficient pressure to maintain flow around it. The differential angles of attack cause the stall zones to propagate from the pressure side to the suction side of each blade opposite the direction of rotation. Storace et al. demonstrated the predominance of backward whirl over the operating range of a statically offset rotor in a four-stage, low-speed compressor. They also found that doubling the rotor tip clearance dropped torque efficiency by 1.6 points versus 0.9 point for doubling the hub stator clearance.

The data of Childs and field data reported in NASA Conference Proceedings served as sources of design information for the development of computational codes by Schuck and Nordmann, San Andres, and Tam to deal with instabilities. Equally important are the data from Bently Rotordynamics Research and Development Corporation and now Bently Pressurized Bearing Company.

The rotordynamics codes of Nordmann, INDSEAL developed by Shapiro (1996), SCISEAL developed by Athavale, and TAMSEAL developed by San Andres, the three-dimensional fluid dynamics work of Tam et al., the CFD model, and the "lumped"-fluid-parameter model of Muszynska provide a foundation for studying the dynamics of rotor seal and bearing systems. (See also Hendricks, 1996.)

These codes, the work of Tam et al., and the Bently and Muszynska models related herein corroborate and implicate that destabilizing factors are related though fluid average circumferential velocity. However, the dynamics of the rotational flow field are complex with bifurcated secondary flows that significantly alter the circumferential velocity. Several numerical experiments were carried out with the Tam et al. and CFD models and Bently and Muszynska's lumped-parameter model. Fluid injection and/or preswirl of the flow field opposing the shaft rotation significantly intensified these secondary recirculation zones and thus reduced the average circumferential velocity, whereas injection or preswirl in the direction of rotation significantly weakened these zones. A decrease in average circumferential velocity was related to an increase in the strength of the recirculation zones and thereby promoted stability. The lumped-parameter model describes the dynamic forces for relatively large but limited ranges of parameters and is extremely useful in system dynamic analysis of rotor bearings and seals.

Seals play a prominent role in stabilizing turbomachines, and understanding of sealing forces in high-power-density machines has emerged, although the details continue to be analyzed yet today. *Correcting the seals enabled the space shuttle's high-pressure fuel turbopump to operate successfully.* Also, correcting the fluid injection to control seal preswirl of the fuel turbopump enabled the LH–7A hydrogen-oxygen engine to operate safely.

Finally, if the engine and power conversion industry wants a smooth-operating, reliable, long-lived machine, it must pay very close attention to sealing dynamics. Does this mean that gas path or power-stream dynamics are not important? Of course not. Brayton cycle machines, for example, are fairly mature. However, turbomachine sealing dynamics represents your competitive edge.

# Appendix A

# Numerical and Analytical Modeling

### Part 1—Numerical Modeling

For an observer located in the rotating frame the relation between absolute, relative, and grid velocity becomes

$$\vec{U}_{\text{abs}} = \vec{\tilde{U}} + \vec{\omega}_P \times \vec{r} \qquad (A\text{–}1)$$

where $\vec{U}_{\text{abs}}$ is the fluid absolute velocity, $\vec{\tilde{U}}$ the fluid relative velocity, $\vec{\omega}_P$ the rotor precession (perturbation) frequency, and $\vec{r}$ the local radius in the fluid. For any given perturbation speed ratio the transformed moving-coordinate grid system must be consistent with the specified rotor precessional speed imposed (fig. 27).

***Governing equations***.—Conservation of mass can be written as

$$\frac{\partial}{\partial t}(\rho J) + \nabla \cdot \left(\rho \vec{\tilde{U}}\right) J = 0 \qquad (A\text{–}2)$$

where $\rho$ is the fluid density and $J$ the determinant of the Jacobian matrix (i.e., the physical volume of a grid cell in the finite difference approach).

From the Euler identity and the small circular orbit assumption the rate change of the Jacobian matrix can be made to vanish. The "quasi-steady" analysis is valid and equation ($A$–2) takes the final form

$$\nabla \cdot \left(\rho \vec{\tilde{U}}\right) J = 0 \qquad (A\text{–}3)$$

The three-dimensional, turbulent, time-averaged, "conservative"[4] Navier-Stokes (N–S) equation in the coordinate system rotating at the perturbation angular velocity $\omega_P$ is

$$\frac{\partial\left(\rho \vec{\tilde{U}} J\right)}{\partial t} + \nabla \cdot \left(\rho J \vec{\tilde{U}} \vec{\tilde{U}}\right) = -J \nabla p - J \left[ \overbrace{\rho \vec{\omega}_P \times \left(\vec{\omega}_P \times \vec{r}\right)}^{\textit{Centrifugal}} + \underbrace{2\rho \vec{\omega}_P \times \vec{\tilde{U}}}_{\textit{Coriolis}} \right] + \overbrace{J \nabla \tilde{\vec{\tau}}}^{\textit{Shear}} + \underbrace{J \rho \vec{g}}_{\textit{Body force}} \qquad (A\text{–}4)$$

It is very important to note the centrifugal and Coriolis source terms arising from the shaft whirling at $\omega_P$.

[4]Conservation is respected at every grid point in the mesh; viscous fluctuating terms are time averaged.

In this equation the shear stress tensor $\nabla\tilde{\tilde{\tau}}$ contains time-averaged Reynolds stress terms. The turbulence model used in our seal flow simulations makes use of the eddy viscosity concept to compute those terms, resulting in the following expressions:

$$J\nabla\tilde{\tilde{\tau}} = -\rho u_i u_j J = \mu_t\left(\frac{du_i}{dx_j} + \frac{du_j}{dx_i} - \frac{2}{3}\nabla \cdot U\delta_{ij}\right) \qquad (A-5a)$$

where the turbulent eddy viscosity $\mu_t$ is proportional to the mixture density of the turbulent flow $\rho$, the rate of strain $\phi$, and the square of the mixing length of turbulence $l_m$. The centrifugal and Coriolis forces appear to be caused by the coordinate rotation and are incorporated into the computational model as additional volumetric momentum sources.

$$S(\tilde{u}) = -2\rho\omega_P\tilde{v}\ \mathrm{Vol}_{\mathrm{cell}}, \qquad S(\tilde{v}) = \left(\rho\omega_P^2 r + 2\rho\omega_P\tilde{u}\right)\mathrm{Vol}_{\mathrm{cell}} \qquad (A-5b)$$

where $\mathrm{Vol}_{\mathrm{cell}}$ is the physical volume of a grid cell (from the Jacobian $J$).

***Turbulence modeling for seal and bearing flows***.—The characteristics of seal and bearing flows can be summarized as strong swirl, high viscosity, and high pressure drop associated with significant wall roughness and small clearances. Several attempts at predicting rotating turbulent flows indicate that using complex full Reynolds stress equations was only as good as using those obtained with simple correction of the turbulence generation and dissipation $k$-$\varepsilon$. Furthermore, existing turbulence models can successfully predict only simple boundary layer or mildly recirculating flows.

*Effects of surface curvature and rotating flows on turbulence*: Several investigators have attempted to extend both the algebraic Reynolds stress and $k$-$\varepsilon$ models for turbulent rotating flows. Salient features of the effects of surface curvature and rotating flows on turbulence modeling can be discussed briefly. Most relevant approaches are based on Bradshaw's suggestion (Bradshaw, 1973. See also Hoffman et al., 1985; Muck et al., 1985; and Smits et al., 1979.) that the streamline curvature effects can be modeled by modifying the turbulence length scale. The two most relevant approaches are those of Rodi (1979) and Launder et al. (1977). Both incorporate the "rotating" correction into the constants of the turbulence dissipation rate term. The extension of Rodi introduces a correction to the model constant in the generation part of the $\varepsilon$ equation source term. The Launder extension modifies the destruction part of that term in a similar manner by introducing the Richardson flux number:

$$R = \frac{k^2}{\varepsilon^2}\frac{u}{r^2}\frac{\partial ru}{\partial r}$$

Both the Rodi and Launder et al. approaches respond to the angular speed, to the swirl velocity gradient, and to the turbulence time scale. Analysis of the Richardson flux correlation indicates that in the regions of negative velocity gradients $R$ is also negative and smaller $\varepsilon$ decay intensifies the turbulence level. Negative Richardson flux starts increasing from the shaft walls (from inner to outer walls) and becomes maximum at the separation regions. Then, the gradient of Richardson flux drops sharply and changes to a positive number where the turbulence level is damped and a secondary recirculating zone appears.

*Two-equation model extensions:* In extending the two-equation turbulence model, like other turbulence flow researchers (Rodi, 1979, and Bradshaw, 1969, in particular), Kim and Rhode (1999) have also incorporated Richardson flux corrections, modified the turbulence mixing-length scale, and elaborated on the log-law wall function with an attempt to account for swirling streamline-curvature flow influences on the $k$-ε turbulence model. They claimed only very limited success.

For coupled swirling flows these models fail to capture the essential physics of usually anisotropic, nonhomogeneous, and three-dimensional turbulence structures. However, the general consensus is that the empirical constants in the semi-empirical $k$-ε model are invalid for complex flows anyway. For these reasons a simple Prandtl mixing-length model was used to represent the turbulence in seal and bearing flow passages. Further, the purpose herein is to develop the dynamics of fluid-solid-coupled modeling rather than to develop a turbulence model for nonplanar interfaces.

*Prandtl mixing-length turbulence model*: The zero-equation Prandtl mixing-length model is simple and well established, and the mixing-length scale is determined by the clearance. The turbulence model used the eddy-viscosity concept

$$\frac{y}{\zeta} \le \frac{\alpha}{b}, \qquad \frac{l_m}{\zeta} = \frac{by}{\zeta}, \qquad b = 0.435; \qquad \frac{y}{\zeta} > \frac{\alpha}{b}, \qquad \frac{l_m}{\zeta} = \alpha, \qquad \alpha = 0.09$$

where $\zeta$ is the normal distance measured between the stator and rotor surfaces, $y$ is the minimum local distance measured from the stator and rotor surfaces, and $b$ and $\alpha$ are coefficients.

***Numerical algorithm, boundary conditions, and grid***.—An implicit pressure-correction method, the SIMPLEST algorithm proposed by Spalding (1981), was used to solve the numerical model. The momentum equations were first solved with a guessed pressure field. An implicit successive iterative method with a pressure-correction equation derived from the continuity equation was used in the algorithm. Subsequent pressure and momentum were corrected to satisfy continuity. The whole process was repeated until satisfactory convergence was achieved.

At the flow inlet both the pressure and the circumferential velocity (with or without preswirl) were specified. Only pressure was specified at the outlet. For a specific perturbation speed ratio the proper rotor rotational speed and the rotor precessional speed were specified. The transformed moving coordinate grid system must be consistent with the specified rotor precessional speed imposed. The no-slip velocity condition at the rotor and stator walls and fluid shear stresses acting on the rotor and stator surfaces were generally incorporated. Shear stresses on the rotor and stator surfaces were calculated on the basis of the Couette flow assumption with universal "log-law" of the wall function approach adopted. For the roughness of the wall boundary specifications Childs et al. (in NASA CP–2133, 1980, and in NASA CP–2443, 1986) demonstrated that surface roughness depends on the flow direction (i.e., there is higher resistance to flow in the axial than in the circumferential direction). Consequently, different rough-to-smooth correlations were specified in the axial and circumferential directions (the coefficients 2.9 and 1.1 were multipliers of the smooth friction relations). Finally, cyclic boundary conditions in the circumferential direction were adopted.

A three-dimensional, nonorthogonal, body-fitted computational grid has been selected for the computations (fig. 28). The grid allows for steep variations in physical parameters (fluid preswirl in particular). It has been also optimized according to a surface Reynolds number criterion ($Re^+ < 100$) of the imposed wall function to ensure proper resolution of the boundary layer near the rotor and stator walls.

***Dynamic forces***.—Fluid circumferential force components $F_r$ (radial) and $F_t$ (tangential) were calculated from the pressure distribution

$$-F_r = \int_0^{2\pi}\int_0^{l} p\cos(\phi) R_i \, d\phi dz, \quad -F_t = \int_0^{2\pi}\int_0^{l} p\sin(\phi) R_i \, d\phi dz \qquad (A\text{–}6)$$

where $R_i$ is the shaft radius, $l$ denotes bearing or seal length, and $\phi$ is the angle measured (clockwise) from the position of minimum clearance.

The third component of the fluid force $F_z$ is related to the axial flow such as that occurring in seals of pumps and compressors due to balance piston loading. In bearings $F_z$ is usually small relative to $F_r$ and $F_t$, but for seals in machines of the SSME category the axial flow and pressure drop are large and $F_z$ has a significant value. However, it was assumed to remain implicitly linked to $F_t$ and is a source for future work.

### Part 2—Analytical Lumped-Parameter Model

The lumped-parameter model represents an analytical approach to rotordynamics with fluid film components (Bently et al., 1986; and Muszynska, 1986, 1988a, 2001). The fluid force model was identified by using extensive modal perturbation testing (Muszynska and Bently, 1990; Muszynska, 1995).

The most important novel feature in the model is the fundamental assumption that the fluid dynamic force is related to the circumferential flow, which is generated by rotor rotation in the rotor/stationary clearance. Note that this model is applicable for fluid-lubricated bearings, seals, and any other radial or axial clearances between a rotating and stationary part.

At the beginning it is assumed that the rotor is <u>centered</u> within the clearance and the averaged (lumped) fluid force is <u>rotating</u> at the angular velocity $\lambda\omega_R$ (not a constant $\omega_R/2$, as is often assumed, e.g., Black and Jenssen, 1969–70), where $\omega_R$ is rotor rotational speed. The fluid force expressed in coordinates rotating at angular velocity $\lambda\omega_R$ has three classical components: stiffness $K$ (stiffness force proportional to shaft radial displacement $z_r$), damping $D$ (damping force proportional to shaft radial velocity $dz_r/dt$), and fluid inertia $M$ (fluid inertia force proportional to radial acceleration $d^2z_r/dt^2$, where $z_r = x_r + jy_r$ is the complex displacement of the rotor within the clearance. In stationary coordinates the fluid force becomes

$$-F = Kz + D\left(\dot{z} - j\lambda\omega_R z\right) + M\left(\ddot{z} - 2j\lambda\omega_R\dot{z} - \lambda^2\omega_R^2 z\right) \tag{A-7}$$

$$z = x + jy, \qquad j = \sqrt{-1}, \qquad |z| = \sqrt{x^2 + y^2}, \qquad \cdot = d/dt$$

where $\lambda$ is the fluid circumferential average velocity ratio (a measure of the circumferential flow strength), $z$ is shaft radial complex displacement (conventionally, $x$ denotes horizontal, and $y$ denotes vertical), and $z = z_r \exp(j\lambda\omega_R)$ is the transformation from stationary to rotating coordinates.

In the bearing and seal coefficient format and in the chosen reference system (fig. 27) the fluid force for clockwise rotor rotation is as follows:

$$-F = \frac{1}{|z|}\begin{vmatrix} -F_r & -F_t \\ F_t & -F_r \end{vmatrix}\begin{vmatrix} x \\ y \end{vmatrix} = \begin{vmatrix} K - M\lambda^2\omega_R^2 & D\lambda\omega_R \\ -D\lambda\omega_R & K - M\lambda^2\omega_R^2 \end{vmatrix}\begin{vmatrix} x \\ y \end{vmatrix}$$

$$+\begin{vmatrix} D & 2M\lambda\omega_R \\ -2M\lambda\omega_R & D \end{vmatrix}\begin{vmatrix} \dot{x} \\ \dot{y} \end{vmatrix} + \begin{vmatrix} M & 0 \\ 0 & M \end{vmatrix}\begin{vmatrix} \ddot{x} \\ \ddot{y} \end{vmatrix} \tag{A-8}$$

Note that the cross-coupled stiffness term is generated here by the radial damping due to rotation and is proportional to $\lambda$ and $\omega_R$. The radial stiffness is modified by centrifugal inertia and carries the negative sign. “Cross damping” is due to the Coriolis inertia force.

When in response to external excitation by nonsynchronously rotating force $P\exp(j\omega_P t)$, the rotor precessional (orbital) motion is circular with amplitude $A$, phase $\alpha$, and frequency $\omega_P \neq \omega_R$; that is,

$$z = Ae^{j(\omega_P t + \alpha)} \tag{A–9}$$

When equation (*A*–9) is substituted into equation (*A*–7), the following relation results:

$$Pe^{j\omega_P t} = Ae^{j(\omega_P t+\alpha)}\left[K + jD(\omega_P - \lambda\omega_R) - M(\omega_P - \lambda\omega_R)^2\right] \tag{A–10a}$$

The external force divided by the rotor response yields the fluid-related complex dynamic stiffness

$$\frac{P}{Ae^{j\alpha}} = K - M(\omega_P - \lambda\omega_R)^2 + jD(\omega_P - \lambda\omega_R) \equiv K_D + jK_Q \tag{A–10b}$$

Muszynska and Bently (1990) and Muszynska (1995) identified the direct (real) $K_D$ and the quadrature (imaginary) $K_Q$ components of the fluid dynamic stiffness in equations (*A*–10) by using nonsynchronous forward and backward perturbation testing. Tam et al. (1988) also obtained the elements of the fluid dynamic stiffness from numerical calculations. (Selected results are illustrated in figures 29 to 33.) Note the high value of the fluid inertia effect, $M = 4.63$ kg, exceeds by about 400 times the fluid mass in the seal (fig. 30).

For an isotropic shaft carrying a disk of mass $M_1$ and a journal of mass $M_2$ and supported by a fluid film bearing on one end and a pivoting rolling-element bearing on the other end, with shaft partial stiffness $K_1$ (left side) and $K_2$ (right side) (fig. 48), the governing equations become

$$M_1\ddot{z}_1 + D_s\dot{z}_1 + (K_1 + K_2)z_1 - K_2 z_2 = m_2 r\omega_R^2 \exp(j\omega_R t) \tag{A–11}$$

$$M_2\ddot{z}_2 + M_f(\ddot{z}_2 - 2j\omega_R\dot{z}_2 - \lambda\omega_R^2 z_2) + [D + \psi_2] \\ \times(\dot{z}_2 - j\lambda\omega_R z_2) + (K_0 + \psi_1)z_2 + K_3\, z_2 + K_2(z_2 - z_1)] = 0 \tag{A–12}$$

$$z_i(t) = x_i(t) + j\, y_i(t),\ i = 1,2 \tag{A–13}$$

where $D$ is fluid damping and $D_s$ is external damping; $K_0$ and $M_f$ are fluid film stiffness and fluid inertia; $m_2$ and $r$ are the mass and radius of unbalance, respectively; and $\psi_1$ and $\psi_2$ are nonlinear stiffness and damping functions of the journal radial displacement $|z_2|$, respectively.

Muszynska (1985, 2001) gives and discusses the solution for the stability threshold of pure shaft rotation:

$$\omega_R^{\mathrm{ST}} = (1/\lambda)\sqrt{\left(\frac{K_1}{M_1}\right) + \frac{K_2(K_0 + K_3 - M_2K_1/M_1)}{M_1(K_2 + K_0 + K_3 - M_2K_1/M_1)}} \tag{A–14}$$

For $\omega_R < \omega_R^{\mathrm{ST}}$ the rotor is stable; for $\omega_R \geq \omega_R^{\mathrm{ST}}$ the rotor becomes unstable. Because in equation (*A*–14) the fluid inertia and the journal mass are small relative to the disk mass, and shaft stiffness $K_1$ dominates other stiffnesses being in sequence, the threshold of stability can be approximated as

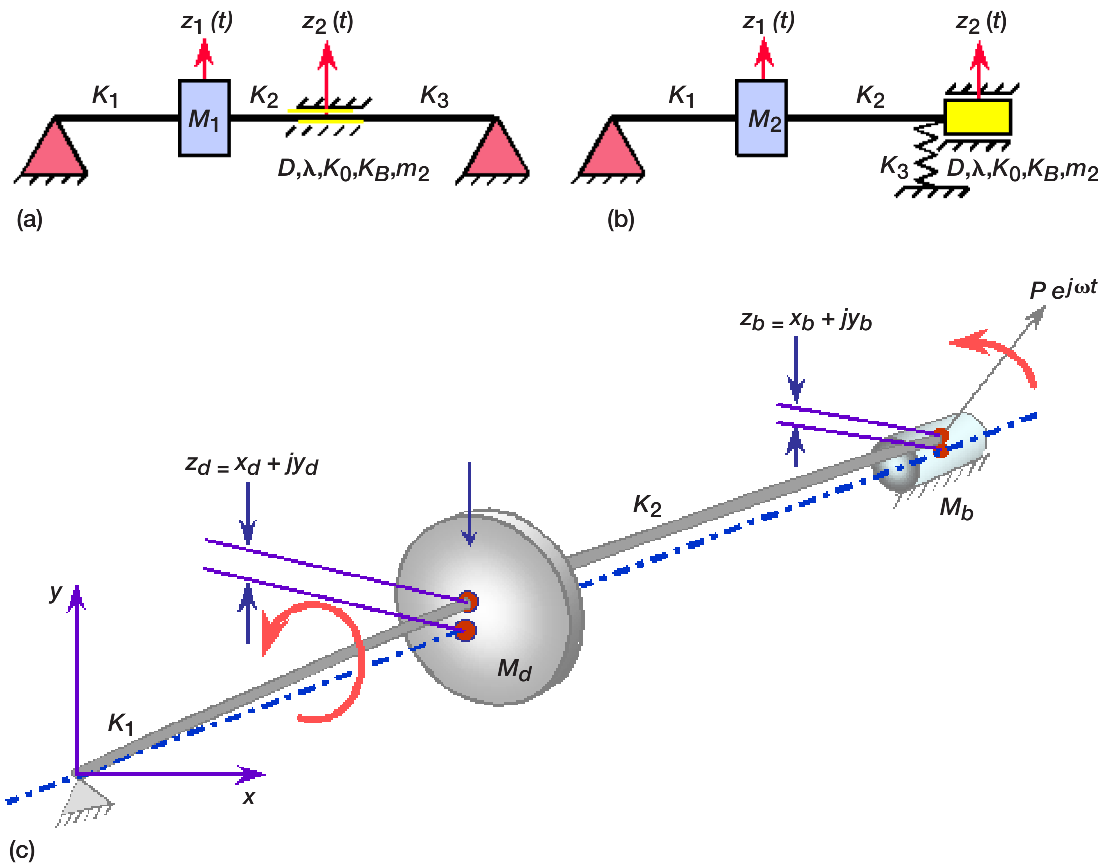


Figure 48.—Rotor and fluid film modeling. (a) Rotor and seal model. (b) Rotor and bearing model. (c) Rotor system accounting for two-complex-mode model. Nonsynchronous perturbation force *P* applied at the journal (or at the disk) as in equations (A-1) and (A-12). (Muszynska, 2001.)

$$\omega_R^{ST} = (1/\lambda)\sqrt{(K_1/M_1)} \qquad (A\text{–}15)$$

Note that the rotor instability thresholds (eqs. ($A$–14) and ($A$–15)) are inversely proportional to λ.

The rotor and fluid model (eqs. ($A$–11) to ($A$–13)) also provides stability criteria for the unbalance-related synchronous response of the rotor (Muszynska, 1986). It also explicitly provides the postinstability-threshold rotor self-excited vibrations, fluid whirl and fluid whip, as two varieties of the same phenomenon (fig. 16). Note that in equations ($A$–11) and ($A$–12) it has been assumed that the journal was centered within the bearing clearance. Muszynska (1986b) solved the more realistic cases considering eccentric positions for the journal. Below there is an example on how the nonconcentric cases can be handled.

Implementation of the fluid-force model (eq. ($A$–8)) into another one-disk model of an isotropic rotor, operating in a fluid environment is as follows:

$$M_d\ddot{z}+D_s\dot{z}+K_d z+D\left\{\dot{z}-j\left[\lambda-\lambda_n\left(|z|\right)\omega_R z\right]\right\}+\left[K+\psi_1\left(|z|\right)\right]=P\exp\left(j\delta\right) \qquad (A\text{–}16)$$

where $M_d$ and $K_d$ are rotor modal mass and stiffness, respectively, for the first lateral mode and $P$ and δ are the magnitude and angular orientation, respectively, of a constant radial force applied to the rotor. At $|z| = 0$ (concentric case) $\lambda_n = \lambda$; then, with increasing eccentricity, $\lambda_n$ decreases to zero, which means that the circumferential flow is no longer dominant. In this model rotor unbalance, fluid nonlinear damping, and fluid inertia are not included for clarity. The model contains, however, a nonlinear function of fluid circumferential average velocity ratio $\lambda_n$, which is a decreasing function of the rotor radial displacement $|z|$. This model reflects the fact that when the rotor is concentric within the clearance, the circumferential flow is the strongest. A rotor at higher eccentricity suppresses the circumferential flow (some secondary flows occur and most often the axial flow then becomes dominant). The model (eq. (*A*–16)) shows the nonlinear effect of the fluid force when constant external force displaces the rotor from the concentric position in the fluid-filled clearance.

The instability threshold for the linear part of the rotor model (eq. (*A*–16)) is as follows:

$$\omega_R^{\mathrm{ST}} = \frac{1}{\lambda}\left(1+\frac{D_s}{D}\right)\sqrt{\frac{K_d+K}{M_d}} \qquad (A\text{–}17)$$

As previously (eqs. (*A*–14) and (*A*–15)) the instability threshold is inversely proportional to the fluid circumferential average velocity ratio $\lambda$. Changing this ratio would directly affect the rotor instability threshold. One way to achieve this change is to move the rotor to higher eccentricity by applying radial force. There is also another way. It has been shown that external injection of the fluid into the seal clearance in the tangential direction, either the same or opposite to rotor rotation, changes $\lambda$ as well as the fluid radial stiffness:

$$\lambda+\lambda(|z|)\rightarrow\lambda+\lambda(|z|)\pm\lambda_{\mathrm{ext}}, \quad K+\psi_1\rightarrow K+\psi_1+K_{\mathrm{ext}} \qquad (A\text{–}18)$$

The new $\lambda$ depends on the direction of injection, so it can increase or decrease. The fluid radial stiffness always increases with any direction of injection because it creates additional pressure in the clearance. As can be seen in equation (*A*–17), if the fluid is injected in the direction opposite to rotor rotation, the rotor instability threshold may be significantly increased (Muszynska et al., 1988b; Muszynska and Bently, 1989; and Muszynska, 2001):

$$\omega_R^{\mathrm{ST}} = \frac{1}{\lambda-\lambda_{\mathrm{ext}}}\left(1+\frac{D_{R,\mathrm{ext}}}{D}\right)\sqrt{\frac{K_0+K_R+K_{\mathrm{ext}}}{M_R}} \qquad (A\text{–}19)$$

Equation (*A*–19) clearly shows that external tangential injection (1) alters rotor stability and (2) increases radial fluid film stiffness. With control of both issues, tangential injection and pressure, rotordynamic systems can be "walked through" rotor instabilities (Bently et al., 2002).

The major effort for the CFD analysis is then to define the effects of $\lambda$, which is a measure of circumferential flow strength, fluid film stiffness, and damping with coupling to the shaft dynamics, and thus solve the problem of fluid-solid coupling interaction.

# Appendix B

## Turbomachine Fluid/Structural Interactions

All turbomachines respond to unsteady thermal fluid dynamic processes, but the structural codes discussed here closely replicate only structural dynamic imbalance. The catch is that these dynamic imbalances are of mechanical origin (i.e., added torque through weight placement) and conform to structural responses. On the other hand, thermal fluid dynamic perturbations are driven by the inherent unsteadiness of the flow coupled through fluid/structural interactions to either reinforce or damp perturbations. Unless these factors are built into the engine codes, resonant or unstable engine phenomena will always appear that may necessitate engine rework or at best altering component design. Although expensive in terms of development time and testing cost, experimental validation of computations is a necessary part of certification.

### Full-Scale Systems

***Industrial gas turbine***.—As turbomachines become more sophisticated, the need for full component and engine assembly test and analysis becomes acute. Although these analyses are expensive to set up and computationally intensive to carry out, whole-engine gas path modeling is being developed by several researchers (e.g., Numerical Propulsion System Simulation (NPSS) by NASA GRC program manager Joseph Veres), and structural analysis codes exist (e.g., MSC–NASTRAN).

Surial and Kaushal (2003) applied MSC–NASTRAN superelements to a Rolls-Royce aeroderivative, three-spool gas turbine with (1) representing the engine casing, (2) the low-pressure turbine (LPT), (3) the intermediate-pressure turbine rotor (IPT), and (4) the high-pressure turbine (HPT). The casing superelement (0) was modeled by using quadrilateral (QUAD4) and three-node (TRIA3) linear shell elements (first order) and standard beam elements. The casing superelement model had eight modules:

1. Front end and low-pressure case
2. Intercompressor duct
3. Plenum
4. Aeronautical intercase
5. Combustor
6. High-pressure case
7. IPT case
8. LPT case

Other superelements included (10), the LP rotor; (20), the IP rotor; (30), the HP rotor; (40), the engine coupling; (50), the pedestal shaft; (60), the generator coupling; and (70), the generator rotor. Figure 49 illustrates the computational mesh of the aeroderivative gas turbine with figure 50 showing the LP rotor, IP rotor, and HP rotor or spools. The drive trains were also modeled, and Guyan reduction was mapped each onto a common centerline model. The mode shapes were animated by using PATRAN to determine whirl directions. Modal frequency analysis was performed by using NASTRAN (SOL 111) with gyroscopic effects considered by using NASTRAN sssalter ridgyroa.705. Pedestal damping included CDAMP elements. An unbalance load of $7.22\times10^{-3}$ kg-m (10 oz.-in.) was applied at seven engine locations giving seven excitation and nine computed responses. The results were in good agreement for those points measured (table III).

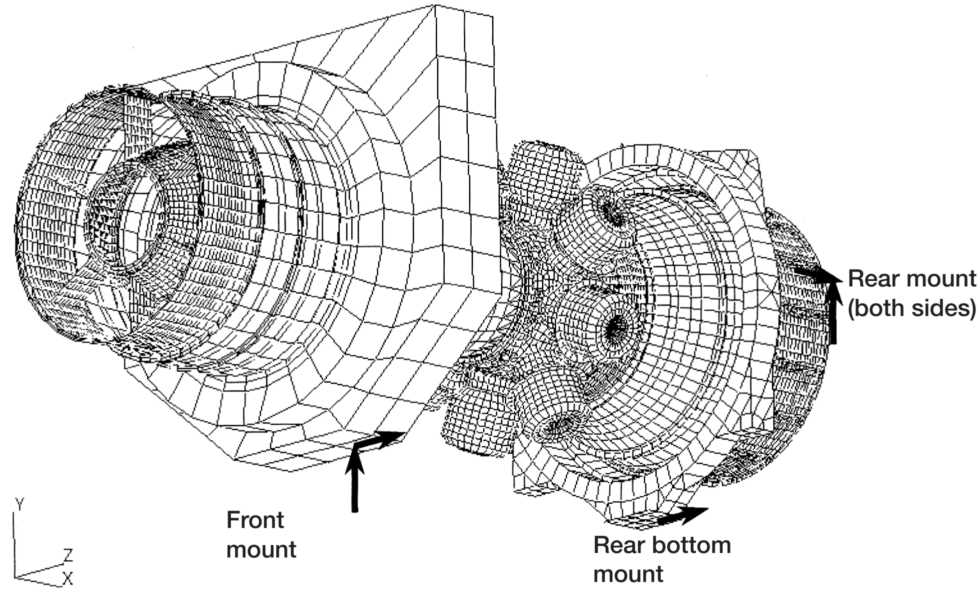


Figure 49.—Finite element model and engine-to-ground mounts. (Surial and Kaushal, 2003.) Courtesy ISCORMA–2.

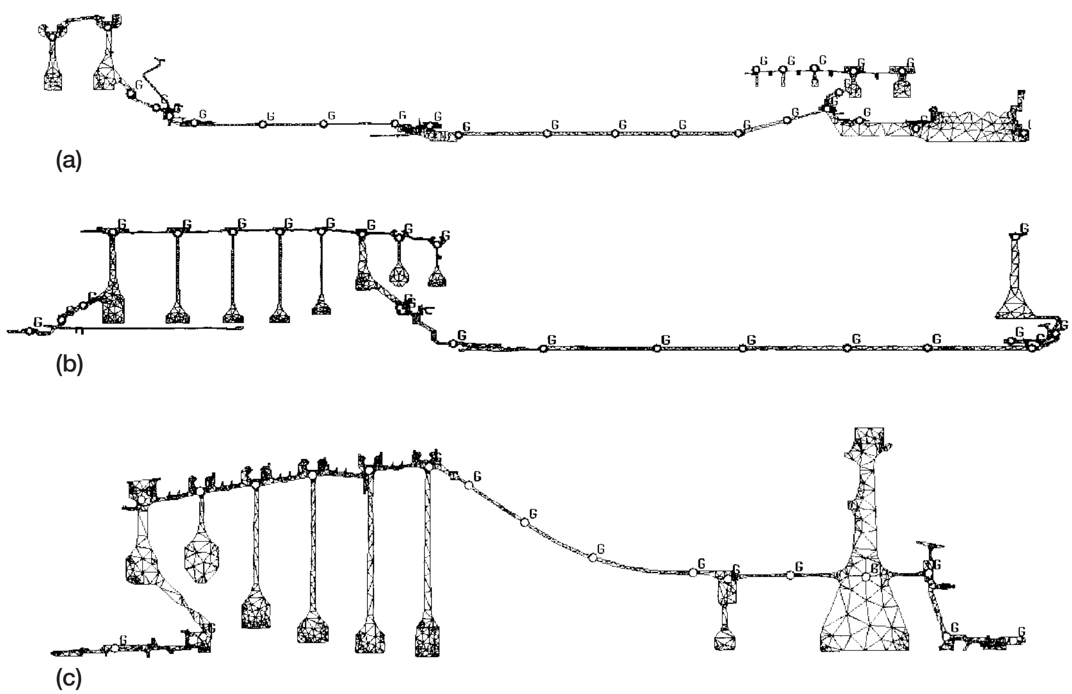


Figure 50.—Illustration of some Guyan points. (a) On LP rotor. (b) On IP rotor. (c) On HP rotor. (Surial and Kaushal, 2003.) Courtesy ISCORMA–2.

TABLE III.—RESULTS OF CRITICAL SPEED ANALYSIS AND MEASUREMENTS

| Mode number | Frequency, Hz | | Description |
|---|---|---|---|
| | Experimental | Computational | |
| 92 | ------ | 9.42 | Drive train torsion |
| 99 | ------ | 21.55 | Drive train torsion |
| 104 | ------ | 25.13 | Engine and generator (axial) coupling |
| 109 | 33.6 | 33.73 | LP rotor mixed whirl |
| 111 | ------ | 37.04 | LP rotor and generator rotor axial |
| 115 | 42.72 | 41.67 | LP rotor mixed whirl |
| 117 | 47.3 | 44.58 | LP rotor forward whirl |
| 121 | ------ | 50 56 | LP rotor reverse whirl |
| 122 | 53.4 | 51.28 | LP rotor pedestal shaft first conical mode |
| 123 | 53.4 | 52.58 | Pedestal shaft second conical mode |

TABLE IV.—NONDIMENSIONAL NATURAL FREQUENCIES FOR THREE BLADE MODELS

| Blade model | Nondimensional natural frequency | | | | |
|---|---|---|---|---|---|
| Cantilevered blade without root cross section | 0.5062 | 0.9002 | 1.8062 | 2.3128 | 3.7909 |
| Cantilevered blade with root cross section | 0.4681 | 0.8388 | 1.7777 | 2.0235 | 3.0766 |
| Blade with disk sector | 0.3190 | 0.4747 | 0.9715 | 1.2170 | 1.7808 |

***Industrial gas-turbine-driven compressor.***—Camatti et al. (2003a) relate instability problems in full-scale testing of gas-turbine-driven, back-to-back compressors with greater details, and Camatti et al. (2003b) give a second system example. Table IV and figure 51 give seal locations and types. The impeller slant-toothed labyrinth seal and the interstage honeycomb balance-piston seal were unstable. The final balance-piston, abradable shroud seal, teeth on rotor (fig. 51(c)) appeared to be stable. The impeller shroud labyrinth seals (fig. 51(a)) were replaced by labyrinth seals with staggered, multiple, axial slots machined into the intertooth cavities and referred to as web seals (fig. 52). These slots were effective in reducing the impeller shroud circumferential fluid force velocity $\Omega\lambda$. The honeycomb interstage seal (fig. 51(b)) was modified by adding convergent taper. The operating taper was a compromise between the need to increase frequency and the need for sufficient damping and was set at 0.06 mm (0.0024 in.) radial. However, because of pressure and thermal effects the machined taper was twice that, or 0.12 mm (0.0048 in.) radial; these changes nearly doubled the damping. Nevertheless, even with changes in the impeller seal (or web seal; fig. 51(a)) and seal tapering (honeycomb), operation with plugged radial-diffused fluid injection holes, or "shunts," provided only marginal improvements. However, opening the shunts to the honeycomb seal inlet (fig. 51(d)) decreased gas swirl (i.e., reduced $\Omega\lambda$; see also figs. 36 and 37), and the system operated without a trace of instability, even to theoretical surge at 120 bar (120 percent operational). Opening the shunts perturbed diffuser and back-side impeller fluid dynamics and balance and decreased or nearly eliminated interstage-seal (fig. 51(b)) inlet gas swirl (i.e., reduced or eliminated $\Omega\lambda$; see also figs. 36 and 37). Recalling that alterations of the CDP seal changed flows throughout the engine (e.g., fig. 12 of part 1), shunt fluid injection may also alter impeller flow and pressure fields and thus enhance power-stream stability. (See also stability criteria in Fulton, 2003).

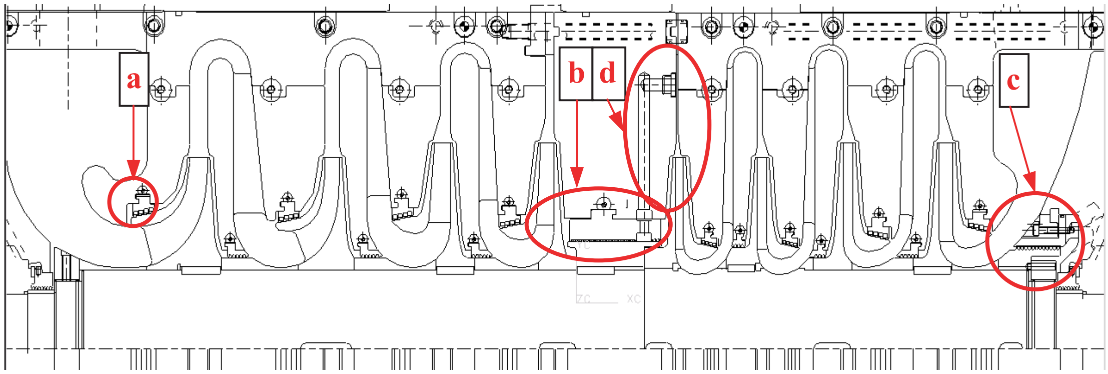


Figure 51.—Compressor cross-sectional drawing showing detail of rotor plus seals. (a) Impeller shroud labyrinth seal. (b) Honeycomb interstage seal. (c) Abradable seal. (d) Honeycomb interstage seal. (Camatti et al., 2003.) Courtesy ISCORMA–2.

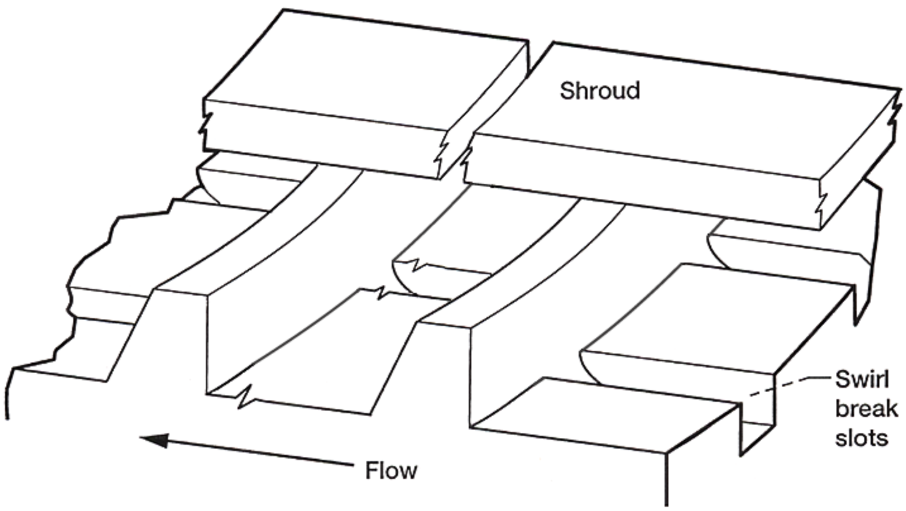


(a)

(b)

Figure 52.—Web seal. (a) Sketch of conceptual web seal. (b) Photograph of web seal or slotted labyrinth seal. (Camatti et al., 2003.) Courtesy ISCORMA–2.

Figure 53 shows the nature of this labyrinth and honeycomb dual-seal concept. The two labyrinth teeth are in the extreme foreground, and between the labyrinth teeth and the honeycomb is a recessed annulus. Within the annulus are shunt holes that connect the high-pressure diffuser to the annulus. These holes can be plugged or open. When they are open, high-pressure diffuser gas flows radially through them into the annulus. Because this annulus contains the highest pressure in the seal, some gas flows toward the foreground, across the two labyrinth teeth, and beyond, flowing radially

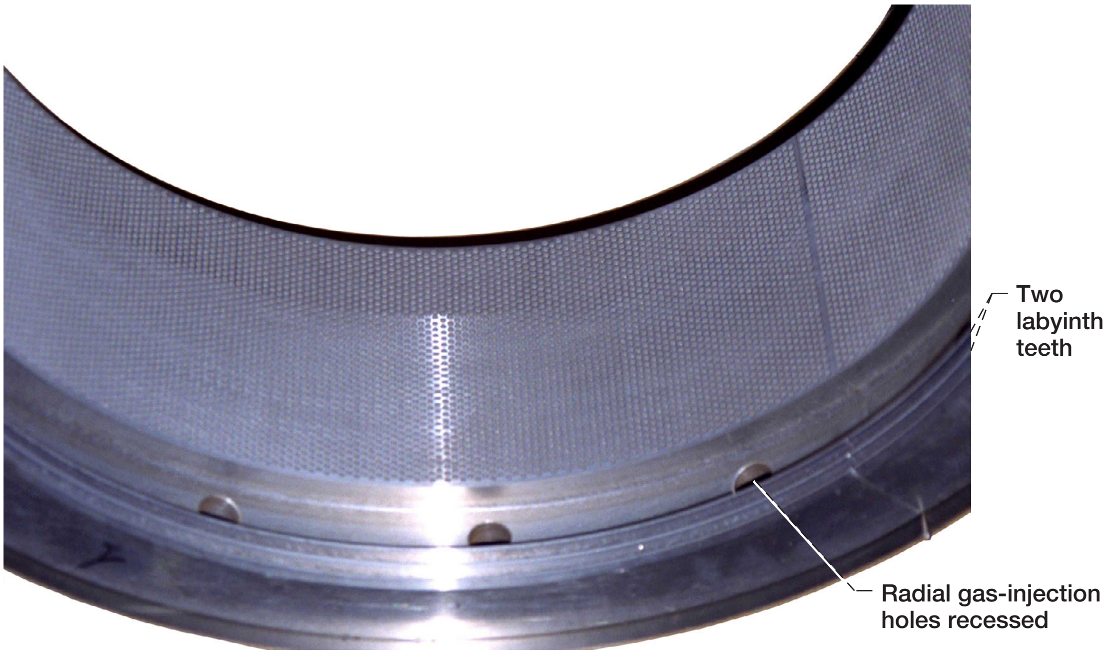


Figure 53.—Honeycomb seal rub region with provisions for shunt. (Camatti et al., 2003.) Courtesy ISCORMA–2.

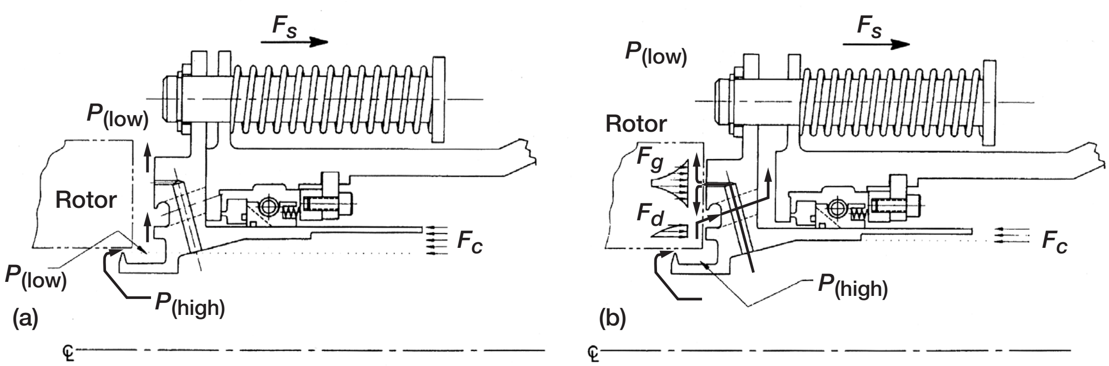


Figure 54.—Aspirating seal GE90 test. (a) At shutdown phase. (b) At steady-state operation. (Tseng et al., 2002.)

outward along the back of the impeller disk. However, most of the injected flow goes through the clearance between the smooth shaft and the honeycomb cells.

In many respects this dual-seal configuration functions like the aspirating seal (fig. 54). In the aspirating seal the labyrinth tooth controls leakage flow at elevated clearances (fig. 54(a)) and forms a high-pressure cavity for the diffused-injected flow in the engine cavity at operating conditions (fig. 54(b)), where flow is controlled by the narrow gap in the face seal (Tseng et al., 2002).

## Components

***Padded-finger seal fluid***.—Altering the geometry of the basic finger seal concept, Braun et al. (2003) developed a new seal that combines the features of a self-acting shaft seal lift pad as an extension of the downstream fingers with an overlapping row of noncontact upstream fingers. The upstream and downstream fingers are further reinforced each by a single row of overlapping fingers (figs. 55 and 56). These overlapping fingers reduce the axial and radial flows along the compliant fingers that allow for radial motion of the shaft/seal interface. The lift pad rubs the surface until sufficient force is generated to lift the pad into a noncontact position. Leakage will occur between the noncontact overlapping fingers and the lift-pad extended fingers. These seals respond to both radial and axial shaft perturbations and some degree of misalignment with minimal hysteresis; the latter is a problem in conventional finger seals and some types of early brush seal designs. The importance of including coupled thermal/fluid/structural interactions makes the difference between a seal that works and one that does not. With this in mind, Braun et al. (2003) were able to determine flow patterns and provide seal dynamic response for the padded-finger seal by relating the cantilever or finger stiffness to fluid stiffness.

***Fluid film journal bearing***.—Temis and Temis (2003) also cite the importance of fluid/structural interactions in predicting load capacity and stability for conventional fluid film journal bearings. In their analysis the energy equation and conjugate heat transfer are neglected as are compressibility effects, which need further consideration. Nevertheless, consider a bronze steel-shaft journal bearing. Young's moduli are $E_{bronze} = 0.75\times10^5$ MPa and $E_{steel} = 1.15\times10^5$ MPa with a Poisson ratio of 0.3 for both. Shaft diameter is 30 mm, clearance ($c = \delta$) is 0.05 mm, and the ratio of turbine diameter to blade length $D/L = 1$. The shaft rotates at 30 000 rpm, with oil viscosity of $0.02\times10^{-6}$ Pa-s at an eccentricity ratio $\varepsilon = \chi = e/c = 0.8$.

Figure 57 illustrates the loading, figure 58 the deformed fluid film journal bearing surfaces, and figure 59 the actual displacements. Note that these displacements have to be reflected to circumferential angle $\varphi = 0$. With a compliant interface the load exerted by the fluid film on the bearing support tends to a finite value rather than an infinite value as eccentricity $\varepsilon = \chi \rightarrow 1$ (fig. 60(a)) and the attitude angle $\theta$ tends to be nonzero (fig. 60(b)). These compliant surfaces greatly affect stability margins, tending to lower stability with increasing bearing $D/L$ (fig. 61). The singularity ($\varepsilon = \chi \rightarrow 1$) was not examined because it represents boundary-lubricated or dry-contact rub with significant heat release, another feature to be added to bearing analysis research and development. (See also the section Life and Reliability Issues in part 3.)

***Rotor impact loading***.—In Navy aircraft slammed onto the deck by the arresting hook cable and other hard landings, the aircraft gas turbine's rotor bearing undergoes abrupt changes in loading, termed "impact loading," a common occurrence. Aircraft tires are seldom spun to speed prior to the impact loadings of landing and associated spin-up to speed. Runway tire marks and maintenance records attest to the brutal nature of hard impacts absorbed by landing gear struts and tire spin-up.

The analysis is beyond our scope, but the similarities are not as we consider yet another class of fluid/structural interactions. Muszynska (2003) shows the effects of horizontal rotor drop onto retainer or load-sharing bearings due to the loss of magnetic bearing support to be skid and bounce. Skid represents a form of dry or boundary-lubricated contact for very short periods of time. The time rate of change of the angular coordinate position is modified by subtracting the term $K\Omega$ (tangential radial stiffness coefficient times rotational speed). The $K$ term is related to surface shear force or $\mu N$ (kinetic friction times rotor radial load and surface speed differential). The energy release, surface deformation, and lubrication problems have yet to be considered, as is also the case of $N = Mg$ (rotor mass times gravitational acceleration) rotor loading where other perturbations can significantly alter these results (e.g., a vertical rotor). Depending on the value of $K$ the skid or bouncing stage leads the rotor either to stabilization or to a very dangerous mode of self-excited vibrations called dry whip. Muszynska (2003) gives requirements for retainer (backup) and load-sharing bearings. They must

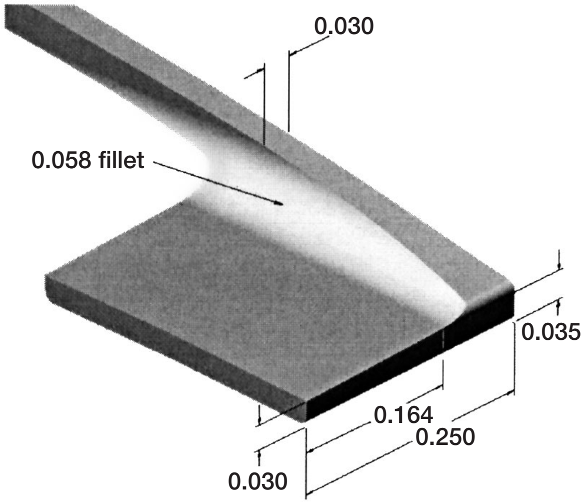


Figure 55.—Typical dimensions (in inches) and appearance of padded finger. (Braun et al., 2003.)

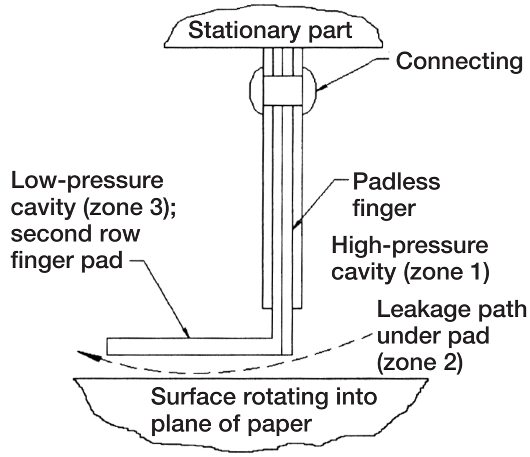


Figure 56.—Boundary conditions for finger seal. Schematic cross section with two rows of padded low-pressure and padless high-pressure fingers and definition of pressure zones. (Braun et al., 2003.)

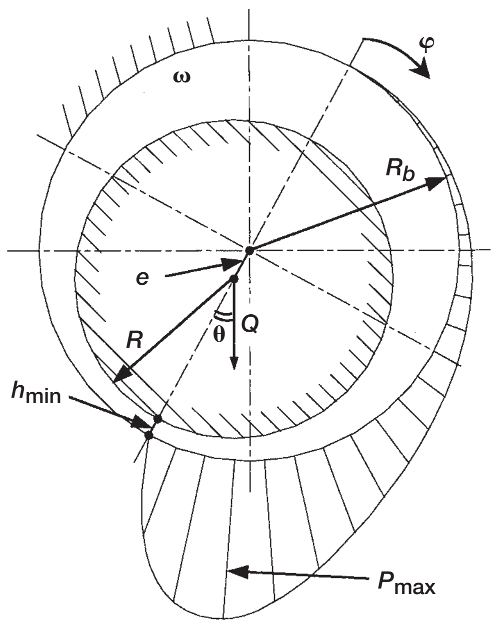


Figure 57.—Section of fluid film journal bearing. (Temis and Temis, 2003.) Courtesy ISCORMA–2.

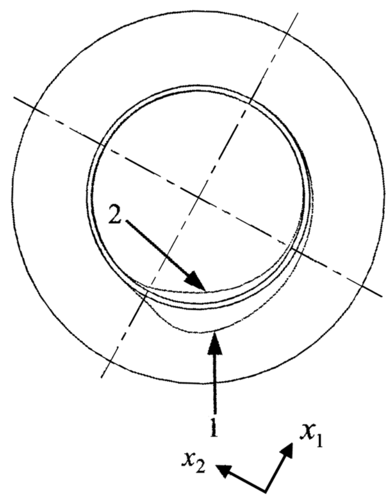


Figure 58.—Fluid film bearing with deformed surfaces (1–bearing surface; 2–shaft journal surface). (Temis and Temis, 2003.) Courtesy ISCORMA–2.

provide machine support at rest and at all transient states between rests and provide stable operation as well as support in the event of magnetic bearing failure. In addition, these bearings must ensure safe, efficient, cost-effective machine operation.

Although first-stage disk failure of the high-pressure turbine is *the critical component* in turbomachine failure, turbine and compressor blade fatigue failures also represent serious design challenges. Rzadkowski et al. (2003) investigated the natural frequencies of shrouded blade/disk/shaft models of one, two, and three turbine stages. The turbine disk modeled had a 0.685-m outside diameter with a 0.196-m bore and 144 tuned blades 0.159 m long (fig. 62). Details and specification of the model, geometry, element interface connections, and normalization parameters were not

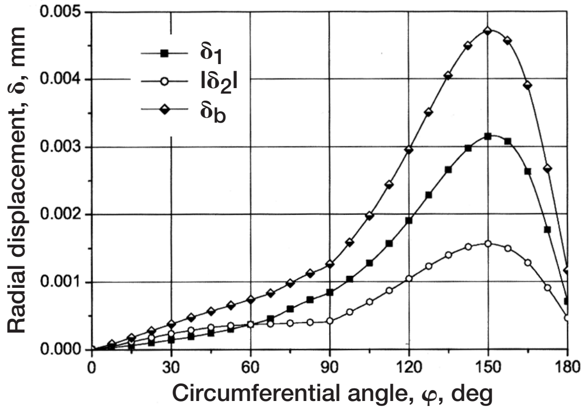


Figure 59.—Bearing and shaft journal radial displacements as function of circumferential angle; $\delta_1$ = bearing displacement, $|\delta_2|$ = magnitude of shaft displacement, $\delta_b$ = total displacement gap. (Temis and Temis, 2003.) Courtesy ISCORMA–2.

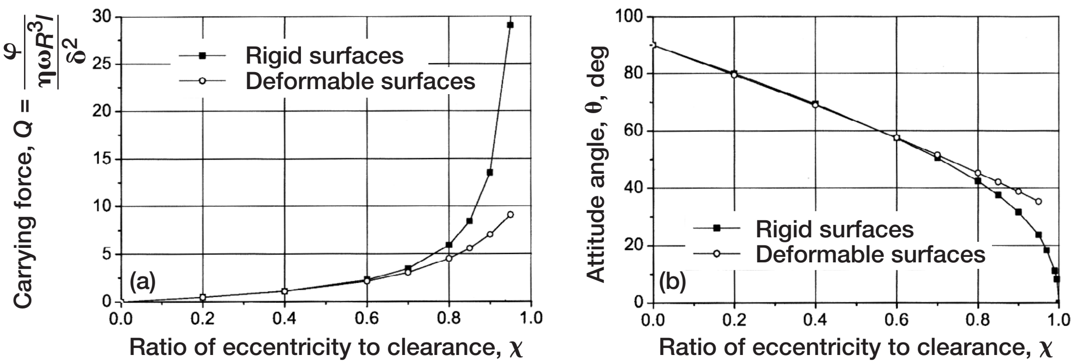


Figure 60.—Bearing resultant carrying force (a) and attitude angle (b) as function of ratio of eccentricity to clearance. (Temis and Temis, 2003.) Courtesy ISCORMA–2.

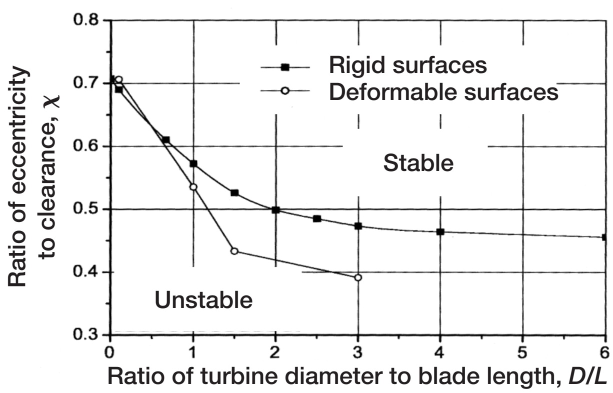


Figure 61.—Boundary between stable and unstable orbits for shaft journal motion in bearing. (Temis and Temis, 2003.) Courtesy ISCORMA–2.

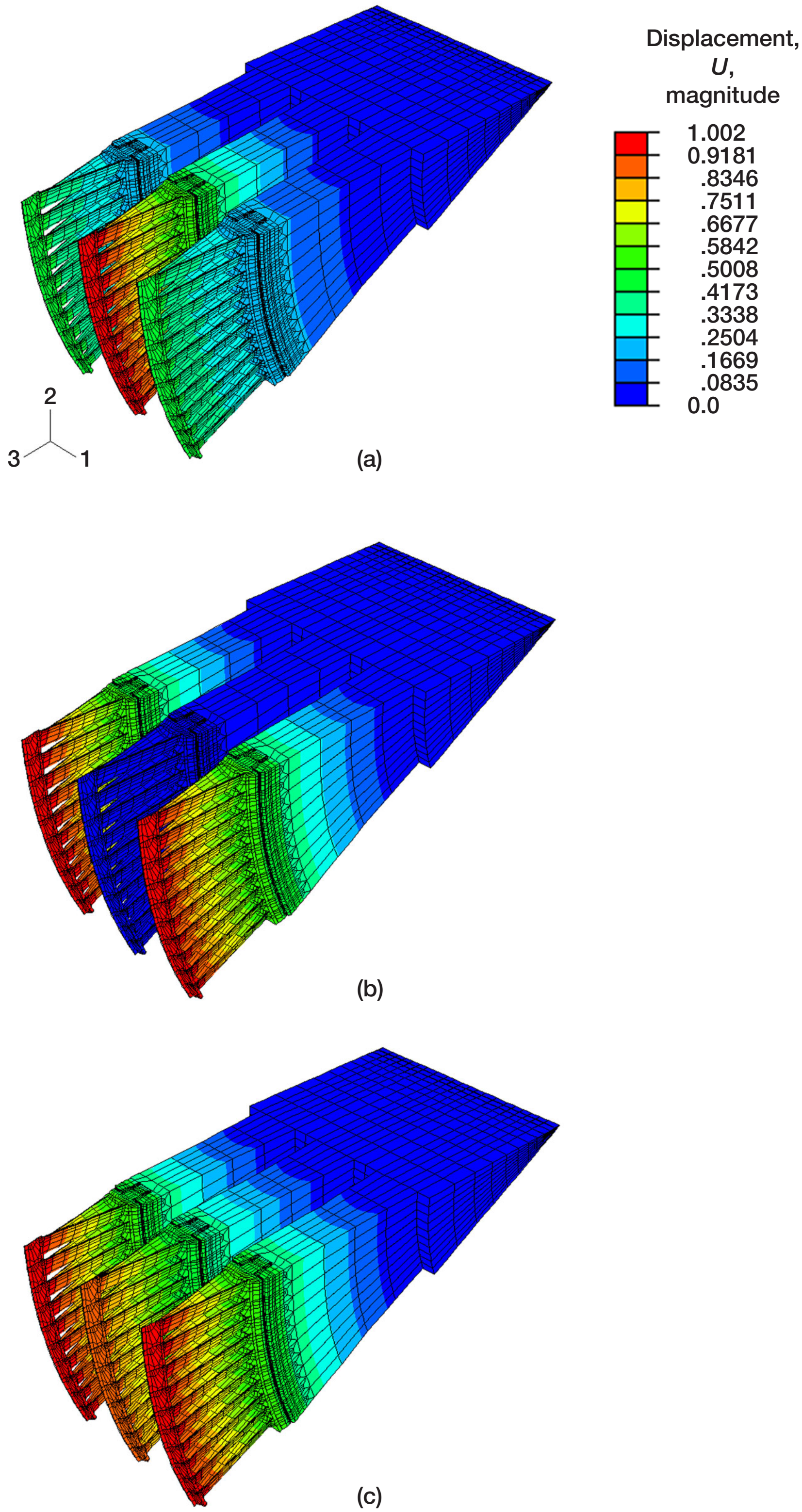


Figure 62.—Dimensionless relative displacements of three shrouded blade disks placed on shaft illustrating modal shapes. (a) Inner disk motion. (b) Outer disk motion. (c) Nearly equivalent motion. (Rzadkowski et al., 2003.)

disclosed, making it impossible to replicate or apply the authors' results directly without their consent. Note that detuning the blades enhances stability. The modes of the bladed disks are classified by using an analogy with axisymmetric modes, which are mainly characterized by nodal lines lying along the diameters of the structure and having constant angular spacing (see also fig. 7). There are either zero ($k = 0$), one ($k = 1$), two ($k = 2$), or more ($k > 2$) nodal diameters in bending or torsion modes to 73 nodal diameters because there are 146 blades on the disk. For a single cantilevered blade, series 1 is associated with the first natural frequency, series 2 with the second natural frequency, etc., where $k$ is the number of nodal diameters. Rzadkowski et al. (2003) determined the influence of shaft flexibility on the natural frequencies of the shrouded bladed disks to four nodal diameters for two first-frequency series. Here, to four nodal diameters the number 4 is dependent on the geometrical parameters of the blade, disk, and shaft. Sometimes it is only one nodal diameter. For unshrouded cantilevered blades the natural frequencies (given in table IV) are the limit of the series of natural frequencies of unshrouded bladed disks. The actual frequencies are then found by multiplying by a constant for the configuration (not provided; contact the authors). The relative nondimensional amplitude values and the order of disk vibration are taken from figures of the mode shapes (not provided; contact the authors).

# References

Abbott, D.R. (1981) Advances in Labyrinth Seal Aeroelastic Instability Prediction and Prevention, J. Engineering for Power, vol. 103, pp. 308, 312.

Alford, J.S. (1963) Protection of Labyrinth Seals From Flexural Vibration, ASME Paper 63–AHGT–9. (Also J. Engineering for Power, Apr. 1964, pp. 141–148.)

Alford, J.S. (1965) Protecting Turbomachinery From Self-Excited Rotor Whirl, J. Engineering for Power, series A, vol. 87, Oct., pp. 333–344.

Alford, J.S. (1967) Protecting Turbomachinery From Unstable and Oscillatory Flows, J. Engineering for Power, Series A, vol. 89, Oct., pp. 513, 528.

Alford, J.S. (1971) Labyrinth Seal Designs Have Benefited From Development and Service Experience, SAE Paper 710435.

Anon. (1965) Aerodynamic Design of Axial-Flow Compressors (Revised), I.A. Johnsen and R.O. Bullock, eds., NASA SP–36. (Supersedes declassified NACA Memorandums E56B03, E56B03a, and E56B03b, 1956.)

Athavale M.M., Przekwas, A.J., Hendricks, R.C., and Liang, A. (1992) SCISEAL—A Three-Dimensional CFD Code for Accurate Analyses of Fluid Flows and Forces in Seals, Proceedings of Conference on Advanced Earth-to-Orbit Propulsion Technology.

Athavale, M.M., Przekwas, A.J., and Hendricks, R.C. (1993) Driven Cavity Simulation of Turbomachine Blade Flows With Vortex Control, AIAA Paper 93–0390.

Benckert, H. and Wachter, J. (1978) Studies on Vibrations Stimulated by Lateral Forces in Sealing Gaps, AGARD Power, Energetics, and Propulsion Meeting on Seal Technology in Gas Turbine Engines, AGARD–CP–237 (AGARD–AR–123), Paper 9.

Benckert, H. and Wachter, J. (1980) Rotordynamic Instability Problems in High-Performance Turbomachinery, NASA CP–2133, pp. 189–212.

Bently, D.E., Muszynska, A., and Hendricks, R.C., eds. (1986) Instability in Rotating Machinery, NASA CP–2409.

Bently, D.E. (2001) Private Communication at the 1st International Symposium on Stability Control of Rotating Machinery (ISCORMA–1), South Lake Tahoe, California, Aug. 20–24.

Bently, D.E., Hatch, C.T., and Grissom, B., eds. (2002) Fundamentals of Rotating Machinery Diagnostics, Bently Pressurized Bearings Press, Minden, Nevada.

Black, H.F. (1968) Effects of Hydraulic Forces in Annular Pressure Seals on the Vibrations of Centrifugal Pump Rotors, J. Mechanical Engineering Science, vol. 11, no. 2, pp. 206–213.

Black, H.F. and Jenssen, D.N. (1969–70) Dynamic Hybrid Bearing Characteristics of Annular Controller Leakage Seals, Proceedings of Institution of Mechanical Engineers, vol. 184, pt. 3N, pp. 92–100.

Bradshaw, P. (1969) The Analogy Between Streamline Curvature and Buoyancy in Turbulent Shear Flow, J. Fluid Mechanics, vol. 36, pp. 177–197.

Bradshaw, P. (1973) Effects of Streamline Curvature on Turbulent Flow, AGARD Monograph 169.

Braun, M.J., Batur, C., Ida, N., Rose, B., Hendricks, R.C., and Mullen, R.L. (1987) A Nonintrusive Laser Based Analysis for Thin Film Flow at Low Reynolds Numbers, Int. Conf. on Tribology, Lubrication, and Wear, Inst. of Mech. Engr., London, July 1–3, Paper 342/143.

Braun, M., Pierson, H., Deng, D., Choy, F., Proctor, M., and Steinetz, B. (2003) Structural and Dynamic Considerations Towards the Design of a Padded Finger Seal, AIAA Paper 2003–4698.

Camatti, M., Vannini, G., Baldassarre, L., Fulton, J., and Forte, P. (2003a) Full Load Test Experience on the Instability of a High Speed Back to Back Compressor Equipped With a Honeycomb Seal (Paper 110), Proceedings of the 2nd International Symposium on Stability Control of Rotating Machinery (ISCORMA–2), A. Gosiewski and A. Muszynska, eds., pp. 617–626.

Camatti, M., Vannini, G., Fulton, J., and Hopenwasser, F. (2003b) Instability of a High Pressure Compressor Equipped With Honeycomb Seals, Proceedings of the 32nd Turbomachinery Symposium.

Childs, D.W. (1983) The SSME HPFTP Interstage Seals: Analysis and Experiments for Leakage and Reaction Force Coefficients, NASA CR–170876.

Childs, D.W. (1984) SSME HPFTP Interstage Seals: Analysis and Experiments for Leakage and Force Coefficients, NASA Contract NAS8–33716, Turbomachine Laboratories, Texas A&M University, College Station, Texas, Feb.

Childs, D.W., Vance, J.M., and Hendricks, R.C., eds. (1984) Rotordynamic Instability Problems in High-Performance Turbomachinery—1984, NASA CP–2338.

Childs, D.W., Baskharone, E., and Ramsey, C. (1991) Test Results for Rotordynamic Coefficients of the SSME HPOTP Turbine Interstage Seal With Two Swirl Brakes, NASA CP–3122, pp. 165–178.

Childs, D.W. (1993) Turbomachinery Rotordynamics Phenomena, Modeling, and Analysis, John Wiley & Sons, New York.

Colding-Jorgensen, J. (1980) Effect of Fluid Forces on Rotor Stability of Centrifugal Compressors and Pumps, NASA CP–2133, pp. 249–265.

Crandall, S.H. (1980) Physical Explanations of the Destabilizing Effect of Damping in Rotating Parts, NASA CP–2133.

Davis, E.Y. and Stearns, E.M. (1985) Energy Efficient Engine, Flight Propulsion System, Final Design, and Analysis, NASA CR–168219.

Dimofte, F. and Hendricks, R.C. (2001) Wave Journal Bearings Under Dynamic Loads, NASA/TM—2002-211079.

Ehrich, F.F. (1993) Rotor Whirl Forces Induced by the Tip Clearance Effect in Axial Flow Compressors, J. Vibration and Acoustics, vol. 115, pp. 509–515.

Fleming, D.P. (1977) High Stiffness Seals for Rotor Critical Speed Control, ASME Paper 77–DET–10. (Also NASA TMX–73654.)

Fulton, J. (2003) Rotor Stability Criteria for Multistage Centrifugal Compressors, Proceedings of the ASME 2003 Design Engineering Technical Conference and Computers and Information in Engineering Conference (DETC'03), DETC2003/VIB–48459.

Halila, E.E., Lenahan, D.T., and Thomas, T.T. (1982) Energy Efficient Engine High Pressure Turbine Test Hardware: Detailed Design Report, NASA CR–167955.

Hendricks, R.C. (1981a) Investigation of a Straight Cylindrical Seal for High-Performance Turbomachines, NASA TP–1850.

Hendricks, R.C. (1981b) Investigation of a Three-Step Cylindrical Seal for High-Performance Turbomachines, NASA TP–1849.

Hendricks, R.C. (1981c) Investigation of a Three-Step Labyrinth Seal for High-Performance Turbomachines, NASA TP–1848.

Hendricks, R.C., Griffin, T.A., Kline, T.R., Csavina, K.R., Pancheli, A., and Sood, D. (1994) Relative Performance Comparison Between Baseline Labyrinth and Dual Brush Compressor Discharge Seals in a T–700 Engine Test, Proceedings of the International Gas Turbine and Aeroengine Congress and Exposition, Paper 94–GT–266.

Hendricks, R.C., Steinetz, B.M., Athavale, M.M., Przekwas, A.J., Braun, M.J., Dozozo, M.I., Choy, F.K., Kudriavtsev, V.V., Mullen, R.L., and von Pragenau, G.L. (1995) Interactive Developments of Seals, Bearings, and Secondary Flow Systems With the Power Stream, Int. J. Rotating Machinery, vol. 1, no. 3–4, pp. 153–185.

Hoffman, P.H., Muck, K.C., and Bradshaw, P. (1985) The Effect of Concave Surface Curvature on Turbulent Boundary Layers, J. Fluid Mechanics, vol. 161, pp. 371–403.

Iwatsubo, T. and Iwasaki, Y. (2002) Experimental and Theoretical Study on Swirl-Braked Labyrinth Seal, Proceedings of the 6th International Conference on Rotor Dynamics (IFToMM), pp. 564–572.

Johnsen, I.A. and Bullock, R.O., eds. (1965) Aerodynamic Design of Axial-Flow Compressors (Revised), NASA SP–36. (Supersedes declassified NACA Memorandums E56B03, E56B03a, and E56B03b, 1956.)

Kanki, H., Shibabe, S., and Goshima, N. (2003) Destabilizing Force of Labyrith Seal Under Partial Admission Condition (Paper 201), Proceedings of the 2nd International Symposium on Stability Control of Rotating Machinery (ISCORMA–2), A. Gosiewski and A. Muszynska, eds., pp. 278–288.

Kawak, H.-D., Lee, Y.-B., Kim, C.-H., Ha, T.-W., and Woo, Y.-C. (2002) Prediction of Rotordynamic Stability for a High Pressure High Speed Turbopump Unit. Proceedings of 6th International Conference on Rotor Dynamics (IFToMM), pp. 478–486.

Kim, H. and Rhode, D.L. (1999) Swirling Streamline-Curvature Law of the Wall From a Novel Perturbation Analysis, Numerical Heat Transfer, part B, vol. 36, pp. 311–330.

Kostyuk, A. (1972) A Theoretical Analysis of the Aerodynamic Forces in the Labyrinth Glands of Turbomachine, Teploenergetika, vol. 19, no. 11, pp. 29–33.

Launder, B.E., Priddin, C.H., and Sharma, B.I. (1977) The Calculation of Turbulent Boundary Layers on Spinning and Curved Surfaces, J. Fluid Eng., vol. 231.

Leie, B. and Thomas, H.J. (1980) Self-Excited Rotor Whirl due to Tip-Seal Leakage Forces, NASA CP–2133, pp. 303–316.

Lewis, D.A., Platt, C.E., and Smith, E.B. (1978) Aeroelastic Instability in F100 Labyrinth Air Seals, Analytically Predicted, Experimentally Confirmed, Corrected by Tailoring Seal Clearance, AIAA Paper 78–1087.

Ludwig, L.P. (1978) Gas Path Sealing in Turbine Engines, AGARD–CP–237 (AGARD–AR–123). (Also NASA TM–73890 revised.)

Mailach, R., Lehmann, I., and Vogeler, K. (2001) Rotating Instabilities in an Axial Compressor Originating From the Fluctuating Blade Tip Vortex, J. Turbomachinery, vol. 123, July, pp. 453–463.

Motoi, H., Kitamura, A., Sakazume, N., Uchiumi, M., Uchida, M., Saiki, K., Nozaki, O., and Iwatsubo, T. (2003) Sub-Synchronous Whirl in the Le–7a Rocket Engine Fuel Turbo-Pump (Paper 105), Proceedings of the 2nd International Symposium on Stability Control of Rotating Machinery (ISCORMA–2), A. Gosiewski and A. Muszynska, eds., pp. 160–169.

Muck, K.C., Hoffman, P.H., and Bradshaw, P. (1985) The Effect of Concave Surface Curvature on Turbulent Boundary Layers, J. Fluid Mechanics, vol. 161, pp. 347–369.

Mullen, R.L. and Hendricks, R.C. (1983) Finite Element Formulation for Transient Heat Treat Problems, ASME–JSME Thermal Engineering Joint Conference, Vol. 3, Y. Mori and W.J. Yung, eds., ASME, New York, 1983, pp. 367–374. (Also NASA TM–83070.)

Munson, J., Grant, D., and Agrawal, G. (2002) Foil Face Seal Proof-of-Concept Demonstration Testing, AIAA Paper 2002–3791.

Muszynska, A. (1985) Whirl and Whip—Rotor/Bearing Stability Problems, Instability in Rotating Machinery, NASA CP–2409, pp. 155–177.

Muszynska, A. (1986a), Whirl and Whip Rotor/Bearing Stability Problems, J. Sound and Vibration, vol. 110, no. 3, Nov. 8, pp. 443–462.

Muszynska, A. (1986b) Fluid-Related Rotor/Bearing/Seal Instability Problems, Bently Rotordynamics Research and Development Corp., BRDRC Report No. 2.

Muszynska, A., (1988a) Improvements in Lightly Loaded Rotor/Bearing and Rotor/Seal Models, J. Vibration, Acoustics, Stress, and Reliability in Design, vol. 110, no. 2, Apr., pp. 129–136.

Muszynska, A., Franklin, W.D., and Bently, D.E. (1988b) Rotor Active "Anti-Swirl" Control, J. Vibration, Acoustics, Stress, and Reliability in Design, vol. 110, no. 2, Apr., pp. 143–150.

Muszynska, A. and Bently, D.E., (1989) Anti-Swirl Arrangements Prevent Rotor/Seal Instability, J. Vibration, Acoustics, Stress, and Reliability in Design, vol. 111, no. 2, pp. 156–162.

Muszynska, A. and Bently, D.E. (1990), Frequency Swept Rotating Input Perturbation Techniques and Identification of the Fluid Force Models in Rotor/Bearing/Seal Systems and Fluid Handling Machines, J. Sound and Vibration, vol. 143, no. 1, 1990, pp. 103–124.

Muszynska, A., (1995) Modal Testing of Rotors With Fluid Interaction, Int. J. Rotating Machinery, vol. 1, no. 2, pp. 83–116.

Muszynska, A. (2001) The Fluid Force Model in Rotating Machine Clearances Identified by Modal Testing and Model Applications: An Adequate Interpretation of the Fluid-Induced Instabilities, Invited Lecture, Proceedings of the 1st International Symposium on Stability Control of Rotating Machinery (ISCORMA–1).

Muszynska, A. (2003) Impacting of a Rotor Against Retainer Bearing (Paper 604), Proceedings of the 2nd International Symposium on Stability Control of Rotating Machinery (ISCORMA–2), A. Gosiewski and A. Muszynska, eds., pp. 417–427.

NASA Conference Publications, Childs, D.W., Vance, J.M., and Hendricks, R.C., eds., Rotordynamic Instability Problems in High-Performance Turbomachinery. [1] NASA CP–2133, 1986. NASA CP–2133 (1980); NASA CP–2250 (1982); NASA CP–2338 (1984); NASA CP–2409 (1985); NASA CP–2443 (1986); NASA CP–3026 (1988); NASA CP–3122 (1990); NASA CP–3239 (1993); NASA CP–3344 (1997); and Instability in Rotating Machinery, NASA CP–2409 (1985).

NASA Conference Publications, Hendricks, R.C., Liang, A.D., and Steinetz, B.M., eds., Seals Code Development and Seal and Secondary Air Systems Workshops Conference Publications NASA CP–10124 (1992); NASA CP–10136 (1993); NASA CP–10181 (1995); NASA CP–10198 (1996); NASA CP–208916 (1998); NASA CP–210472 (2000); NASA CP–211208 (2001).

Queitzsch, G.K., Jr. and Fleming, D.P. (2001) Rotordynamic Influences on Rolling Element Bearing Selection and Operation, Proceedings of the 1st International Symposium on Stability Control of Rotating Machinery (ISCORMA–1).

Rodi, W. (1979) Influence of Buoyancy and Rotation on Equations for the Turbulent Length Scale, Proceedings of the 2nd Symposium on Turbulent Shear Flows.

Rzadkowski, R., Kwapisz, L., Sokolowski, J., Karpiuk, R., Ostrowski, P., and Radulski, W. (2003) Natural Frequencies and Mode Shapes of Rotating Three Shrouded Bladed Discs Placed on the Part of the Shaft (Paper 603), Proceedings of the 2nd International Symposium on Stability Control of Rotating Machinery (ISCORMA–2), A. Gosiewski and A. Muszynska, eds., pp. 381–392.

San Andres, L. and Childs, D. (1997) Angled Injection-Turbulent Flow Hybrid Bearings, Comparison to Test Results, NASA CP–3344, pp. 20–46.

Schuck G. and Nordmann, R. (2002) Investigation of Self-Excited Vibrations in Flexible Labyrinth Seals due to Instationary Pressure-Fields, Proceedings of the Sixth International Conference on Rotor Dynamics (IFToMM), Vol. II, pp. 995–1002 (Paper 209FP_Schuck.pdf).

Schuck, G. and Nordmann, R. (2003) Influence of Structural Parameters and Flow Conditions on the Dynamic Behavior of Flexible Labyrinth Seals (Paper 312), Proceedings of the 2nd International Symposium on Stability Control of Rotating Machinery (ISCORMA–2), A. Gosiewski and A. Muszynska, eds., pp. 289–299.

Shapiro, W. (1996) Industrial Computer Codes, NASA CP–10181, pp. 115–143.

Smith, D.M. (1933) The Motion of a Rotor Carried by a Flexible Shaft in Flexible Bearings, Proc. Royal Society (London), Series A, vol. 142, pp. 92–118.

Smits, A.J., Young, S.T.B., and Bradshaw, P. (1979) The Effect of Short Regions of High Surface Curvature on Turbulent Boundary Layers, J. Fluid Mechanics, vol. 94, part 2, pp. 209–242.

Spalding, D.B. (1981) A General Purpose Computer Program for Multi Dimensional One- and Two Phase Flow, Mathematics and Computers in Simulation, vol. 23, no. 3, Sept., pp. 267–276.

Stewart, P.A.E. and Brasnett, K.A. (1978) The Contribution of Dynamic X-Ray to Gas Turbine Air Sealing Technology, AGARD–CP–237 (AGARD–AR–123), Paper 10.

Storace, A.F., Wisler, D.C., Shin, H.-W., Beacher, B.F., Ehrich, F.F., Spakovszky, Z.S., Martinez-Sanchez, M., and Song, S.J. (2001) Unsteady Flow and Whirl-Inducing Forces in Axial-Flow Compressors: Part I—Experiment, J. Turbomachinery, vol. 123, July, pp. 433–445. {Note the scales of figure 11 are incorrect, and authors use nonconventional static pressure rather than conventional $(P_t - p_s)/(V^2/2)$ in their diagrams.}

Surial, A. and Kaushal, A. (2003) Coupled Vibration Analysis of an Industrial Gas Turbine Engine and Drivetrain—Analysis and Testing (Paper 412), Proceedings of the 2nd International Symposium on Stability Control of Rotating Machinery (ISCORMA–2), A. Gosiewski and A. Muszynska, eds., pp. 322–330.

Tam, L.T. (1985) An Interim Report on the Calculation Method for a Multi Dimensional Whirling Seal, CHAM of North America, Huntsville, Alabama.

Tam, L.T., Przekwas, A.J., and Hendricks, R.C. (1986) Numerical Modeling of Multi-Dimensional Whirling Seal and Bearings, CHAM of North America, Huntsville, Alabama. (Presented at NASA Lewis Research Center, Dec. 1986.)

Tam, L.T., Przekwas, A.J., Muszynska, A., Hendricks, R.C., Braun, M.J., and Mullen, R.L. (1988) Numerical and Analytical Study of Fluid Dynamic Forces in Seals and Bearings, J. Vibration, Acoustics, Stress, and Reliability in Design, vol. 110, July, pp. 315–325. (Also NASA TM–100268.)

Temis, Y.M and Temis, M.Y. (2003) Influence of Elastohydrodynamic Contact Deformations in Fluid Film Bearing on High-Speed Rotor Dynamics (Paper 301), Proceedings of the 2nd International Symposium on Stability Control of Rotating Machinery (ISCORMA–2), A. Gosiewski and A. Muszynska, eds. pp. 150–159.

Thomas, R.J. (1958) Unstable Oscillations of Turbine Rotors due to Steam Leakage in the Clearances of the Sealing Glands and the Buckets, Bulletin Scientifique, A.J.M., vol. 71, pp. 1039–1063. (See also NASA CP–2133, 1980.)

Thompson, W.E. (1980) Vibration Exciting Mechanisms Induced by Flow in Turbomachine Stages, NASA CP–2133, pp. 285–302.

Tseng, T., McNickel, A., Steinetz, B., and Turnquest, N. (2002) Aspirating Seal GE90 Test, 2001 NASA Seal/Secondary Air System Workshop, NASA/CP—2002-211911/VOL1, pp. 79–93.

Vance, J. (1988) Rotordynamics of Turbomachinery, John Wiley & Sons, Inc., New York.

von Pragenau, G.L. (1982) Damping Seals for Turbomachinery, NASA TP–1987.

von Pragenau, G.L. (1985) Damping Seals for Turbomachinery, NASA CP–2372, pp. 438–451.

von Pragenau, G.L. (1992) From Labyrinth Seals to Damping Seals/Bearings, Proceedings of the 4th International Symposium on Transport Phenomena and Dynamics of Rotating Machinery (ISROMAC–4), pp. 277, 285.

Wohlrab, R. (1983) Experimental Determination of Gap Flow-Conditioned Forces at Turbine Stages and Their Effect on the Running Stability of Simple Rotors, NASA TM–77293. (Translation of Wohlrab, R. (1975) Experimentelle Ermittlung Spaltstromungabedingter Krafte an Turbinenstufen und deren Einflub auf die Laufstabilitat einfacher Rotoren, Dissertation, Technical University of Munchen.)

Yu, Z. and Childs, D. (1997) A Comparison of Experimental Rotordynamic Coefficients and Leakage Characteristics Between Hole-Pattern Gas Damper Seals and a Honeycomb Seal, NASA CP–3344, pp. 77–93.

# REPORT DOCUMENTATION PAGE

*Form Approved*
*OMB No. 0704-0188*



**1. AGENCY USE ONLY** (*Leave blank*)

**2. REPORT DATE**
July 2004

**3. REPORT TYPE AND DATES COVERED**
Technical Memorandum

**4. TITLE AND SUBTITLE**
Turbomachine Sealing and Secondary Flows
Part 2—Review of Rotordynamics Issues in Inherently Unsteady Flow Systems With Small Clearances

**5. FUNDING NUMBERS**
Cost Center 2250000013

**6. AUTHOR(S)**
R.C. Hendricks, L.T. Tam, and A. Muszynska

**7. PERFORMING ORGANIZATION NAME(S) AND ADDRESS(ES)**
National Aeronautics and Space Administration
John H. Glenn Research Center at Lewis Field
Cleveland, Ohio 44135–3191

**8. PERFORMING ORGANIZATION REPORT NUMBER**
E–13662–2

**9. SPONSORING/MONITORING AGENCY NAME(S) AND ADDRESS(ES)**
National Aeronautics and Space Administration
Washington, DC 20546–0001

**10. SPONSORING/MONITORING AGENCY REPORT NUMBER**
NASA TM—2004-211991-PART2

**11. SUPPLEMENTARY NOTES**
Portions of this material were presented at Second International Symposium on Stability Control of Rotating Machinery sponsored by Bently Pressurized Bearing Company, Gdansk, Poland, August 4–8, 2003. R.C. Hendricks, NASA Glenn Research Center; L.T. Tam, Lockheed Martin Space Systems Company, Sunnyvale, California 94089; and A. Muszynska, A.M. Consulting, Minden, Nevada 89423. Responsible person, R.C. Hendricks, organization code 5000, 216–977–7507.

**12a. DISTRIBUTION/AVAILABILITY STATEMENT**
Unclassified - Unlimited
Subject Categories: 01, 07, 20, and 37 Distribution: Nonstandard
Available electronically at http://gltrs.grc.nasa.gov
This publication is available from the NASA Center for AeroSpace Information, 301–621–0390.

**12b. DISTRIBUTION CODE**

**13. ABSTRACT** ***(Maximum 200 words)***
Today's computational methods enable the determination of forces in complex systems, but without field validation data, or feedback, there is a high risk of failure when the design envelope is challenged. The data of Childs and Bently and field data reported in NASA Conference Proceedings serve as sources of design information for the development of these computational codes. Over time all turbomachines degrade and instabilities often develop, requiring responsible, accurate, turbomachine diagnostics with proper decisions to prevent failures. Tam et al. (numerical) and Bently and Muszynska (analytical) models corroborate and implicate that destabilizing factors are related through increases in the fluid-force average circumferential velocity. The stability threshold can be controlled by external swirl and swirl brakes and increases in radial fluid film stiffness (e.g., hydrostatic and ambient pressures) to enhance rotor stability. Also cited are drum rotor self-excited oscillations, where the classic "fix" is to add a split or severed damper ring or cylindrical damper drum, and the Benkert-Wachter work that engendered swirl brake concepts. For a smooth-operating, reliable, long-lived machine, designers must pay very close attention to sealing dynamics and diagnostic methods. Correcting the seals enabled the space shuttle main engine high-pressure fuel turbopump (SSME HPFTP) to operate successfully.

**14. SUBJECT TERMS**
Turbomachine; Seals; Dynamics; Antiswirl; CFD; Models; Fluid dynamic forces; Rotor and stator clearances

**15. NUMBER OF PAGES**
78

**16. PRICE CODE**

| 17. SECURITY CLASSIFICATION OF REPORT | 18. SECURITY CLASSIFICATION OF THIS PAGE | 19. SECURITY CLASSIFICATION OF ABSTRACT | 20. LIMITATION OF ABSTRACT |
|---|---|---|---|
| Unclassified | Unclassified | Unclassified | |